Towards hybrid modeling of hybrid VAWT

Pan, J.

DOI
10.4233/uuid:30929ef5-705d-4fc6-9251-8d159e6b1139

Publication date
2024

Document Version
Final published version

Citation (APA)
Pan, J. (2024). *Towards hybrid modeling of hybrid VAWT*. [Dissertation (TU Delft), Delft University of Technology]. https://doi.org/10.4233/uuid:30929ef5-705d-4fc6-9251-8d159e6b1139

Towards Hybrid Modeling Of Hybrid VAWT

Jingna Pan

Propositions

accompanying the dissertation

TOWARDS HYBRID MODELING OF HYBRID VAWT

by

Jingna PAN

1. The hybrid Eulerian-Lagrangian model is superior to the Eulerian model for rotor aerodynamics. (Thesis)
2. Savonius wind turbines are not outdated. (Thesis)
3. Lagrangian models are the most effective models in simulations of VAWT. (Thesis)
4. The added complexity of combining Darrieus and Savonius in the hybrid VAWT is ideal in the urban area compared to individual wind turbines.
5. Peak power performance of hybrid VAWT does not matter for urban wind turbines.
6. To achieve excellence in research you must exist in a state of simultaneous stress and relaxation.
7. Zooming in to achievements and zooming out to setbacks simplify your life.
8. Artificial intelligence has no spontaneous emotions, which is a limitation inherent in its design and programming.
9. Privacy in the workplace is of significant importance as a fundamental factor in enhancing the performance of employees. Not providing a private workspace is harmful to education and research at TU Delft.
10. With open access, TU Delft should offer every student/employee free access to academic resources including grammar checkers and ChatGPT.

These propositions are regarded as opposable and defendable, and have been approved as such by the promotor prof. dr. ir. C. J. S. Ferreira and copromotor dr.ir. A. H. van Zuijlen.

Stellingen

behorende bij het proefschrift

TOWARDS HYBRID MODELING OF HYBRID VAWT

door

Jingna PAN

1. Het hybride Euleriaanse-Lagrangiaanse model is superieur aan het Euleriaanse model voor rotor-aerodynamica. (Proefschrift)
2. Savonius-windturbines zijn niet achterhaald. (Proefschrift)
3. Lagrangiaanse modellen zijn de meest effectieve modellen bij simulaties van VAWTs. (Proefschrift)
4. De toegevoegde complexiteit van het combineren van Darrieus en Savonius in de hybride VAWT is ideaal voor gebruik in stedelijk gebied vergeleken met gebruik als individuele windturbine.
5. De piekvermogensprestatie van hybride VAWTs doet er niet toe voor stedelijke windturbines.
6. Om uitmuntendheid in onderzoek te bereiken, moet je in een staat van gelijktijdige stress en ontspanning verkeren.
7. Inzoomen op prestaties en uitzoomen op tegenslagen vereenvoudigt je leven.
8. Kunstmatige intelligentie heeft geen spontane emoties, wat een beperking is die inherent is aan haar ontwerp en programmering.
9. Privacy op de werkplek is een fundamentele factor om de prestaties van werknemers te verbeteren. Het niet bieden van een privéwerkruimte is schadelijk voor het onderwijs en onderzoek aan de TU Delft.
10. Met open toegang zou de TU Delft elke student/werknemer gratis toegang moeten bieden tot academische bronnen, inclusief grammaticacheckers en ChatGPT.

Deze stellingen worden opponeerbaar en verdedigbaar geacht en zijn als zodanig goedgekeurd door de promotor prof. dr. ir. C. J. S. Ferreira en copromotor dr.ir. A. H. van Zuijlen.

TOWARDS HYBRID MODELING OF HYBRID VAWT

TOWARDS HYBRID MODELING OF HYBRID VAWT

Proefschrift

ter verkrijging van de graad van doctor
aan de Technische Universiteit Delft,
op gezag van de Rector Magnificus prof. dr. ir. T.H.J.J. van der Hagen,
voorzitter van het College voor Promoties,
in het openbaar te verdedigen op donderdag 5 september 2024 om 15:00 uur

by

Jingna PAN 潘静娜

Master of Science in Power Engineering,
China University of Petroleum (East China), Qingdao, China,
geboren te Shandong, China.

Dit proefschrift is goedgekeurd door de

Promotor: Prof. dr. ir. C.J.S. Ferreira
Copromotor: Dr. ir. A.H. van Zuijlen

Samenstelling promotiecommissie:

Rector Magnificus,	Voorzitter
Prof. dr. ir. C.J.S. Ferreira,	Technische Universiteit Delft, Nederland
Dr. ir. A.H. van Zuijlen,	Technische Universiteit Delft, Nederland

Onafhankelijke leden:

Prof. dr. D. Casalino	Technische Universiteit Delft, Nederland
Prof. dr. T. Griffth	University of Texas at Dallas, Verenigde Staten
Dr. R.J.A.M. Stevens	Universiteit Twente, Nederland
Prof. dr. M. Runacres	Vrije Universiteit Brussel, België
Prof. dr. P. Chatelain	Université catholique de Louvain, Frankrijk
Prof. dr. S.J. Watson	Technische Universiteit Delft, Nederland, reservelid

Keywords: Vertical axis wind turbine, numerical modeling, power performance, flow fields, hybrid Darrieus-Savonius turbine, hybrid Eulerian-Lagrangian model

Printed by: Ipskamp

Front & Back: Designed by Dr. D. Han

ISBN 978-94-6366-920-7
An electronic version of this dissertation is available at
http://repository.tudelft.nl/.

CONTENTS

SUMMARY

Vertical axis wind turbines (VAWTs) are popular design solutions for omnidirectional wind and limited installation area, particularly in urban areas, due to their advantages of low noise, low energy cost, and lower sensitivity to turbulence. They are often found in either of two distinct designs: the lift-driven Darrieus, with high aerodynamic power, and the drag-lift-driven Savonius, which excels in its start-up performance. The Darrieus-Savonius combined vertical axis wind turbine (hybrid VAWT) emerges from combining the advantages of Darrieus and Savonius. However, the hybrid VAWT has complex fluid dynamics, with multiple scales and interactions. Therefore, a comprehensive analysis and modeling of hybrid VAWTs can benefit from a multi-fidelity approach.

The choice of numerical methods, in either Eulerian or Lagrangian reference frames, holds paramount importance in simulating VAWTs, each method offering distinct advantages and limitations. Through high-fidelity Eulerian unsteady Reynolds averaged Navier Stokes (URANS) simulations, insights into airflow patterns, and turbulence phenomena across varied operating conditions are gained. Conversely, Lagrangian models such as the vortex particle method (VPM) can enable efficient analyses of vortical structures and wake interactions. While URANS simulation offers high-fidelity representations of complex flow phenomena and allows for precise optimization of turbine design parameters, it demands significant computational resources and expertise. In contrast, VPM excels in capturing flow features efficiently but may struggle to accurately represent boundary layer effects and near-wall flows. Consequently, the integration of both the Eulerian URANS and the Lagrangian VPM (hybrid method) is crucial for achieving comprehensive, reliable, and cost-effective simulations of VAWT performance. In this thesis, the hybrid VAWT is investigated using multi-fidelity numerical tools to estimate rotor/blade aerodynamics, computational efficiency and accuracy. Eulerian (U)RANS simulations in OpenFOAM and Lagrangian VPM are first applied to different types of VAWTs, followed by the application of the hybrid method in the hybrid VAWT case.

The goal of this thesis is also to investigate the flow features and power performance of the hybrid VAWT with multi-fidelity methods. In the context of the Eulerian reference frame, this thesis advances the knowledge of hybrid VAWT aerodynamics in several aspects. The Darrieus and Savonius parts in a hybrid VAWT are modeled as uniform force fields to exclude the effects of structural and operational parameters on the power losses of the wind turbines. The results show that the hybrid configuration cannot show a significant power increase, and it is only beneficial for the startup performance. The vortex dynamics behind the hybrid VAWT are analyzed in different attachment angles and tip speed ratios. The blade-vortex interaction is characterized and correlated with the torque generation of the Darrieus blade. Results show that the Darrieus blade torque increase is dependent on the interaction with the shed vortex from the advanced Savonius blade.

In the context of Lagrangian reference frame, both Savonius and hybrid VAWT con-

figurations are employed to assess the computational efficiency and accuracy of the vortex particle method. In the case of Savonius rotor simulations using the vortex method, the Savonius is defined as a rotor with two trailing edges because it has no clear leading/trailing edge like an airfoil, named double-trailing-edge-wake-modeling vortex particle method (DTVPM). Results show that a maximum power coefficient is achieved at a tip speed ratio of approximately 0.8, consistent with experimental findings. Furthermore, the process of trailing-edge vortex generation and detachment is effectively captured. A comparative analysis between Eulerian URANS simulations and Lagrangian DTVPM reveals that DTVPM offers a more efficient simulation of Savonius rotors without the need for empirical parameters. Notably, DTVPM demonstrates remarkable computational speed, with simulations being approximately 20 to 10^4 times faster than parallel URANS simulations over five revolutions. This significant reduction in computational time underscores the potential of DTVPM to enhance existing engineering models for wind energy applications. In the case of hybrid VAWT simulations, this thesis extends the application of VPM to hybrid VAWTs and introduces a viscous correction to improve simulation accuracy. By incorporating the airfoil polar, the proposed Lagrangian DTVPM effectively predicts comparable force variations to Eulerian URANS simulations. Importantly, the computational efficiency of URANS and DTVPM for hybrid VAWTs is compared, revealing that serial DTVPM simulations are approximately 20 times faster than parallel URANS simulations over ten revolutions. This notable increase in computational speed highlights the potential of DTVPM to provide efficient and accurate simulations for hybrid VAWTs, facilitating further advancements in wind energy technology.

In the context of the hybrid Eulerian-Lagrangian reference frame, this study aims to enhance accuracy and efficiency in analyzing complex flow phenomena. Through conducting various scenarios of hybrid VAWT using the hybrid method, this study concludes with the demonstration of the hybrid solver's capability in simulating hybrid VAWT aerodynamics. The final goal of this thesis is to ascertain an efficient model for hybrid VAWT and determine the limits of individual Eulerian and Lagrangian methods while considering specific flow features of VAWTs. Overall, this study contributes to comprehensive insights into the correlation of blade-vortex interaction and torque variation. The modeling challenge in the hybrid VAWT simulation is studied and a hybrid model is suggested to understand the performance and flow features of hybrid VAWTs.

SAMENVATTING

Verticale-as-windturbines (VAWTs) zijn populaire ontwerpoplossingen voor gebruik in gebieden met omnidirectionele wind condities en beperkte installatieruimte, voornamelijk in stedelijke gebieden, vanwege hun voordelen zoals lage geluidsniveaus, lage energiekosten en lagere gevoeligheid voor turbulentie. Er wordt meestal gebruik gemaakt van een van deze twee onderscheidende ontwerpen: de op draagkracht gebaseerde Darrieus, met een hoog aerodynamisch vermogen, en de op weerstand-draagkracht gebaseerde Savonius, die uitblinkt in zijn opstartprestaties. De gecombineerde Darrieus-Savonius verticale-as-windturbine (hybride VAWT) komt voort uit het combineren van de voordelen van Darrieus en Savonius. Deze hybride VAWT heeft echter complexe aerodynamica, die meerdere schalen en interacties behelst. Daarom kan een uitgebreide analyse en modellering van hybride VAWT's profijt hebben van een aanpak met meervoudige betrouewbaarheid.

De keuze van numerieke methoden, in zowel Euleriaanse als Lagrangiaanse referentiekaders, is van het grootste belang bij het simuleren van VAWT's, waarbij elke methode specifieke voordelen en beperkingen heeft. Door middel van betrouwbare, Euleriaanse, Reynolds-gemiddeld Navier-Stokes (URANS) simulaties worden inzichten verkregen in luchtstroompatronen en turbulentieverschijnselen bij verschillende bedrijfsomstandigheden. Daarentegen kunnen Lagrangiaanse modellen zoals de werveldeeltjesmethode (VPM) efficiënte analyses van wervelstructuren en zoginteracties mogelijk maken. URANS-simulaties bieden betrouwbare representaties van complexe stromingsverschijnselen en maken nauwkeurige optimalisatie van turbineontwerpparameters mogelijk, echter vereisen een aanzienlijke rekenkracht en expertise. In tegenstelling hiermee blinkt VPM uit in het efficiënt berekenen van stroomingsverschijnselen, echter VPM is minder geschikt om grenslaageffecten en stromingen nabij de wand nauwkeurig weer te geven. Hieruit volgt dat de integratie van zowel de Euleriaanse URANS als de Lagrangiaanse VPM (hybride methode) cruciaal is voor het verkrijgen van uitgebreide, betrouwbare en kosteneffectieve simulaties van VAWT-prestaties. In dit proefschrift wordt de hybride VAWT onderzocht met behulp van numerieke methodes met meervoudige betrouwbaarheid, om the onderzoeken hoe rotor-/bladaerodynamica, reken efficiëntie en nauwkeurigheid hiermee samenhangt. Eerst worden Euleriaanse (U)RANS-simulaties in OpenFOAM en Lagrangiaanse VPM simulaties toegepast op verschillende soorten VAWTs, gevolgd door de toepassing van de hybride methode in het geval van de hybride VAWT.

Het doel van dit proefschrift is ook om de stromingskenmerken en vermogensprestaties van de hybride VAWT te onderzoeken met behulp van deze methodes met meervoudige betrouwbaarheid. Gebruik makend van het Euleriaanse referentiekader vergroot dit proefschrift de kennis van de aerodynamica van hybride VAWT op verschillende gebieden. De Darrieus en Savonius onderdelen in een hybride VAWT worden gemodelleerd als uniforme krachtvelden om de effecten van structurele en operationele parameters

op de vermogensverliezen van de windturbines uit te sluiten. De resultaten tonen aan dat de hybride configuratie geen significante vermogensverhoging kan geven en alleen gunstig is voor de opstartprestaties. De werveldynamica achter de hybride VAWT wordt geanalyseerd bij verschillende aanhechtingshoeken en tipsnelheidsverhoudingen. De interactie tussen het blad en de wervel wordt gekarakteriseerd en gecorreleerd aan het gegenereerde koppel door het Darrieus-blad. Resultaten tonen aan dat de toename van het, door het Darrieus-blad, gegeneerde koppel afhankelijk is van de interactie met de afgeschudde wervels van het stroomopwaarts bewegende Savonius-blad.

Voor de Lagrangiaanse methode worden zowel Savonius- als hybride VAWT-configuraties gebruikt om de rekenkundige efficiëntie en nauwkeurigheid van de werveldeeltjesmethode te beoordelen. In het geval van Savonius-rotorsimulaties met de werveldeeltjesmethode wordt de Savonius gedefinieerd als een rotor met twee achterste randen omdat het geen eenduidige voor- en achterrand heeft zoals een vleugelprofiel dat wel heeft, genaamd dubbele-achterrand-zog-modellering werveldeeltjesmethode (DTVPM). Resultaten tonen aan dat een maximale vermogenscoëfficiënt wordt bereikt bij een tip-snelheidsverhouding van ongeveer 0,8, in overeenstemming met experimentele bevindingen. Bovendien wordt het proces van het genereren en afschudden van de wervel aan de achterrand effectief gemodelleerd. Een vergelijkende analyse tussen Euleriaanse URANS-simulaties en Lagrangiaanse DTVPM laat zien dat DTVPM een efficiëntere simulatie van Savonius-rotoren biedt zonder de noodzaak empirische parameters te bepalen. DTVPM toont met name een opmerkelijke rekenkundige snelheid, waarbij simulaties ongeveer 20 tot 10^4 keer sneller zijn dan parallelle URANS-simulaties voor een simulatieduur van vijf omwentelingen. Deze aanzienlijke vermindering van de rekentijd benadrukt het potentieel van DTVPM om bestaande benaderingsmodellen voor windenergietoepassingen te verbeteren. Voor hybride VAWT-simulaties breidt dit proefschrift de toepassing van VPM uit naar hybride VAWT's en introduceert een viskeuze correctie om de simulatienauwkeurigheid te verbeteren. Door de polaire van het vleugelprofiel toe te voegen, voorspelt de voorgestelde Lagrangiaanse DTVPM effectief vergelijkbare krachtvariaties als Euleriaanse URANS-simulaties. Belangrijk is dat de rekenkundige efficiëntie van URANS en DTVPM voor hybride VAWT's wordt vergeleken, waarbij blijkt dat seriële DTVPM-simulaties ongeveer 20 keer sneller zijn dan parallelle URANS-simulaties voor een simulatieduur van tien omwentelingen. Deze opmerkelijke toename van de rekenkundige snelheid benadrukt het potentieel van DTVPM om efficiënte en nauwkeurige simulaties te bieden voor hybride VAWT's, waardoor verdere vooruitgang in de technologie van windenergie wordt vereenvoudigd.

Deze studie heeft tot doel om de nauwkeurigheid en efficiëntie van de hybride Euleriaanse-Lagrangiaanse methode bij het analyseren van complexe stromingsverschijnselen te verbeteren. Door verschillende scenario's met een hybride VAWT door te lopen met behulp van de hybride methode, sluit deze studie af met de demonstratie van de capaciteit van de hybride solver om de aerodynamica van hybride VAWTs te simuleren. Het uiteindelijke doel van dit proefschrift is het vinden van een efficiënt model voor hybride VAWT en het bepalen van de grenzen van de afzonderlijke Euleriaanse en Lagrangiaanse methoden, door specifiek te kijken naar de stroomingskenmerken van VAWT's. Al met al draagt deze studie bij aan verdere inzichten in de correlatie tussen blad-wervelinteractie en koppelvariatie. De modelleringsuitdaging in de hybride VAWT-simulatie is bestudeerd

en een hybride model wordt voorgesteld om de prestaties en stromingskenmerken van hybride VAWTs te begrijpen.

NOMENCLATURE

2D	Two-dimensional
3D	Three-dimensional
AMI	Arbitrary Mesh Interface
CFD	Computational Fluid Dynamics
PIMPLE	PISO-SIMPLE
PISO	Pressure Implicit with Splitting of Operators
SIMPLE	Semi-Implicit Method for Pressure Linked Equations
SST	Shear Stress Transport
TSR	Tip Speed Ratio
URANS	unsteady Reynolds-Averaged Navier–Stokes
VAWT	Vertical Axis Wind Turbine
ΔC_p	Difference of maximum and minimum pressure coefficients
Δy_1	Distance between cell and the nearest wall
ϵ	Overlap ratio of Savonius blades
γ	Attachment angle
λ_D	Tip speed ratio of Darrieus
λ_S	Tip speed ratio of Savonius
λ_{hybrid}	Tip speed ratio of hybrid VAWT
λ_{max}	Maximum tip speed ratio of rotor
λ_{min}	Minimum tip speed ratio of rotor
μ	Dynamic viscosity
μ_t	Turbulent viscosity
Ω	Rotational speed
ω	Vorticity

Φ	Arc angle of Savonius blade
ρ	Flow density
θ	Phase angle
υ	Kinematic viscosity
$\vec{u}_1$	Induced velocity
$\vec{u}_2$	Shear velocity
C_p	Pressure coefficient
c_p	Power coefficient
c_q	Torque coefficient
$c_{p_{max}}$	Peak power coefficient
e	Gap width
k	Turbulent kinetic energy
p	Pressure
R_1	Semi-major axis of elliptic Savonius blade
R_2	Semi-minor axis of elliptic Savonius blade
R_D	Darrieus rotor radius
R_S	Savonius rotor radius
R_{hybrid}	Radius of hybrid VAWT
u	Sum of mean velocity and fluctuating velocity
U_∞	Inflow velocity
u_τ	Friction velocity
w	Turbulent dissipation rate
x	Coordinate in horizontal axis
y	Coordinate in vertical axis

I

INTRODUCTION

1
INTRODUCTION

1

1.1. RENEWABLE ENERGY ADVANCEMENTS

In recent years, there have been significant advancements in renewable energy technologies, driving the global transition towards sustainable energy sources. Among these, wind energy stands out as a promising avenue for clean power generation [1, 2, 3]. The potential of wind energy lies in its abundance and widespread availability, making it a viable option for countries aiming to reduce dependence on fossil fuels and mitigate climate change. Furthermore, innovations in wind turbine design and manufacturing processes have led to increased efficiency and cost-effectiveness, making wind power increasingly competitive with conventional energy sources [4]. As technology continues to evolve, the scalability and reliability of wind energy systems are expected to improve further, unlocking new opportunities for harnessing the power of the wind to meet growing energy demands.

Climate change is a pressing global issue that has caught increasing attention in recent years [5]. The rise in greenhouse gas emissions, primarily caused by human activities, has led to rising global temperatures, altering weather patterns, and contributing to various environmental hazards. To combat the adverse effects of climate change, the adoption of renewable energy sources has become imperative. Among these sources, wind energy has experienced remarkable growth and plays a pivotal role in mitigating climate change. The scalability, eco-friendliness, and decreasing wind energy costs have contributed significantly to its expansion [6].

1.2. WIND ENERGY DEVELOPMENT

Wind energy has emerged as a leading contender due to its abundant availability, cost-effectiveness, and negligible greenhouse gas emissions. This section aims to provide a comprehensive overview of wind energy development, focusing on its technology, current status, and potential for future growth.

Wind energy technology revolves around the concept of converting kinetic energy from the wind into electrical power through wind turbines. The fundamental components of a wind turbine include rotor blades, a nacelle, a generator, and a tower. As the wind blows, it causes the rotor blades to rotate, transferring the rotational energy to the generator, which then produces electricity. Modern wind turbines are designed with aerodynamically optimized blades, advanced control systems, and efficient gearbox mechanisms to maximize power generation while minimizing maintenance requirements.

Wind turbines can be categorized into two groups: horizontal axis wind turbine (HAWT) and vertical axis wind turbine (VAWT). VAWT received very little engineering development in the 1990s due to the dominance of the HAWT in the wind energy market [7]. Over the past few decades, especially from the mid-2000s, the development of VAWTs has entered the Renaissance period [8] when multiple projects are working to bring VAWTs to the wind market. The project information, e.g., relevant power, installation region, and status are shown in Table 1.1. The VAWT configurations in different projects are depicted in Figure 1.1. VAWTs in offshore wind farms have gained momentum, offering the advantage of high wind speeds, high power rates, and reduced visual impact [9, 10, 11, 12, 13, 14, 15, 16, 17, 18]. Additionally, advancements in VAWT design and

engineering have enabled onshore VAWT installations in areas with low wind speeds, especially hybrid Darrieus and Savonius (hybrid VAWT) [19, 20], further expanding the potential for wind energy utilization.

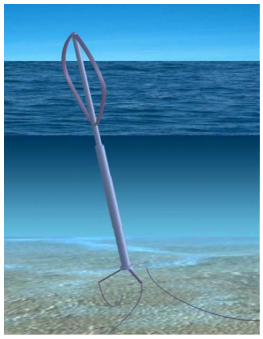

DeepWind [9]

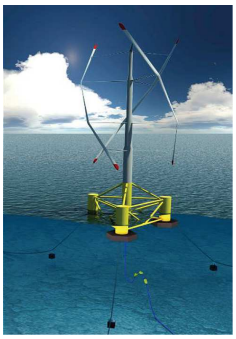

INFLOW (VertiWind) [10, 11]

Gwind [12]

SeaTwirl[13]

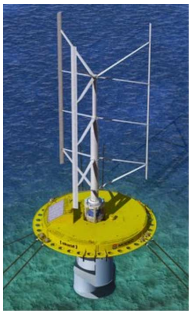

SKWID [14, 15]

Spinfloat [16]

Aerogenerator X [17, 18]

INFLOW [11]

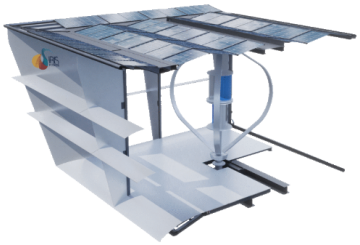

PowerNEST [19]

DS-3000 [20]

Figure 1.1: Multipe projects of VAWTs

Table 1.1: Summary of VAWT projects

Project	Rated power	VAWT configuration	Status	Region
DeepWind [9]	5MW	Darrieus curved blades	Prototype	EU/USA
INFLOW (VertiWind) [10, 11]	2MW	Helical blades	Prototype	EU
INFLOW [11]	2MW	Two rotors with straight blades	Concept	EU
Gwind [12]	NA	Helical blades	Prototype	Norway
SeaTwirl [13]	1MW	Helical blades	Prototype	Sweden
SKWID [14, 15]	0.5MW	Hybrid Darrieus and Savonius	Prototype	Japan
Aerogenerator X [17, 18]	10MW	V-shaped	Concept	UK
Spinfloat [16]	6MW	Straight blades	Concept	France
PowerNEST [19]	3kW	Hybrid Darrieus and Savonius	Prototype	Netherlands
DS-3000 [20]	3kW	Hybrid Darrieus and Savonius	Prototype	China

The deployment of VAWTs in urban areas is attributed to several advantages: low noise, insensitivity to wind conditions, good performance under unstable wind, safety concerns, etc. [21]. Due to a better understanding of the fatigue loads of VAWTs [22, 23], the fatigue issue that hindered the early VAWT installations can now be resolved. Among all types of VAWTs, Savonius and Darrieus and hybrid Darrieus and Savonius rotors are the main representatives. Their detailed information can be found in Section 1.3.1.

1.3. VAWT DEVELOPMENT

1.3.1. TECHNOLOGY OF SAVONIUS AND DARRIEUS VERTICAL AXIS WIND TURBINE

Since the early 2000s, onshore wind turbines have grown in size (both height and blade lengths) and generated more energy [24]. The growth rate continues to increase so that more lands are occupied by wind turbines. To address this issue, the technology of wind turbines has gradually developed in two directions: large-size grid-connected power generation and miniaturization in off-grid power generation. When it comes to the form of wind energy utilization, large-scale grid-connected wind power has become mainstream. However, distributed, discrete, micro-grid, multi-energy complementary, and other forms of wind energy utilization also receive more and more attention in urban applications.

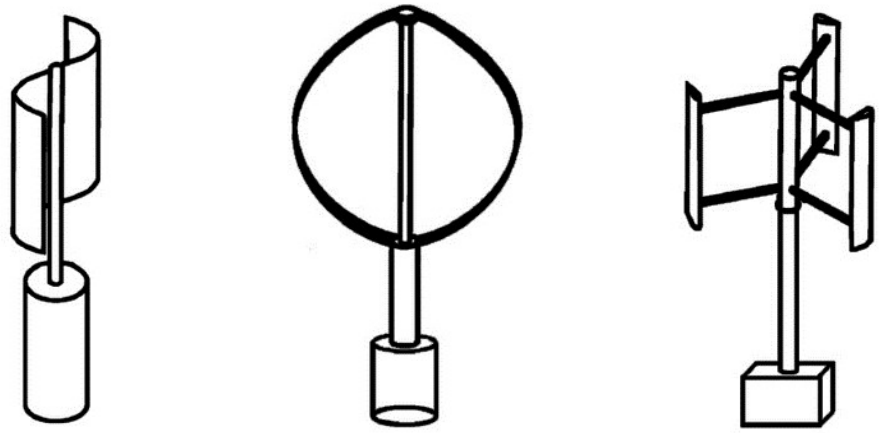

Savonius D-type Darrieus H-type Darrieus

Figure 1.2: Schematic of VAWTs

Table 1.2: Operational conditions of Darrieus and Savonius rotors

Author	VAWT	λ_{min}	λ_{max}	$c_{p_{max}}$
Hosseini et al. [25]	3-bladed Darrieus	1	5	0.48
Castelli et al. [26]	3-bladed Darrieus	1.43	-	0.31
Wang et al. [27]	2-, 3- and 4-bladed Darrieus	~ 0.8	~ 4	~ 0.4
Gosselin et al. [28]	3-bladed Darrieus	1.8	5.2	0.36
Hosseini et al. [25]	Bach-type Savonius	~ 0.6(self-start)	~ 1	0.27
Wekesa et al. [29]	Three-bladed double stage Savonius	~ 0.2(self-start)	~ 1.3	0.18

Three popular VAWT designs for urban environments are the Savonius, D-type Darrieus, and H-type Darrieus see Figure 1.2. The features and operational conditions of these turbines have been investigated in many studies, and some notable studies are listed in Table 1.2. Savonius rotors have the features of simple structure, low noise, and good self-starting performance [30, 25, 29]. These characteristics allow them to be suitable for most small and medium-sized utilizations, for example, to be integrated with residential and commercial buildings for energy production [31]. But Savonius rotors demonstrate a reduced peak power efficiency (0.2-0.3) compared to Darrieus rotors [29]. The maximum power coefficient for the Darrieus rotor is often between 0.4 and 0.5[25, 26, 27, 28].

Among the two types of wind turbines, the start-up performances and power performances are complementary [32]. The concept of a combined Darrieus-Savonius turbine (hybrid VAWT) emerges from combining their advantages, leading to an increase in complexity. This study will focus on the comprehensive investigation of the hybrid VAWT based on its performance and flow features.

1.3.2. TECHNOLOGY OF DARRIEUS-SAVONIUS COMBINED TURBINE

The hybrid concept of a Darrieus and Savonius rotor is expected to highlight the strengths of each configuration and compensate for weaknesses. In order to design an effective hybrid VAWT, many studies have been done. Pallotta et al. [33] proposed a hybrid VAWT able to work on more extended operational conditions compared to the single Darrieus and Savonius. The example configuration of the hybrid VAWT is shown in Figure 1.1. The Darrieus and Savonius parts are mounted in the same shaft. Sun et al. [34] designed a hybrid VAWT and predicted its aerodynamics and starting performance using Computational Fluid Dynamics (CFD) simulations. The distance between the Savonius blades and the center of rotation of the turbine rotor was studied. However, this research only improved the start-up performance of the hybrid VAWT. The power coefficient of this turbine was lower than that of the Darrieus VAWT. Mohamed [35] studied the effect of mutable solidity and tip speed ratio on the performance of a hybrid turbine system. Previous numerical studies indicate that the start-up performance is no doubt improved instead of power output. However, an efficient model for the hybrid VAWT is yet to be explored. The numerical modeling of VAWTs should be further investigated in more complex cases, especially hybrid VAWT systems, to extend the application of the efficient and accurate method and contribute to the hybrid VAWT design. Section 1.4.4 will discuss multi-fidelity models for the hybrid VAWT.

Additionally, it is worth investigating the correlation between blade forces/power output and the flow mechanism of the hybrid VAWT, which has not been comprehensively studied in previous studies. The flow field of the hybrid VAWT is complex due to the blade-vortex interaction of Darrieus and Savonius blades, particularly when blades pass through the shed wake. Despite its good start-up performance, the power coefficient is a relevant issue. Various factors can affect the power output of the hybrid VAWT, including airfoil efficiency, tip speed ratio, and rotor shape.

1.3.3. POWER PERFORMANCE ANALYSIS

The evaluation of power performance in hybrid VAWTs is a fundamental aspect of understanding their operational efficiency and potential contribution to renewable energy generation. The torque-based power coefficient c_p is the most common parameter utilized to quantify the power output of these turbines. It is calculated by Equation 1.1, where Q is the turbine's torque, Ω is the turbine's rotational speed, U_∞ is inflow velocity, and A is the turbine's swept area. It provides insights into the turbine's ability to convert available wind energy into mechanical power. The maximum power coefficient of any turbine cannot exceed 16/27, known as Betz limit [36]. Studies focused on power performance delve into the dependency of c_p on factors such as tip speed ratio, wind speed, and turbine geometry [37, 38, 39, 35, 40].

$$c_p = \frac{Q\Omega}{0.5\rho U_\infty^3 A} \tag{1.1}$$

1.3.4. FLOW FEATURE ANALYSIS

The flow phenomena unique to hybrid VAWTs, including vortex interactions and wake characteristics, are discussed in this section. The intricate flow phenomena and aerodynamic characteristics inherent to hybrid VAWTs present a promising research area. These turbines combine the distinctive aerodynamic traits of both Darrieus and Savonius rotor designs, leading to a complex flow patterns that significantly impact the hybrid VAWT performance. Liu et al. [41] conducted a fluid-structure interaction study on a hybrid Darrieus-Modifed-Savonius VAWT (HDMS). Results show a penalty on the power coefficient when the size of the inner Savonius increases and/or the tip speed ratio decreases. The vorticity fields of this hybrid design with different tip speed ratios are shown in Figure 1.3. Additionally, the wake dynamics of the Darrieus rotor, with its dynamic stall behavior, contribute to the challenges of optimizing the hybrid VAWT's performance.

Understanding vortex interactions and wake characteristics is pivotal for enhancing turbine performance and operational efficiency. By characterizing these complex flow patterns and understanding their implications, researchers can optimize turbine designs, optimize control strategies, and mitigate adverse effects on power performance. Ultimately, a profound grasp of flow phenomena and aerodynamics is essential for unlocking the full potential of Darrieus-Savonius hybrid VAWTs as a reliable and efficient renewable energy source.

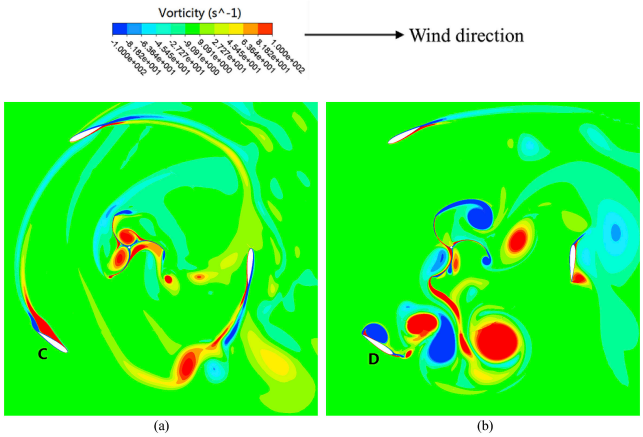

Figure 1.3: Vorticity fields of the hybrid VAWT (a) when c_p = 41% (TSR=2.3); (b) and when c_p = 2% (TSR=0.5) [41]

1.4. NUMERICAL MODELING DEVELOPMENT

1.4.1. ADVANCES AND CHALLENGES IN VAWT MODELING

Numerical modeling plays a crucial role in the design, optimization, and performance evaluation of VAWTs. By employing computational fluid dynamics (CFD) techniques, engineers can simulate the complex flow phenomena around VAWTs, including turbulence, vortex shedding, and boundary layer effects [42]. These simulations provide valuable insights into the aerodynamic behavior of VAWTs, allowing designers to optimize blade shapes, rotor configurations, and operational parameters for maximum energy capture and efficiency. Additionally, numerical models enable the assessment of wake interactions and structural loads, facilitating the development of robust and reliable wind turbine systems [43]. With advances in computational power and simulation techniques, numerical modeling continues to play a pivotal role in advancing VAWT technology and driving innovation in the renewable energy sector.

Numerical modeling of VAWTs also poses several challenges due to the inherent complexity of the flow physics involved. One major challenge is accurately capturing the unsteady aerodynamic behavior of VAWTs, including dynamic stall, vortex shedding, and wake interactions, which can significantly impact turbine performance [32]. Additionally, resolving the boundary layer near the turbine blades poses computational challenges, particularly in regions of separation and flow reattachment. Furthermore, the three-dimensional (3D) and transient nature of the flow around VAWTs demands substantial computational resources. All of this limits the efficient prediction of VAWT performance [44]. Efficient simulation enables the exploration of a wider design space, facilitating innovation and the development of next-generation VAWT technologies. It reduces computational costs and time-to-results, enabling faster design iterations and decision-making processes. Moreover, validating numerical models against experimental data remains challenging, as wind turbine experiments are often conducted under controlled but simplified conditions, making direct comparison with simulation results

complex [45, 46]. Despite these challenges, advancements in numerical techniques continue to improve the accuracy and efficiency of VAWT simulations, driving progress in wind turbine design and optimization.

1.4.2. NUMERICAL METHODS FOR SAVONIUS

Different computational methods have been used to address Savonius' unsteady flow problem. Korprasertsak [47] designed a wind booster for a Savonius rotor using XFLOW CFD software with Wall-Adapting Local-Eddy (WALE) turbulence model. This booster configuration improves the power efficiency and has a good agreement with experimental results. Kacprzak [48] examined the performance of conventional and modified Savonius rotors employing ANSYS CFX with shear stress transport (SST) k-ω turbulence model. Other high-fidelity methods, such as large eddy simulation (LES) and detached eddy simulation (DES), are expected to give more accurate predictions, especially on flow characteristics with massive flow separation. Gao [49] and Lee [50] studied the turbine performance and wake structures of a hydrokinetic Savonius turbine using LES accompanied by a prototype experiment for validation. Although their simulations help to address step-by-step changes in the blade shape and operating tip speed ratio during optimization design process, it is reported in the literature that one simulation of 1.8m long, 0.3m wide and 0.54m deep computational domain needs around 1800h with 768 cores on the supercomputer. Dobrev [51] analyzed the performance and wake evolution of a Savonius rotor by means of unsteady Reynolds averaged Navier Stokes (URANS) and DES, revealing that the capability of DES gives more comparable rotor power and flow structures with experiments. Elkhoury [52] studied effects of wind speed, aspect ratio, inflow angle on the performance of an orthopter-type VAWT using delayed detached eddy simulation (DDES). It is perceived that DDES can properly predict power coefficient of turbine along with the related 3D vortical flow structures. Antar [53] utilized 2D RANS and 3D DDES in the parametric optimization process for a Savonius rotor with guided plate configuration. Their results show that DDES can perfectly replicate the power performance curve and RANS can be seen as an alternative to avoid costly parametric processes. These numerical tools could give accurate predictions for unsteady flows. However, these CFD applications require extremely fine grids to simulate the boundary layer flow and large computational domains to ensure accurate solutions. It is inefficient concerning time and resources.

In addition to the blade-resolved method, there exist alternative methodologies with reduced computational time. Among these, the vortex-based method stands out as a viable option, effectively striking a balance between the trade-offs involving computational cost and fidelity. Ogawa [54] modeled the Savonius rotor by the discrete vortex method. It is reported that the numerical results do not show a quantitative agreement with experiments but yield a qualitative explanation of the wake pattern. Ueda [55] solved the boundary integral equation and Bernoulli's equation using a vortex panel method to calculate the automated S-shaped rotor. The load-free rotor starts from a static state and reaches stable rotations. The results show that the vortex shedding and reattachment play a key role in toque variation. These methods are less computationally expensive than the above CFD applications but have a deficiency in capturing boundary layer flow.

1.4.3. NUMERICAL METHODS FOR DARRIEUS

Researchers have explored different models that can effectively estimate the power output and vortex dynamics for the Darrieus turbine. To analyze the complex and unsteady aerodynamic flow associated with wind turbine operation, computational fluid dynamics (CFD) is an attractive and powerful method [56, 57]. Almohammadi [58] studied the effect of the trailing edge profile on the performance of the straight-blade-VAWT using CFD methods. It is observed that the trailing edge profile may play a significant role in improving the turbine performance and should be accurately accounted for in the design process of the straight-blade-VAWT. Ferreira [8] evaluates the differences between the different commonly used turbulence models (Laminar, Spalart-Allmaras and k-ϵ) in a 2D Darrieus case. The results show a good agreement with the PIV field data.

However, the high computational cost of CFD simulation limits studies on the aerodynamic performance of wind turbines due to the requirement of excessive computational resources. Alternative computational methods are explored for development purposes in many studies. The vortex method [59, 60, 61, 62] is a mesh-free method in which the vorticity is carried by particles. And the vortex particles could be located at places where the vorticity exists to reduce computation time and resources. U2DiVA [63] is a two-dimensional vortex model that can capture the wake structure by dividing the near-wake and far-wake fields. In this method, the near wake is modeled as constant strength doublet panels, while the far wake is modeled with vortex points. That reduces computation time and is validated to be more accurate than a conventional Double Multiple Streamtube model. Zanon [64] developed a double wake vortex panel method for the physics of dynamic stall in a 2D VAWT. The results have a good agreement in both attachment and separated flow conditions. Dyachuk [65] coupled a streamtube model with a modified dynamic stall model for a wide range of VAWT operations. Although this model does not reproduce every case in great detail, it can be used for preliminary estimations of blade forces due to its high computational speed and reasonable accuracy.

1.4.4. NUMERICAL METHODS FOR HYBRID VAWT

The modeling of the hybrid VAWT plays an important role in predicting the turbine performances and developing stages such as design, construction, and operation. In recent years, many studies have been conducted to develop numerical models for hybrid VAWT. Chegini et al. [66] investigated the self-starting performances of a hybrid VAWT and techniques of power performance enhancement (deflectors). A 2D computational fluid dynamics (CFD) approach was used to simulate the hybrid VAWT. The complex flow around the turbine and transient blade forces were obtained by solving the unsteady Reynolds-Averaged Navier-Stokes (URANS) equations. Pouransari et al. [67] examined the performances of three hybrid VAWTs using a numerical approach to solve the three-dimensional (3D) URANS equations. The results revealed the optimal Savonius position is on top of the Darrieus. Irawan et al.[68] studied the improvements of the hybrid VAWT using the CFD approach. 2D URANS equations were solved to obtain the complex flow problems in Ansys Fluent. The results showed power improvements can be achieved up to 50% higher by changing the turbine rotation mode compared to the conventional hybrid VAWT. Fertahi [69] used the URANS coupled with SST k-ω turbulence model to study the power performances of a 3D vertical tidal turbine. It is found that the asyn-

chronous coupling of Savonius and Darrieus (identical rotational direction for the two rotors) provides effective performances compared with other studied hybrid configurations. The mesh has 0.34 million elements and a sufficiently small physical time step has been used for the investigated turbines. Liang [40] investigated the aerodynamic performance of a 2D hybrid VAWT using ANSYS Fluent. About 1 million elements were employed in the simulations with an average deviation of 7% compared with the finest studied case.

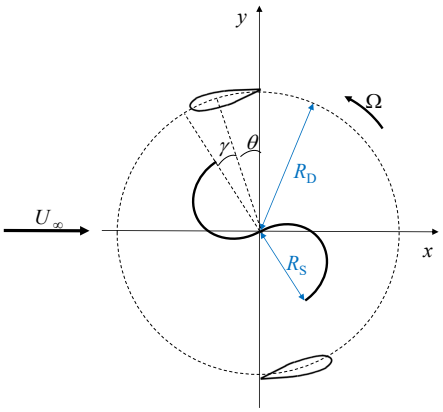

Figure 1.4: Schematic of a hybrid VAWT with two semi-circular Savonius blades and two Darrieus blades

The complexity of the above numerical models increases with the need to acquire knowledge of blade-vortex interactions and blade forces. In principle, most of these numerical models are based on the real geometry of the turbine blade. However, it is obvious that the blade rotation can be interpreted as forces acting on the flow, and the turbine power is determined by the force distribution along the rotation path in Figure 1.4. The flow models of the hybrid VAWT remain a challenge. The motivation of this work is to extend the knowledge of wind energy conversion using a hybrid VAWT flow model.

1.4.5. WIND TURBINE FLOW MODELS

The previous sections have briefly reviewed the numerical modeling for VAWTs. This study aims to understand the flow features and power performance of a hybrid VAWT using (hybrid) flow models. Wind turbine flow models can be classified into kinematic models and dynamic models according to the boundary conditions [70]. The vortex model is popular in the group of kinematic models. It solves the potential flow problem using the Neumann boundary condition on the impermeable surface. Besides, the time rate of circulation change in a control volume is conserved as zero. Ferreira [63] conducted 2D and 3D potential flow simulations to gain insights into the aerodynamics of VAWT. Jin et al. [71] investigated 2D unsteady flows around polygons using a vortex method. The kinematic models are quite complex due to the necessity of solving the unsteadiness of flow.

The dynamics models have been widely used due to their simplicity. They are based on the momentum conservation. Mohammed [72] provided a review of various momentum models used in the aerodynamic modeling of Darrieus rotors. It discusses three streamtube models: single streamtube (SST), multiple streamtube (MST), and double multiple streamtube (DMST). The former two models have the same problem that a constant velocity along the streamtube is assumed. DMST overcomes this problem by accounting for the velocity variation along the streamtube. However, it has a convergence issue at high tip speed ratios. Froude [73] originally proposed an actuator disk model for horizontal axis wind turbines (HAWTs). This simplified model is commonly employed for propellers or HAWTs, representing a permeable surface with uniformly distributed forces. The flow induced by this force distribution is characterized by shedding vorticity. In the case of VAWTs, where the blade path follows a circular trajectory, the information available is limited to the streamwise direction using the actuator disk model. Madsen [74] proposed an alternative actuator cylinder model for VAWTs, distributing forces along a cylindrical surface. Both actuator models are created based on the blade forces acting on the fluid and ignorance of the diffusion. However, these models neglect the diffusivity, which addresses how fluid motion is damped behind the hybrid VAWT.

In this work, the VAWT can be modeled as a fundamental formulation of a force field by excluding geometrical and operational effects (airfoil shape, rotor shape, installation position of each component and tip speed ratio). To estimate the power performance for the hybrid force field (idealized hybrid VAWT), concepts of the actuator disk and actuator cylinder can be introduced to resolve the flow around an idealized hybrid VAWT. The inner Savonius and the outer Darrieus can be modeled using an actuator disk and actuator cylinder with uniform loading. This approach allows us to examine the power gain or loss of the hybrid VAWT in an ideal simulation with varied actuators' locations and force distributions.

1.4.6. HYBRID METHOD FOR AIRFOIL APPLICATIONS

A cost-effective model plays a vital role in the accurate and efficient prediction of the force and flow fields.

Since the Eulerian and Lagrangian solvers are complementary in the modeling techniques, an alternative approach is to divide the computation domain into two regions and apply these two solvers according to the flow characteristics present in each region. By employing the hybrid solver, it is possible to accurately and effectively resolve the flow in boundary layers and capture the wake flow. Following this idea, researchers have spared no efforts to develop the hybrid Eulerian-Lagrangian solver.

Cottet et al. [75] firstly derived a combined particle method and finite difference method to analyze the high Reynolds number flow. The domain decomposition idea is to divide the domain into two subdomains that overlap for the computation of vorticity and velocity. Geurmond et al. [76] proposed a hybrid solver dividing the domain into two subdomains without overlapping. The stream function and vorticity formulation are solved within these two independent subdomains. Besides, the transmission condition is required on the interface. This method can be extended to a pressure-related case. Ould-Salihi et al. [77] described and illustrated numerical procedures that combine grid and particle solvers for the solution of the incompressible Navier–Stokes equations.

More recently, some hybrid approaches have been proposed that could avoid the classical alternating Schwartz procedure. Daeninck [78] considered the whole computational domain as the Lagrangian subdomain, and the near-wall region as the Eulerian subdomain. In this approach, they used the Lagrangian vortex method to solve the entire flow and then captured the detailed wall features using a grid-based solver in the near-wall region. This Eulerian information was used to correct the Lagrangian method in the near-wall region. At last, use the Lagrangian domain to obtain the boundary condition on the Eulerian domain. This is an approach using a Lagrangian vortex element method to resolve the boundary layer regions by calling an Eulerian grid-based solver. However, linear interpolation was used in their approach. It is quick and easy, but not very precise. Stock et al. [79] proposed a modification of the previous approach by Daeninck [78]. Instead of using linear interpolation to obtain the interface boundary conditions, Stock et al. solved the BEM (Boundary Element Moment Method) equations [80] for the unknown surface element vortex strengths, avoiding interpolation errors within the viscous boundary layer. Palha et al. [81] decomposed the computational domain the same as Daeninck [78] and Stock et al. [79], but took a slightly different computation approach. Instead of focusing on exactly matching the solution of both solvers in the overlap region, the Eulerian solution was used to correct the Lagrangian one in the near-wall region. Billuart [82] coupled the body-fitted near-wall solver and a Vortex-Particle-Mesh method. The correction scheme of the vorticity field for the vortex method by the near-wall Eulerian field is simply applied to guarantee global conservation of the circulation. Hence, no additional wall treatment is required in the Vortex-Particle-Mesh method. It is noted that all of the research above used the decomposition method and applied different solvers in subdomains. Huntley et al. [83] proposed a hybrid method that couples a RANS solver with a vortex particle method (VPM). The domain was not decomposed into regions; instead, the VPM is used to approximate the flow solution, and the CFD is used to calculate the difference between the approximation and the flow field. This is done by including the influence of the particles in the CFD solution through the split velocity method, which has previously been used in the simulation of gusts [84, 85].

By employing the hybrid solver, it is possible to accurately and effectively resolve the flow in boundary layers and capture the wake flow. This dissertation will analyze the flow features and power performance of VAWTs using the hybrid Eulerian-Lagrangian model.

1.4.7. Summary of VAWT modeling

Multi-fidelity computational methods used to study flow dynamics and power performances in VAWTs have been discussed.

This section discusses the three principal types of numerical models used in this thesis: Eulerian URANS, Lagrangian VPM, and hybrid Eulerian-Lagrangian model. Each of these types of models bears distinct strengths and weaknesses in the context of investigating the complexities associated with hybrid VAWTs.

Eulerian URANS

Eulerian URANS models command a prominent presence within the computational fluid dynamics (CFD) domain [86]. They are well-suited for addressing the specific complexity presented by hybrid VAWTs. Notably, the URANS model excels in the simulation and

analysis of fluid flow, accurately capturing intricate flow dynamics—including the vortex development, wake interactions, and turbulence to understand turbine behavior.

LAGRANGIAN VPM

The Lagrangian vortex model, as an innovative computational technique, distinguishes itself through its capacity to offer computational efficiency without compromising too much accuracy in modeling flow phenomena [87]. It discretizes the fluid domain into vortex particles (or other elements), which accurately represent vortices and their dynamics. This method is particularly suited to capture the vortex interactions and shedding behavior that is characteristic of hybrid VAWTs. It provides an efficient way of modeling flow characteristics that influence power performance.

HYBRID EULERIAN-LAGRANGIAN MODEL

The rationale behind Eulerian URANS and Lagrangian VPM has been discussed in this study. Each model contributes to capturing different aspects of flow and performance. Since the Eulerian and Lagrangian models are complementary in the simulation techniques, the computation domain is divided into two regions to which these two solvers are applied according to the flow characteristics present in each region [88]. Pasolari et al. [89] integrated a vortex particle method with a finite volume solver through the use of a domain decomposition technique. The findings indicated strong concordance with the outcomes of comprehensive Eulerian simulations. By employing the hybrid model, it is possible to accurately and effectively resolve the flow in boundary layers and capture the wake flow.

The integration capitalizes on the unique strengths of URANS and VPM. URANS facilitates high-fidelity flow analysis compared to VPM, VPM introduces computational efficiency in modeling vortex-related phenomena, and the Eulerian-Lagrangian model demonstrates its capability of hybrid VAWTs simulations.

1.4.8. TWO-DIMENSIONAL (2D) SIMULATIONS FOR VAWTS

Over the past few years, the growth in computational capabilities has paved the path for tackling the computation of VAWTs using computational fluid dynamics (CFD). However, these simulations require an expensive computational investment, resulting in this method still impractical for design objectives. As a result, researchers have turned to simplified two-dimensional (2D) models, which significantly reduce computational demands. The two-dimensional (2D) blade-resolved simulations can capture the primary vortex dynamics and yield comparable trends in quantitative results for VAWTs (e.g., streamwise velocity, blade force) [90, 91]. Fatahian et al. [92] investigated the flow dynamics and rotor performance of a vented Savonius using 2D unsteady simulation in ANSYS Fluent. The numerical results of the rotor aerodynamic performance exhibited similar trends to the experimental results [93]. Li et al. [94] studied the wave-turbine interaction of a Savonius hydrokinetic turbine using 2D simulations in STAR-CCM+. The simulated wave evolution was validated against the theoretical and experimental values. Results indicated that the turbine diameter and blade number will affect the turbine efficiency. Vigneswaran et al. [95] explored the effect of co-flow jet velocity, injection height, and injection mass flow rate on the aerodynamic coefficient of a 2D co-flow jet (CFJ) airfoil in ANSYS Fluent. Results showed that the jet velocity played a significant role in

affecting the aerodynamic coefficient of CFJ airfoils. The studied geometrical parameter (attachment angle, radius ratio) and operational parameter (tip speed ratio) are all 2D parameters. With the aim of characterizing the flow features of the hybrid VAWT and conducting a cost-effective parametric study, 2D simulations are considered sufficient in this study.

1.5. RESEARCH MOTIVATION

The complex aerodynamics of the hybrid VAWTs raise a challenge of multiple phenomena, such as unsteady flows, dynamic stall, massively separated flow, blade vortex interaction, rotor wake interaction, and wake development. Such complexity results in either inaccurate and/or computationally expensive models. This is an excellent study case for a multi-fidelity hybrid modeling approach. The motivation of this research is to explore a more efficient approach to model the fundamental processes of the flow across different levels of complexity. The varying complexities within flow dynamics and the diverse levels of precision needed for design analysis prompt us to explore a multi-fidelity approach, *a hybrid model of the hybrid rotor*.

1.6. RESEARCH QUESTIONS

This research aims to investigate hybrid VAWT aerodynamics and the numerical modeling of the 2D unsteady flow around the turbine, exploring a cost-effective numerical tool that can support design. To understand the performance of various types of VAWTs with an efficient method, the following research questions need to be answered in this work.

1. How to simplify the hybrid VAWT into its fundamental formulation as a hybrid force field?
    (a) What are the benefits of hybrid VAWT configuration using the fundamental formulation?
    (b) How well can the hybrid force field predict the performance and flow dynamics of a hybrid VAWT?
    (c) What is the effect of force fields on VAWT performance?
    (d) What is the effect of force fields on wake aerodynamics?
2. How well can an Eulerian URANS model predict the performance and flow dynamics of a hybrid VAWT?
    (a) How to use a URANS model to simulate a hybrid VAWT?
    (b) Can we simulate the flow dynamics of hybrid VAWT that fall outside the scope of the fundamental hybrid force model?
    (c) What is the correlation between blade-vortex interaction and blade force variation?
3. How well can a Lagrangian vortex model predict the key performance parameters of VAWTs?

   (a) How to use vortex methods to simulate individual VAWTs?

   (b) How to consider flow viscosity using vortex methods?

   (c) What is the computational accuracy and efficiency of vortex methods compared to high-fidelity simulations in the case of a Savonius rotor?

4. How well can a Lagrangian vortex model be applied to the hybrid VAWT?

   (a) How can the vortex methods include flow viscosity in hybrid VAWT?

   (b) How well can the vortex methods simulate the hybrid VAWT?

5. What is the most simple and efficient way to model the hybrid VAWT in terms of its performance, loads, and vortical structures?

   (a) How well can the Eulerian method be coupled with the Lagrangian method?

   (b) How well can the hybrid solver simulate a hybrid VAWT?

1.7. THESIS OUTLINE

This thesis consists of six parts: Introduction, Eulerian method, Lagrangian method, Eulerian-Lagrangian method, Conclusion, and Appendix. The work studies VAWT aerodynamic performance using various methods. The thesis outline is depicted in Figure 1.5.

Part I: Introduction

This part provides the research background, research objectives and research questions.

Chapter 1: This chapter introduces the motivation of the thesis. It states the necessity of VAWT modeling and development. Besides, the VAWT technology and VAWT modeling is reviewed. The power performance and flow feature of Savonius, Darrieus and hybrid VAWT are recognized as key parameters of VAWT design. The challenges and potential of various numerical tools (Eulerian method, Lagrangian method, Eulerian-Lagrangian method) are summarized. An overview of the thesis and research questions are also provided.

Part II: Eulerian method

In Part II, the aerodynamics and performance of various types of VAWTs are discussed and predicted using (U)RANS. It reveals the possibility of getting more power gain from hybrid VAWT compared to a single Darrieus. The blade force variation and detailed flow fields are also studied.

Chapter 2: This chapter simplifies VAWTs as fundamental formulations with uniform force fields. It studies the effect of force fields on VAWT performance and wake aerodynamics. The implications for a hybrid VAWT study are also shown in this chapter.

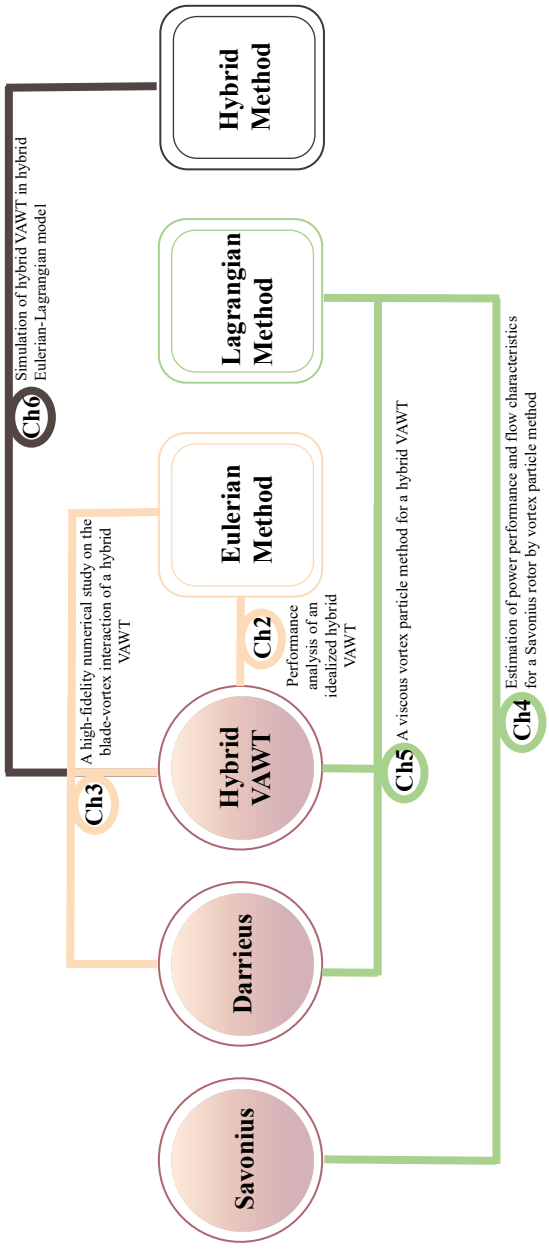

Figure 1.5: Graphical outline of thesis

Chapter 3: This chapter conducts a study of blade-vortex interaction using the unsteady Reynolds averaged Navier-Stokes (URANS). The geometrical and operational parameters are studied for the hybrid VAWT. The numerical results are validated against the literature. This chapter serves URANS as a baseline method for the validation of the following chapters.

Part III: Lagrangian method

Part III consists of the study on various types of VAWTs using Lagrangian method: vortex particle method. It evaluates the computational accuracy and efficiency based on the Eulerian method.

Chapter 4: Vortex method is studied in detail with a focus on how this method can be applied and adapted to the 2D Savonius. The vortex method's strengths and weaknesses are discussed through comparison with OpenFOAM. A double-trailing-edge-wake-modeling method (DTVPM) is proposed to simulate Savonius with reasonable cost-effectiveness.

Chapter 5: Darrieus and hybrid VAWT are simulated using vortex method. It takes into account the flow viscosity. This chapter shows the capability of vortex methods in predicting hybrid VAWT performance.

Part IV: Eulerian-Lagrangian method

Part IV combines the Eulerian and Lagrangian methods as a hybrid method to study the flow fields of hybrid VAWTs.

Chapter 6: This chapter is concerned with the simulation of an idealized hybrid VAWT case using the coupled Eulerian-Lagrangian method. The capability of the hybrid method in hybrid VAWT case is summarized.

Part V: Conclusion

Part V concludes the work on hybrid VAWT modeling and provides guidance for the future direction of hybrid VAWT design.

Chapter 7: The thesis is summarized in this chapter. In addition, an outlook on this project is also discussed.

Part VI: Appendix

Part VI provides additional details about the sensitivity study of the above methods.

REFERENCES

[1] K. Mason, J. Duggan, and E. Howley. Forecasting energy demand, wind generation and carbon dioxide emissions in Ireland using evolutionary neural networks. *Energy* 155 (2018), pp. 705–720.

[2] M. Abdullah-Al-Mahbub and A. R. M. T. Islam. Sustainable wind energy potential in Sandwip and Kalapara coastal regions of Bangladesh: A way of reducing carbon dioxide emissions. *Heliyon* 10.1 (2024), e23982.

[3] K. Hashimoto. *Current Situation of Energy Consumption and Carbon Dioxide Emissions of Our World*. 2019.

[4] P. Veers, C. Bottasso, L. Manuel, J. Naughton, L. Pao, J. Paquette, A. Robertson, M. Robinson, S. Ananthan, A. Barlas, A. Bianchini, H. Bredmose, S. G. Horcas, J. Keller, H. A. Madsen, J. Manwell, P. Moriarty, S. Nolet, and J. Rinker. Grand Challenges in the Design, Manufacture, and Operation of Future Wind Turbine Systems (Apr. 2022).

[5] J. M. Carlson, H. Kaull, M. Steinhauer, A. Zigarac, and J. Cammarata. Paying attention to climate change: Positive images of climate change solutions capture attention. *Journal of Environmental Psychology* 71 (2020), p. 101477.

[6] M. Farghali, A. I. Osman, Z. Chen, A. Abdelhaleem, I. Ihara, I. M. A. Mohamed, P.-S. Yap, and D. W. Rooney. Social, environmental, and economic consequences of integrating renewable energies in the electricity sector: a review. *Environmental Chemistry Letters* 21.3 (Mar. 2023), pp. 1381–1418.

[7] B. Hand and A. Cashman. A review on the historical development of the lift-type vertical axis wind turbine: From onshore to offshore floating application. *Sustainable Energy Technologies and Assessments* 38 (2020), p. 100646.

[8] C. S. Ferreira, G. van Bussel, and G. V. Kuik. *2D CFD Simulation of Dynamic Stall on a Vertical Axis Wind Turbine: Verification and Validation with PIV Measurements*. 2007.

[9] DeepWind. “http://www.deepwind.eu/”.

[10] M. Cahay, E. LUQUIAU, and C. Smadja. Use of a Vertical Wind Turbine in an Offshore Floating Wind Farm. *Offshore Technology Conference, Proceedings* 3 (May 2011).

[11] INFLOW. “Industrialization Setup of a Floating Offshore Wind Turbine”. https://www.inflow-fp7.eu/.

[12] Gwind. “http://www.gwind.no/”.

[13] S. AB. “http://seatwirl.com/”.

[14] SKWID. Floating Wind & Current Hybrid Power Generation - Savonius Keel & Wind Turbine Darrieus (2013).

[15] *Floating Axis Wind and Water Turbine for High Utilization of Sea Surface Area: Design of Sub-Megawatt Prototype Turbine*. Vol. Volume 8: Ocean Renewable Energy. International Conference on Offshore Mechanics and Arctic Engineering. June 2013, V008T09A083.

[16] EOLFI. “http://www.eolfi.com/”.

[17] M. Collu, F. P. Brennan, and M. H. Patel. Conceptual design of a floating support structure for an offshore vertical axis wind turbine : the lessons learnt. *Ships and Offshore Structures* 9.1 (Jan. 2014), pp. 3–21.

[18] A. Shires. Development and Evaluation of an Aerodynamic Model for a Novel Vertical Axis Wind Turbine Concept. *Energies* 6.5 (2013), pp. 2501–2520.

[19] PowerNEST. “https://ibispower.eu/powernest/”.

[20] Hi-VAWT-Technology. “http://www.hi-vawt.com.tw/en/ds3000w.html”.

[21] R. Kumar, K. Raahemifar, and A. S. Fung. A critical review of vertical axis wind turbines for urban applications. *Renewable and Sustainable Energy Reviews* 89 (2018), pp. 281–291.

[22] S. Eriksson, H. Bernhoff, and M. Leijon. Evaluation of different turbine concepts for wind power. *Renewable and Sustainable Energy Reviews* 12.5 (2008), pp. 1419–1434.

[23] H. J. Sutherland, D. E. Berg, and T. D. Ashwill. *A Retrospective of VAWT Technology*. Tech. rep. Sandia National Laboratories.

[24] R. Wiser, M. Bolinger, B. Hoen, D. Millstein, J. Rand, G. Barbose, N. Darghouth, W. Gorman, S. Jeong, and B. Paulos. *Land-Based Wind Market Report: 2022 Edition*. Tech. rep. U.S. Department of Energy, 2022.

[25] A. Hosseini and N. Goudarzi. Design and CFD study of a hybrid vertical-axis wind turbine by employing a combined Bach-type and H-Darrieus rotor systems. *Energy conversion and management* 189 (2019), pp. 49–59.

[26] M. Raciti Castelli, G. Ardizzon, L. Battisti, E. Benini, and G. Pavesi. "Modeling strategy and numerical validation for a Darrieus vertical axis micro-wind turbine". In: *ASME International Mechanical Engineering Congress and Exposition*. Vol. 44441. 2010, pp. 409–418.

[27] Y. Wang, X. Sun, X. Dong, B. Zhu, D. Huang, and Z. Zheng. Numerical investigation on aerodynamic performance of a novel vertical axis wind turbine with adaptive blades. *Energy Conversion and Management* 108 (2016), pp. 275–286.

[28] R. Gosselin, G. Dumas, and M. Boudreau. Parametric study of H-Darrieus vertical-axis turbines using CFD simulations. *Journal of Renewable and Sustainable Energy* 8.5 (2016).

[29] D. W. Wekesa, C. O. Saoke, and J. N. Kamau. An experimental investigation into performance characteristics of H-shaped and Savonius-type VAWT rotors. *Scientific African* 10 (2020), e00603.

[30] T. Chen and Y. Chen. Developing a Vortical Stator Assembly to Improve the Performance of Drag-Type Vertical-Axis Wind Turbines. 31 (2015), pp. 693–699.

[31] C. Jian, Z. Zhou, and H. Xu. Research status of drag-type vertical axis wind turbine. *Energy Engineering* (2017).

[32] F. Scheurich and R. E. Brown. Effect of Dynamic Stall on the Aerodynamics of Vertical-Axis Wind Turbines. *AIAA Journal* 49.11 (Nov. 2011), pp. 2511–2521.

[33] A. Pallotta, D. Pietrogiacomi, and G. P. Romano. HYBRI – A combined Savonius-Darrieus wind turbine: Performances and flow fields. *Energy* 191 (2020), p. 116433.

[34] X. Sun, Y. Chen, Y. Cao, G. Wu, Z. Zheng, and D. Huang. Research on the aerodynamic characteristics of a lift drag hybrid vertical axis wind turbine. *Advances in Mechanical Engineering* 8 (2016), pp. 1–11.

[35] M. Mohamed. Impacts of solidity and hybrid system in small wind turbines performance. *Energy* 57 (Aug. 2013), pp. 495–504.

[36] A. Betz. *Introduction to the Theory of Flow Machines*. Oxford: Pergamon Press. 1966.

[37] R. Gupta and A. Biswas. CFD analysis of flow physics and aerodynamic performance of a combined three-bucket Savonius and three-bladed Darrieus turbine. *International journal of green energy* 8.2 (2011), pp. 209–233.

[38] S. Bhuyan and A. Biswas. Investigations on self-starting and performance characteristics of simple H and hybrid H-Savonius vertical axis wind rotors. *Energy Conversion and Management* 87 (2014), pp. 859–867.

[39] M. Zemamou, M. Aggour, and A. Toumi. Review of savonius wind turbine design and performance. *Energy Procedia* 141 (2017), pp. 383–388.

[40] X. Liang, S. Fu, B. Ou, C. Wu, C. Y. Chao, and K. Pi. A computational study of the effects of the radius ratio and attachment angle on the performance of a Darrieus-Savonius combined wind turbine. *Renewable energy* 113 (2017), pp. 329–334.

[41] K. Liu, M. Yu, and W. Zhu. Enhancing wind energy harvesting performance of vertical axis wind turbines with a new hybrid design: A fluid-structure interaction study. *Renewable Energy* 140 (Sept. 2019), pp. 912–927.

[42] S.-Y. Lin, Y.-Y. Lin, C.-J. Bai, and W.-C. Wang. Performance analysis of vertical-axis-wind-turbine blade with modified trailing edge through computational fluid dynamics. *Renewable Energy* 99 (Dec. 2016), pp. 654–662.

[43] H. Asmuth, G. P. Navarro Diaz, H. A. Madsen, E. Branlard, A. R. Meyer Forsting, K. Nilsson, J. Jonkman, and S. Ivanell. Wind turbine response in waked inflow: A modelling benchmark against full-scale measurements. *Renewable Energy* 191 (May 2022), pp. 868–887.

[44] D. K. R. G, M. Verma, and A. De. Performance analysis of vertical-axis wind turbine clusters: Effect of inter-turbine spacing and turbine rotation. *Physics of Fluids* 35.10 (Oct. 2023).

[45] M. Hmedi, E. Uzunoglu, C. Zeng, J. F. Gaspar, and C. Guedes Soares. Experimental Challenges and Modelling Approaches of Floating Wind Turbines. *Journal of Marine Science and Engineering* 11.11 (Oct. 2023), p. 2048.

[46] P. Chen, J. Chen, and Z. Hu. Review of Experimental-Numerical Methodologies and Challenges for Floating Offshore Wind Turbines. *Journal of Marine Science and Application* 19.3 (Sept. 2020), pp. 339–361.

[47] N. Korprasertsak and T. Leephakpreeda. Analysis and optimal design of wind boosters for Vertical Axis Wind Turbines at low wind speed. *Journal of Wind Engineering and Industrial Aerodynamics* 159 (Korprasertsak2016), pp. 9–18.

[48] K. Kacprzak, G. Liskiewicz, and K. Sobczak. Numerical investigation of conventional and modified Savonius wind turbines. *Renewable energy* 60 (2013), pp. 578–585.

[49] J. Gao, H. Liu, J. Lee, Y. Zheng, M. Guala, and L. Shen. Large-eddy simulation and Co-Design strategy for a drag-type vertical axis hydrokinetic turbine in open channel flows. *Renewable Energy* 181 (2022), pp. 1305–1316.

[50] J. Lee, M. Musa, C. Feist, J. Gao, L. Shen, and M. Guala. Wake characteristics and power performance of a drag-driven in-bank vertical axis hydrokinetic turbine. *Energies* 12.19 (2019), p. 3611.

[51] I. Dobrev and F. Massouh. CFD and PIV investigation of unsteady flow through Savonius wind turbine. *Energy Procedia* 6 (2011), pp. 711–720.

[52] M. Elkhoury, T. Kiwata, K. Nagao, T. Kono, and F. ElHajj. Wind tunnel experiments and Delayed Detached Eddy Simulation of a three-bladed micro vertical axis wind turbine. *Renewable energy* 129 (2018), pp. 63–74.

[53] E. Antar and M. Elkhoury. Parametric sizing optimization process of a casing for a Savonius Vertical Axis Wind Turbine. *Renewable Energy* 136 (2019), pp. 127–138.

[54] T. Ogawa. Theoretical study on the flow about Savonius rotor (1984).

[55] Y. Ueda. Numerical analysis of flow-induced rotation of an S-shaped rotor. *Journal of Fluid Mechanics* 867 (2019), pp. 77–113.

[56] A. Alaimo, A. Esposito, A. Messineo, C. Orlando, and D. Tumino. 3D CFD analysis of a vertical axis wind turbine. *Energies* 8.4 (2015), pp. 3013–3033.

[57] A. Perez, O. Lopez, S. Poroseva, and J. Escobar. "Computational Study of a Small Rotor at Hover Using CFD and UVLM". In: *AIAA SciTech Forum*. 2019.

[58] K. M. Almohammadi, D. B. Ingham, L. Ma, and M. Pourkashanian. 2-D-CFD analysis of the effect of trailing edge shape on the performance of a straight-blade vertical axis wind turbine. *IEEE Transactions on Sustainable Energy* 6.1 (2014), pp. 228–235.

[59] J. Dong, A. Viré, C. S. Ferreira, Z. Li, and G. van Bussel. A Modified Free Wake Vortex Ring Method for Horizontal-Axis Wind Turbines. *Energies* 12.20 (Oct. 2019), p. 3900.

[60] G. S. Winckelmans. Vortex Methods. In: *Encyclopedia of Computational Mechanics*. John Wiley & Sons, Ltd, 2004. Chap. 5.

[61] G.-H. Cottet and P. D. Koumoutsakos. *Vortex Methods: Theory and Practice*. Cambridge University Press, 2000.

[62] J. Katz and A. Plotkin. *Low-Speed Aerodynamics*. 2nd ed. Cambridge Aerospace Series. Cambridge University Press, 2001.

[63] C. Ferreira. *The Near Wake of the VAWT: 2D and 3D Views of the VAWT Aerodynamics*. 2009.

[64] A. Zanon. "A vortex panel method for VAWT in dynamics stall". PhD thesis. May 2011.

[65] E. Dyachuk. "Aerodynamics of Vertical Axis Wind Turbines : Development of Simulation Tools and Experiments". PhD thesis. Uppsala University, Electricity, 2015, p. 86.

[66] S. Chegini, M. Asadbeigi, F. Ghafoorian, and M. Mehrpooya. An investigation into the self-starting of darrieus-savonius hybrid wind turbine and performance enhancement through innovative deflectors: A CFD approach. *Ocean Engineering* 287 (2023), p. 115910.

[67] Z. Pouransari and M. Behzad. Numerical investigation of the aerodynamic performance of a hybrid Darrieus-Savonius wind turbine. *Wind Engineering* (2023), p. 0309524X231188950.

[68] E. N. Irawan, S. Sitompul, K.-I. Yamashita, and G. Fujita. "Computational Fluid Dynamics Analysis on the Improvement of Hybrid Savonius-Darrieus NREL S809 at Various Fluid Flows". In: *2023 4th International Conference on High Voltage Engineering and Power Systems (ICHVEPS)*. 2023, pp. 389–394.

[69] S.-D. Fertahi, T. Bouhal, O. Rajad, T. Kousksou, A. Arid, T. E. Rhafiki, A. Jamil, and A. Benbassou. CFD performance enhancement of a low cut-in speed current Vertical Tidal Turbine through the nested hybridization of Savonius and Darrieus. *Energy Conversion and Management* 169 (2018), pp. 266–278.

[70] H. A. Madsen. "The Voith-Schneider Wind Turbine - Some Theoretical and Experimental Results". PhD thesis. Technical University of Denmark, Aug. 1980.

[71] G. Jin, L. Zou, Y. Jiang, Z. Zong, and Z. Sun. A circle theorem technique to handle 2-D flows around arbitrary cylinders in discrete vortex method. *Journal of Wind Engineering and Industrial Aerodynamics* 209 (2021), p. 104496.

[72] A. A. Mohammed, H. M. Ouakad, A. Z. Sahin, and H. M. S. Bahaidarah. Vertical Axis Wind Turbine Aerodynamics: Summary and Review of Momentum Models. *Journal of Energy Resources Technology* 141.5 (Feb. 2019), p. 050801.

[73] R. E. Froude. On the part played in propulsion by differences of fluid pressure. *Transactions of the Institution of Naval Architects* 30 (1889).

[74] H. A. Madsen. "The Actuator Cylinder - A Flow Model for Vertical Axis Wind Turbines". PhD thesis. Technical University of Denmark, Jan. 1982.

[75] G. H. Cottet. "Particle-grid domain decomposition methods for the Navier-Stokes equations in exterior domains". In: *Vortex Dynamics and Vortex Methods, American Mathematical Society*. 1991, pp. 103–117.

[76] J.-L. Guermond, S. Huberson, and W.-Z. Shen. Simulation of 2D External Viscous Flows by Means of a Domain Decomposition Method. *Journal of Computational Physics* 108.2 (1993), pp. 343–352.

[77] M. L. Ould-Salihi, G. H. Cottet, and M. El Hamraoui. Blending Finite-Difference and Vortex Methods for Incompressible Flow Computations. *SIAM Journal on Scientific Computing* 22.5 (2001), pp. 1655–1674.

[78] G. Daeninck. "Developments in hybrid approaches : Vortex method with known separation location". PhD thesis. Université catholique de Louvain, 2006.

[79] M. Stock, A. Gharakhani, and C. Stone. Modeling Rotor Wakes with a Hybrid OVERFLOW-Vortex Method on a GPU Cluster. In: *28th AIAA Applied Aerodynamics Conference*.

[80] M. Stock and A. Gharakhani. "A GPU-Accelerated Boundary Element Method and Vortex Particle Method". In: June 2010.

[81] A. Palha, L. Manickathan, C. S. Ferreira, and G. van Bussel. A hybrid Eulerian-Lagrangian flow solver (2015).

[82] P. Billuart, M. Duponcheel, G. Winckelmans, and P. Chatelain. A weak coupling between a near-wall Eulerian solver and a Vortex Particle-Mesh method for the efficient simulation of 2D external flows. *Journal of Computational Physics* 473 (2023), p. 111726.

[83] S. J. Huntley, D. P. Jones, and A. L. Gaitonde. Vortex Preservation Using Coupled Eulerian–Lagrangian Solver. *Journal of Aircraft* 56.2 (2019), pp. 457–468.

[84] C. Wales, D. Jones, and A. Gaitonde. Prescribed Velocity Method for Simulation of Aerofoil Gust Responses. *Journal of Aircraft* 52.1 (2015), pp. 64–76.

[85] S. J. Huntley, D. Jones, and A. Gaitonde. 2D and 3D gust response using a prescribed velocity method in viscous flows. In: *46th AIAA Fluid Dynamics Conference*. 2016.

[86] F. Moukalled, L. Mangani, and M. Darwish. *The Finite Volume Method in Computational Fluid Dynamics: An Advanced Introduction with OpenFOAM® and Matlab*. Springer International Publishing, 2016.

[87] B. Peerlings. "A review of aerodynamic flowmodels, solution methods andsolvers – and their applicability toaircraft conceptual design". MA thesis. Delft University of Technology, 2018.

[88] C. M. P. da Silva Santos. "A Lagrangian-Eulerian method for fully non-linear wave simulations using hierarchicalcartesian grids with multigrid acceleration". PhD thesis. University of Bath, 2003.

[89] R. Pasolari, C. Ferreira, and A. van Zuijlen. Coupling of OpenFOAM with a Lagrangian vortex particle method for external aerodynamic simulations. *Physics of Fluids* 35.10 (2023).

[90] N. Franchina, G. Persico, and M. Savini. 2D-3D computations of a vertical axis wind turbine flow field: Modeling issues and physical interpretations. *Renewable Energy* 136 (2019), pp. 1170–1189.

[91] L. Chao, Z. Sonye, X. You-Lin, and X. Yiqing. 2.5 D large eddy simulation of vertical axis wind turbine in consideration of high angle of attack. *Renew. Energy* 51 (2013), pp. 317–330.

[92] H. Fatahian, Z. Mohamed-Kassim, and W. S. Chang. Insights into the flow dynamics and rotor performance of a Savonius turbine with dynamic venting using controllable flaps. *Physics of Fluids* 34.12 (2022).

[93] N. Alom and U. K. Saha. Examining the aerodynamic drag and lift characteristics of a newly developed elliptical-bladed Savonius rotor. *Journal of Energy Resources Technology* 141.5 (2019), p. 051201.

[94] F. Li, J. Yao, C. Eskilsson, Y. Pan, J. Chen, and R. Ji. Investigations on the wave performance of Savonius turbine operating under initial phase-locked strategy. *Physics of Fluids* 35.9 (2023).

[95] C. Vigneswaran and G. VishnuKumar. Computational analysis of influence of CFJ components on aerodynamic performance. *Physics of Fluids* 35.9 (2023).

II

EULERIAN METHOD

2

PERFORMANCE ANALYSIS OF AN IDEALIZED HYBRID VAWT

Parts of this chapter have been published in Wind Energy*.

The previous studies have shown that the configuration of hybrid VAWTs benefits from the improvement in start-up performance. However, it is unknown whether the optimization of Darrieus blades and/or Savonius blades would contribute to the power increase of the hybrid VAWT compared to a single Darrieus. This chapter aims to address the first research question regarding the implications for the study of hybrid VAWT configuration. To achieve this, we simplify the hybrid rotor into its more fundamental formulation as a hybrid force field. To investigate the effect of force distributions of the Savonius/Darrieus part on the power performance of the Darrieus-Savonius combined vertical axis wind turbine (hybrid VAWT), the hybrid VAWT is modeled as uniform force fields with different magnitudes and locations. The goal of idealization is to simplify the intricate interactions between the Savonius and Darrieus components. The conventional momentum theory cannot model flow diffusion due to a lack of viscous effects. Hence, to understand the flow physics around the hybrid VAWT, the inner Savonius and outer Darrieus rotors are modeled by the actuator disk and cylinder in OpenFOAM, respectively. The performance of hybrid VAWT configurations is discussed.

*Jingna Pan, Carlos Ferreira, Alexander van Zuijlen, Performance analysis of an idealized Darrieus-Savonius combined wind turbine, Wind Energy, 1-16 (2024) [1].

2.1. INTRODUCTION

Flow models are required to investigate the performance and complex aerodynamics of hybrid VAWTs [2, 3]. In Chapter 1 we reviewed some of the research in the development and application of these models. However, the benefits and performance trade-offs of the hybrid VAWT configuration have not been clarified yet.

2

In this chapter, a 2D idealized hybrid VAWT, comprising a Darrieus part and a Savonius part, is investigated. To estimate the power performance of the hybrid VAWT, an idealized hybrid VAWT is implemented using the Eulerian RANS model as momentum sources. The Darrieus part is represented by a uniformly-loaded actuator cylinder, while the Savonius part is represented by a uniformly-loaded actuator disk. This approach allows us to examine the power gain or loss of the hybrid VAWT in an ideal simulation, considering variations in the location and force distribution on the actuators. It is worth noting that the maximum power coefficient $c_{p_{\text{ideal}}}$ of 0.616 can be achieved with uniform force distributions along the actuator cylinder [4]. This value exceeds the maximum c_p of the actuator disk. Our study primarily relies on numerical simulations to investigate the effect of force distribution on power output of the idealized hybrid VAWT. Section 2.2 describes the theoretical and numerical models of the actuator disk and actuator cylinder. In Section 2.3, different force distributions of hybrid turbines are investigated based on the extracted power and velocity fields. Finally, Section 2.4 summarizes our findings.

2.2. METHODOLOGY

This section discusses the similarities and differences between theoretical and numerical actuator models. An idealized hybrid VAWT in the numerical model is represented by two actuator surfaces: a circular surface for the Darrieus part and a thin rectangular surface for the Savonius part. The blade forces act on the flow as distributed body forces along the actuator surfaces. First, the relation between vorticity and force is derived. The theoretical models of the actuator disk and actuator cylinder are also presented. Subsequently, the Eulerian RANS model simulating the idealized hybrid VAWT with uniform loading is proposed.

2.2.1. SIMPLIFICATION OF VORTICITY EVOLUTION

Given the assumption of a 2D incompressible and inviscid flow around the idealized hybrid VAWT, the vorticity equation is expressed as Equation 2.1 without vorticity turning, stretching and diffusion [5, 6]. The term $\frac{\mathrm{D}\vec{\omega}}{\mathrm{D}t}$ on the left-hand side denotes the material derivative of the vorticity vector $\vec{\omega}$. It is the rate of change of vorticity of the moving fluid particle. This equation indicates that vorticity can only be introduced by a change of external body forces $\vec{f}$. The force distribution of a 2D actuator with uniform loading is represented by Equation 2.2, where f_x and f_y denote body forces in the x and y directions. In the case of actuator disk, f_y is equal to zero.

$$\frac{\mathrm{D}\vec{\omega}}{\mathrm{D}t} = \nabla \times \vec{f} \tag{2.1}$$

$$\vec{f} = [f_x \quad f_y \quad 0]^T \tag{2.2}$$

Substitution of Equation 2.2 into Equation 2.1 leads to:

$$\frac{\mathrm{D}\vec{\omega}}{\mathrm{D}t} = \begin{bmatrix} 0 \\ 0 \\ \frac{\partial f_y}{\partial x} - \frac{\partial f_x}{\partial y} \end{bmatrix} \tag{2.3}$$

Hence, the shedding vorticity only appears when $\frac{\partial f_y}{\partial x} - \frac{\partial f_x}{\partial y}$ is non-zero. As the actuator models characterize the flow as vortices by the change of the force distribution, the vorticity fields of the theoretical actuator disk and actuator cylinder models will be investigated in Section 2.3.1. The force discontinuity is used to represent the hybrid VAWT model in this study. This assumption potentially ignores the effect of blade shape on the performance of the hybrid VAWT.

2.2.2. THEORETICAL ACTUATOR MODEL

A brief introduction of the existing theoretical actuator models is presented, emphasizing the specific implementations used in this study. Extensive references are suggested for more detailed information about the overview of the actuator disk model [7, 8, 9, 10] and actuator cylinder model [11, 12, 13]. This work investigates the case of an idealized turbine with uniform force distribution, where the viscosity is neglected. The heat transfer is also not included in this study. So, the flow problem is simplified as a 2D steady inviscid incompressible flow with constant internal energy.

The actuator disk model is illustrated in Figure 2.1a. In this model, the flow problem is assumed to be solved along the axial axis. The relation between the velocity at the disk U_R and the freestream upwind velocity U_∞ is expressed through an induction factor a, shown in Equation 2.4. The induction factor a is obtained by equating expressions of streamtube dynamics, representing the change in wind speed normalized by U_∞.

$$U_R = U_\infty(1-a) \tag{2.4}$$

The thrust and power coefficients are calculated as $c_T = 4a(1-a)$ and $c_p = 4a(1-a)^2$ according to the momentum theory. The relation of power coefficient c_p and thrust coefficient c_T is theoretically expressed as $c_p = c_T(0.5 + 0.5\sqrt{1-c_T})$. The maximum power that can be extracted by a wind turbine is known as the Betz limit and corresponds to $c_{p_{Betz}} = 16/27$, $c_{T_{Betz}} = 8/9$ and $a = 1/3$ [14, 15, 16].

The actuator cylinder model is a 2D dynamic model extending the application of the actuator disk model, except that the actuator cylinder model is used in two directions rather than only one axial direction. A schematic of the actuator cylinder for VAWT is shown in Figure 2.1b, where the body forces in the normal direction are denoted as Q_n.

Given the same thrust coefficient, the distribution of the volumetric force along the actuator is implemented differently for the two models. For the actuator disk, the volumetric force is evenly added to each cell of the actuator in the x direction according to the

given thrust. In the case of the actuator cylinder, the force components in the normal direction Q_n are evenly distributed along the actuator. It is calculated from $Q_n = \frac{T}{\sum_{i=0}^{n} (\vec{e}_{n_i} \cdot \vec{e}_{x_i})}$, where $\vec{e}_{n_i}$ and $\vec{e}_{x_i}$ are the unit vectors in the normal and x-axis directions, respectively. The denominator $\sum_{i=0}^{n} (\vec{e}_{n_i} \cdot \vec{e}_{x_i})$ is the sum of the normal vectors' projection on the x axis, n is the number of cells that fall into the actuator region. The current work focuses on a 2D idealized hybrid VAWT, which can be represented by placing an actuator disk inside an actuator cylinder. The schematic of the idealized hybrid VAWT is depicted in Figure 2.1c. It is worth noting that the $c_{T_{AD}}$, $c_{T_{AC}}$ and $c_{T_{hybrid}}$ represent thrust coefficients of the AD, AC and idealized hybrid VAWT, which are nondimensionalized by their respective radii (R_{AD}, R_{AC}, $R_{hybrid} = R_{AC}$). The thrust coefficient of the idealized hybrid VAWT corresponds to the outer radius, given by $c_{T_{hybrid}} = c_{T_{AC}} + c_{T_{AD}} \cdot \frac{R_{AD}}{R_{AC}}$.

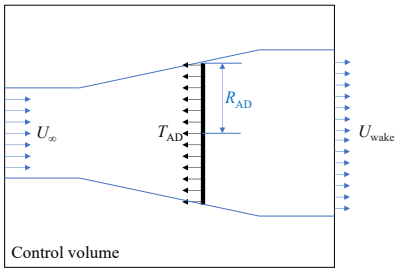

(a) Actuator disk

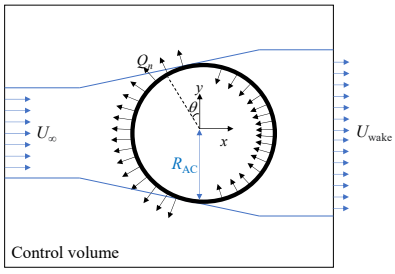

(b) Actuator cylinder

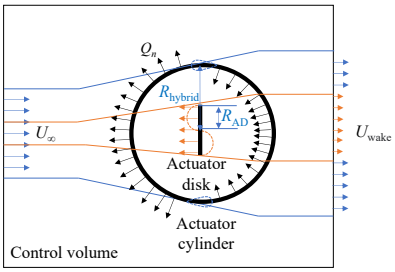

(c) Idealized hybrid VAWT

Figure 2.1: Schematic of actuator models for the idealized turbine

Given the uniform force distribution along different actuator surfaces, the vorticity shedding depends on the gradient of body forces according to the vorticity equation in Section 2.2.1. So, the idealized hybrid VAWT in Figure 2.1c can be superimposed to one single actuator as shown in Figure 2.2. The force distribution becomes non-uniform with the superimposed force T_{AD} in the center and the original force T_{AC}.

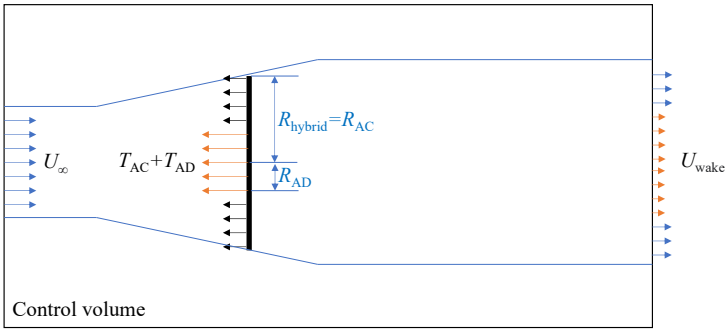

Figure 2.2: Schematic of actuator disk model with non-uniform force distribution

2.2.3. NUMERICAL ACTUATOR MODEL

SET-UP

The force distribution is prescribed as uniform along the disk or cylinder with a thickness of 3.38% of the cylinder dimension. This ensures the actuator cylinder is aligned with the cylindrical mesh shown in Figure 2.3b. In this work, the 2D flow fields of the actuator disk, actuator cylinder, and idealized hybrid VAWT are simulated in OpenFOAM 4.1 [17]. The steady laminar solver simpleFoam is employed with a Reynolds number of 9.67e5. The computational domain and mesh are shown in Figure 2.3. The domain size is $50R_{AC}$

in the x direction and $30R_{AC}$ in the y direction. The numerical power output for cell i can be obtained from $\vec{F}_i \cdot V_i \cdot \vec{u}_i$, where $\vec{F}_i$ is volume force with a unit of N/m^3, V_i is the volume of cell i, and $\vec{u}_i$ is the local velocity at cells where forces are exerted.

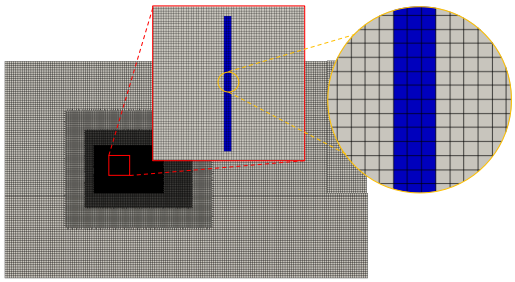

(a) Actuator disk

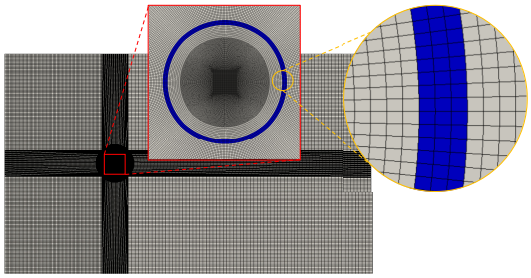

(b) Actuator cylinder

Figure 2.3: Computational domain and mesh in Eulerian RANS simulations

Table 2.1: Mesh independence for AC and idealized hybrid VAWT with upwind AD

Cell number	7.6e4	8.1e4	8.8e4	1.0e5	1.8e5
AC	0.59544 (+0.48%)	0.59581 (+0.54%)	0.59614 (+0.60%)	0.59545 (+0.48%)	0.59559 (+0.51%)
Hybrid VAWT	0.57740	0.57670	0.57694	0.57603	0.57563

Mesh independence for the single AC ($c_{T_{AC}} = 0.93$) and hybrid VAWT with upwind AD

($c_{T_{AC}} = 0.89$, $c_{T_{AD}} = 0.09$) is shown in Table 2.1. The power coefficient is obtained from simulations with different cell numbers. Three configurations for actuator thickness are studied for the single AC with $c_{T_{AC}} = 0.85$. The thickness of $3.38\%D_{AC}$, $5.07\%D_{AC}$ and $6.76\%D_{AC}$ are applied to the AC with body force exerted into three, four, and six layers of cells, respectively. The purpose of this analysis is to determine the mesh configuration and actuator thickness required for accurate results while considering the computational cost. The power coefficient c_p obtained from the three configurations of thickness is predicted as 0.58530, 0.63049, and 0.65858, with discrepancies of −0.73%, +6.93% and +11.70% compared to the theoretical results. So, the thickness of $3.38\%D_{AC}$ with three layers for AC yields a better prediction than the other two thickness configurations. The five mesh configurations predict discrepancies of +0.48%, +0.54%, +0.60%, +0.48% and +0.51% compared to $c_{p_{Betz}}$.It is observed that a cell number of 8.8e4 is chosen to balance computational cost and accuracy for both the single actuator and hybrid actuator cases. Compared to the refined mesh cases, the numerical discrepancies are found to be 0.092% for the single actuator simulation and 0.23% for the hybrid actuator simulation. These errors indicate the deviation of the results obtained with the chosen cell number from the more refined solutions.

DIFFERENCES BETWEEN THEORETICAL AND NUMERICAL METHODS

In OpenFOAM, the Navier-Stokes (NS) equation [18] for incompressible flow considering the force field of the actuator is shown in Equation 2.5, where the diffusion term is included. However, the theoretical methods ignore this term.

$$\frac{\partial \vec{u}}{\partial t} + (\vec{u} \cdot \nabla)\vec{u} = -\frac{\nabla p}{\rho} + \upsilon \nabla^2 \vec{u} + \frac{\vec{F}}{\rho} \tag{2.5}$$

There are additional differences that need to be accounted for when comparing the theoretical actuator models to the numerical simulations:

- Thickness of the actuator surface: In theoretical actuator models, the actuator surface is assumed to have zero thickness. However, in numerical simulations using Eulerian RANS, the actuator surface is represented by a finite thickness. This means that the body force applied to the flow should be distributed over the cell volumes in the computational domain rather than being concentrated on an infinitesimally thin surface.
- Force distribution at the tip: The theoretical actuator models may assume a discontinuity in the force distribution at the tip of the actuator surface. However, in numerical simulations, due to the finite thickness of the actuator surface, the point where the force discontinuity occurs may not align exactly with the theoretical location. The numerical method may introduce some deviations in the force distribution near the actuator tip.

2.3. RESULTS AND DISCUSSIONS

2.3.1. COMPARISON OF STAND-ALONE ACTUATOR MODELS

The vorticity equation shown in Section 2.2.1 demonstrates that the shedding vorticity is characterized by force changes. To validate our numerical model, the actuator cylinder

is categorized into three types of surface: circular surface, upwind-half circular surface, and downwind-half circular surface. The uniform force distributions of different actuators are depicted in Figure 2.4. The thrust coefficient $c_T = 0.93$ is applied for the four actuators. The total thrust of the rotor T needs to be calculated and distributed along the actuator to implement the actuator disk and actuator cylinder model in Eulerian RANS simulations.

The corresponding vorticity fields are shown in Figure 2.5. The vorticity originates from the top and bottom ends of an actuator, where the force discontinuity occurs. The expanded vorticity shedding is observed in four actuators. The similar vorticity distributions among the actuators indicate comparable flow mechanisms, emphasizing the role of force distribution changes in introducing vorticity described in Section 2.2.1. The power coefficients obtained from AD, AC, upwind AC, and downwind AC are 0.59115, 0.59614, 0.59566, and 0.59598, respectively. The visualizations of the four configurations provide valuable insights into flow patterns and contribute to optimizing the design and performance of the idealized hybrid VAWT.

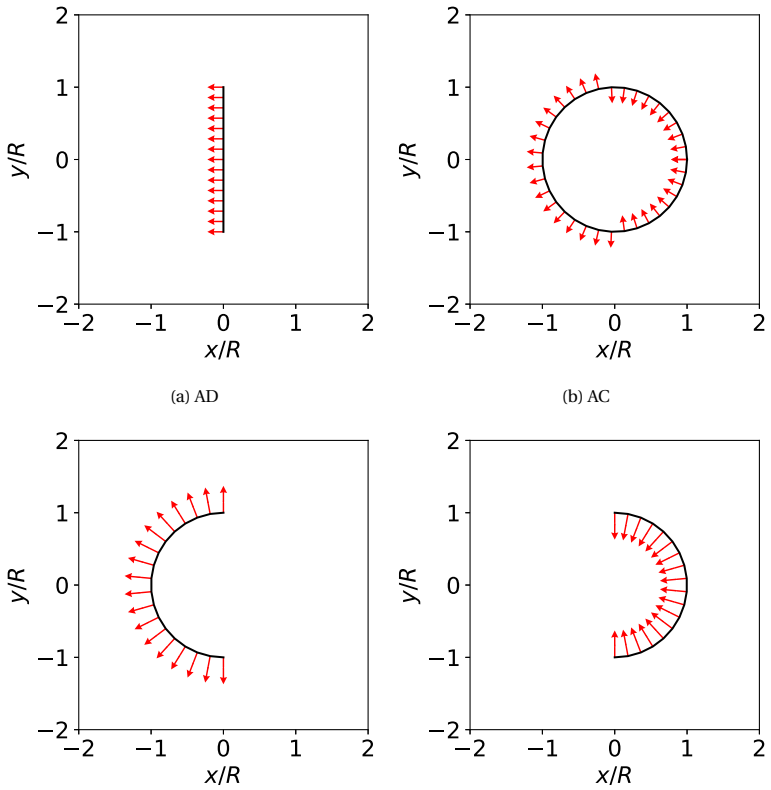

(a) AD

(b) AC

(c) Upwind AC

(d) Downwind AC

Figure 2.4: Force distribution of different actuators (Red arrows represent vectors of body force)

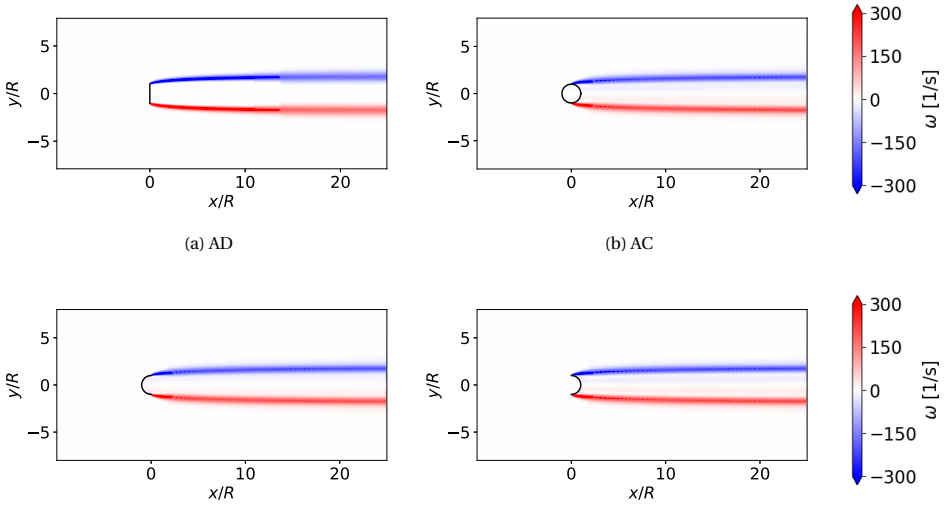

(a) AD (b) AC

(c) Upwind AC (d) Downwind AC

Figure 2.5: Vorticity fields of different actuators

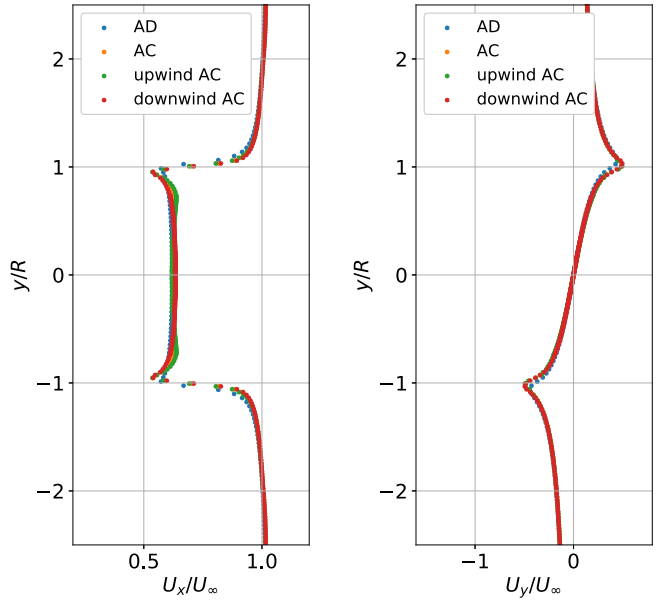

(a) Streamwise flow (b) Crosswise flow

Figure 2.6: Non-dimensional flow velocity at $x = 0$

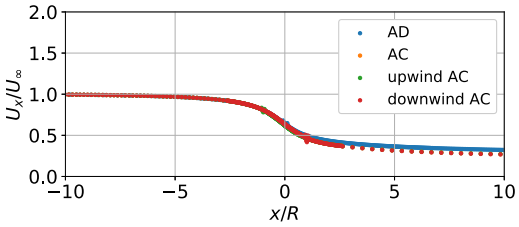

(a) Streamwise flow velocity

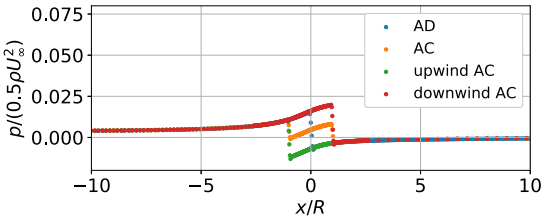

(b) Pressure

Figure 2.7: Non-dimensional streamwise velocity and pressure distribution at $y = 0$

The Non-dimensional flow velocity at the center of an actuator ($x = 0$) is depicted in Figure 2.6. The streamwise velocity shows a gradual decrease instead of a sudden drop at $y/R = \pm 1$. The sampled flow velocity variations at the center of the four actuators have a similar trend in each direction (streamwise and crosswise directions) with negligible differences. The magnitude of minimum $U_{x,x=0}$ for the AD case is around 5.97% higher than the other three AC cases. And the magnitude of minimum and maximum $U_{y,x=0}$ for the AD case exhibits around 9.90% of differences compared to those for the other three AC cases. These negligible differences are attributed to the effect of volume force exerted into a finite thickness of cells in Figure 2.3. The above quantitative and qualitative comparisons demonstrate that the proposed numerical models can predict identical vorticity systems with the same thrust coefficient for the uniformly loaded actuator.

The non-dimensional streamwise velocity and pressure distribution along the x-axis are depicted in Figure 2.7. It is observed that the pressure decreases at $x/R = 0$ for AD, $x/R = \pm 1$ for AC, $x/R = -1$ for upwind AC, and $x/R = 1$ for downwind AC. The streamwise velocity gradually decreases along the x-axis for the four actuators. The pressure reductions for the four actuators have the same amplitudes. The modeling of pressure drop occurs at the position where the body forces are exerted, yielding an effective numerical method.

The numerical model is further verified against the theoretical model in a range of thrust coefficients (0.171 to 1.026). A series of thrust coefficients are chosen to capture the trend of the power coefficient variation. Comparison between theoretical and numerical results of the variation of power coefficient c_p for an actuator cylinder with different thrust coefficients c_T is shown in Figure 2.8. It is observed that the numerical and theoretical results yield similar trends with $c_T = 0.0 \sim 0.5$. Between c_T =0.5 and 0.89, the numerical c_p is lower than the theoretical prediction. For $c_T > 0.89$, OpenFOAM tends

to overestimate the c_p. The maximum power coefficient $c_{p_{max}}$ is about 0.598% higher than the theoretical $c_{p_{max}}$. This difference is negligible, and it is expected due to the wake expansion (Figure 2.5) and the gradual velocity decrease at $y/R = \pm 1$ (Figure 2.6) predicted by the numerical model. The validity of this assumption has also been demonstrated by De Tavernier [6]. The vorticity fields, velocity, and pressure variations of the four actuators are identical with equivalent body force distributions. This equivalence demonstrates the validity of the proposed numerical model.

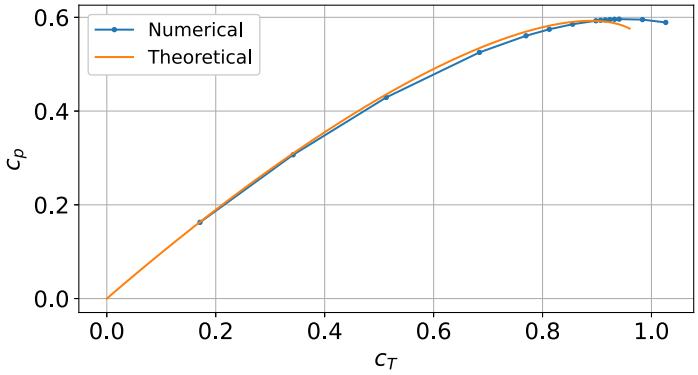

Figure 2.8: Variation of power coefficient for AC with different c_T in theoretical and numerical solution

2.3.2. EFFECT OF FORCE DISTRIBUTION ON POWER PERFORMANCE OF HYBRID VAWT

VARIED POSITION OF IDEALIZED SAVONIUS, REPRESENTING AD

To estimate the power of an idealized hybrid VAWT, the inner Savonius is represented by a uniformly loaded actuator disk, while the Darrieus rotor is idealized as a uniformly loaded actuator cylinder. The vorticity shedding depends on the force variation of the actuator. So, force distribution is the most relevant factor that affects the power performance of hybrid VAWT. Researchers have been putting efforts into implementing active pitch control to control blade forces so that a better power production is achieved from VAWTs. Bouzaher et al. [19] proposed a dynamic control device (a couple of flapping wings) for VAWT blades to get the optimum power harvesting. The control scheme reduces the negative effects of blade-vortex interaction on power production. They attempted to resolve the correlation between force distribution and power performance for the hybrid VAWT. Their study revealed that the total power of the hybrid VAWT varies with different rotor configurations. It indicates that the interaction between each component of hybrid VAWT is the main cause of power change. So, the position of the inner Savonius is varied to explore the optimal force distribution of the hybrid VAWT.

In this section, the impact of the inner AD's position in an idealized hybrid VAWT is investigated. By varying the position of the inner AD, we aim to understand its influence on the overall performance of the idealized hybrid VAWT. Given the assumption of two actuators mounted on the same rotational axis, the radius ratio of the outer and inner actuators is set as five. It is known that the power output of the realistic hybrid VAWT

is affected by the presence of inner Savonius. The power reduction of a hybrid VAWT occurs mainly at the upwind and downwind region [20]. To understand the power generation mechanism of the hybrid VAWT, the upwind and downwind of the hybrid VAWT could be the most related region. The inner AD acting as a turbine- or a propeller- mode is placed upwind, center, or downwind of the cylinder generating six kinds of force distributions. The force distributions for an idealized hybrid VAWT are depicted in Figures 2.9 and 2.10 with the same AC forces and different AD forces. The force directions of the inner AD are the same with the direction of x-axis in the turbine-mode case and opposite to the direction of x-axis in the propeller-mode case.

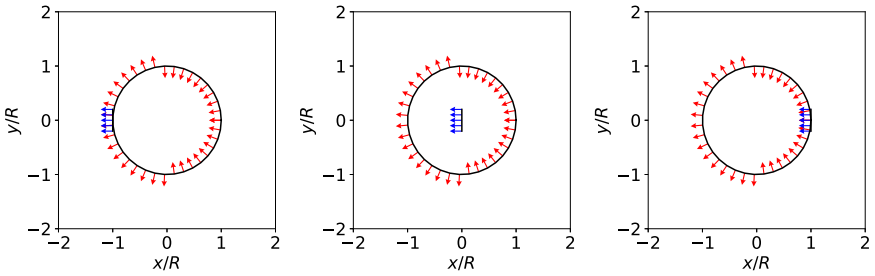

(a) Upwind AD (b) Center AD (c) Downwind AD

Figure 2.9: Force distribution for an idealized hybrid VAWT with a turbine-mode AD (force of AD is opposite to the inflow direction, $c_{T_{AD}} > 0$)

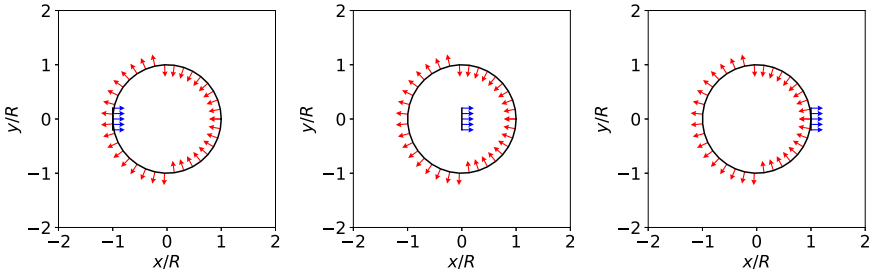

(a) Upwind AD (b) Center AD (c) Downwind AD

Figure 2.10: Force distribution for an idealized hybrid VAWT with a propeller-mode AD (force of AD is directed to the inflow direction, $c_{T_{AD}} < 0$)

As the maximum power coefficient of the actuator disk theory is achieved when $c_T = 0.89$, the thrust coefficient for the outer actuator of the idealized hybrid VAWT is fixed as 0.89. The thrust coefficient for the inner actuator varies to investigate its impact on the overall power performance. Power coefficient of the aforementioned idealized hybrid VAWTs with varied $c_{T_{AD}}$ and $c_{T_{AC}} = 0.89$ is depicted in Figure 2.11. The x-axis is the thrust coefficient of the idealized hybrid VAWT $c_{T_{hybrid}}$, and the y-axis is the power coefficient of the idealized hybrid VAWT $c_{p_{hybrid}}/c_{p_{Betz}}$ normalized by the optimal theoretical

power coefficient of the single AC $c_{p_{Betz}}$. The results indicate that the power coefficient of idealized hybrid VAWT barely exceeds $c_{p_{Betz}}$, except when the low-thrust AD operates in a propeller mode. The idealized hybrid VAWT with a center turbine-mode AD has a higher power coefficient compared to idealized hybrid VAWT with upwind and downwind turbine-mode ADs. The maximum power extracted from idealized hybrid VAWT with upwind AD and given $c_{T_{AC}} = 0.89$ is around 0.435% higher compared to $c_{p_{Betz}}$. The negligible difference can be attributed to the modeling difference between the theoretical and numerical methods (Section 2.2.3). The hybrid VAWT cannot show a significant power increase compared to an optimal single Darrieus.

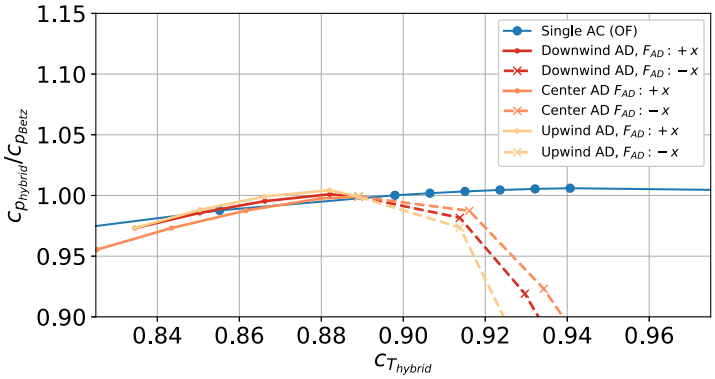

Figure 2.11: Power coefficient of an idealized hybrid VAWT $c_{p_{hybrid}}/c_{p_{Betz}}$ with varied $c_{T_{AD}}$, $c_{T_{AC}} = 0.89$

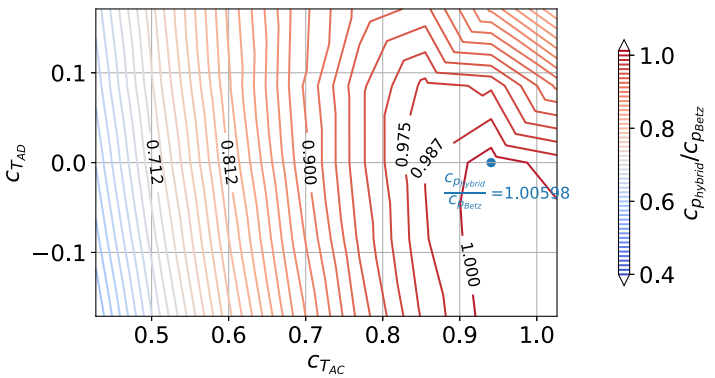

Figure 2.12: Power coefficient of an idealized hybrid VAWT $c_{p_{hybrid}}/c_{p_{Betz}}$ with downwind AD for different combinations of $c_{T_{AD}}$ and $c_{T_{AC}}$.

The contour of the power coefficient for different combinations of $c_{T_{AD}}$ and $c_{T_{AC}}$ is illustrated in Figure 2.12. The power coefficient between the idealized hybrid VAWT and single AC with the optimal thrust coefficient $c_{T_{Betz}}$ is compared. It is observed that $c_{p_{hybrid}}/c_{p_{Betz}}$ exceeds one at the right bottom of the figure where the inner disk oper-

ates as a propeller and the outer cylinder operates at near-optimal conditions. So, the power coefficient of the idealized hybrid VAWT exceeds $c_{p_{Betz}}$ when the inner AD operates in a propeller mode. The blue point is the power coefficient of the optimal single AC, showing the overestimation of our numerical model. This contour suggests that the propeller mode of the AD force contributes to the power compensation in the idealized hybrid VAWT configuration.

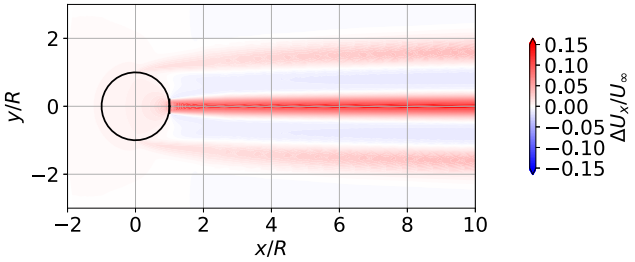

(a) $c_{T_{AD}} < 0$ (propeller mode)

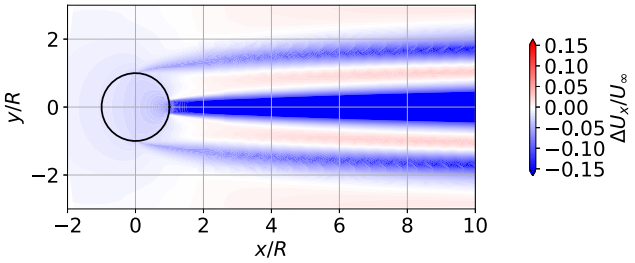

(b) $c_{T_{AD}} > 0$ (turbine mode)

Figure 2.13: Difference of non-dimensional axial velocity field between an idealized hybrid VAWT with downwind AD and the single AC, $c_{T_{AC}} = 0.93$, $c_{T_{AD}} = \pm 0.1$

To determine the reason behind the power increase for the idealized hybrid VAWT with AD in a propeller mode, the power coefficient of the idealized hybrid VAWT with turbine-mode/propeller-mode downwind AD and their velocity field are studied. The difference between the non-dimensional axial velocity of an idealized hybrid VAWT with a downwind AD and the single AC ΔU_x in the flow field is depicted in Figure 2.13. This is to explore the effect of force distribution on flow fields of the idealized hybrid VAWT. In the case of an idealized hybrid VAWT with a turbine-mode AD shown in Figure 2.13b, the high energy extraction on the upwind side of the rotor leads to a deficit in kinetic energy, reducing the energy extraction on the downwind side. However, when the AD operates in a propeller mode, as shown in Figure 2.13a, it helps to mitigate the rotor blockage caused by this kinetic energy deficit and to generate a slighter wake expansion

downstream. As claimed in Sections 2.2.1 and 2.2.2, the vorticity development depends on the force distribution of the actuator. The total force of the outer cylinder and inner disk (Figure 2.1c) is consistent with the force of a single disk (Figure 2.2). This indicates adjusting the force distribution of AC would be the alternative to moving the inner AD. Similar studies have been conducted by Huang [21], where the force distribution was changed by pitch control of blades. In Section 2.3.2, we will further study the effect of force distribution on the power output of the idealized hybrid VAWT.

To further comprehend the operational conditions of the idealized hybrid VAWT, its power performance with specific $c_{T_{AC}}$ and $c_{T_{AD}}$ is compared to the corresponding theoretical AC with the same $c_{T_{AC}}$. The power performance of the hybrid VAWT with center AD is taken as an example to compare with the single AC with the same $c_{T_{AC}}$ (Figure 2.11). The results of the power coefficient for the idealized hybrid VAWT are shown in Figure 2.14. The legend $c_{p_{hybrid}}/c_{p_{AC,theoretical}}$ represents the ratio of the power coefficient of the idealized hybrid VAWT with specific $c_{T_{AC}}$ over that of the single theoretical AC with the same $c_{T_{AC}}$. The results on the top-right of the figure are not presented due to the numerical instabilities of the high-thrust cases. Besides, the flow reversal behind actuators leads to significant unsteadiness in the predicted power. When a turbine-mode AD ($c_{T_{AD}} > 0$) is employed, the value of $c_{T_{AC}}$ should be lower to maintain or even increase c_p of the idealized hybrid VAWT compared to c_p of the AC with the same $c_{T_{AC}}$. On the other hand, when a propeller-mode AD ($c_{T_{AD}} < 0$) is employed, the AC is expected to operate with a high c_T to maintain the same amount of c_p, thus compensating for the power consumption of propeller-mode AD. This analysis highlights the importance of selecting the appropriate operating mode and adjusting the thrust coefficients for the actuators in the idealized hybrid VAWT to optimize its power performance.

The optimal operational points for the idealized hybrid VAWT are analyzed based on predefined force conditions. When a specific $c_{T_{AC}}$ is given, there is an optimal operational point for the inner disk to obtain the maximum c_p of the idealized hybrid VAWT. These optimal points, obtained from both numerical and theoretical solutions, are plotted in the Figure 2.14. The results show that the optimal configurations of the idealized hybrid VAWT with a known $c_{T_{AC}}$ occur when $c_{T_{AC}} + c_{T_{AD}}$ is equal to 0.89. The theoretical results agree well with the numerical results.

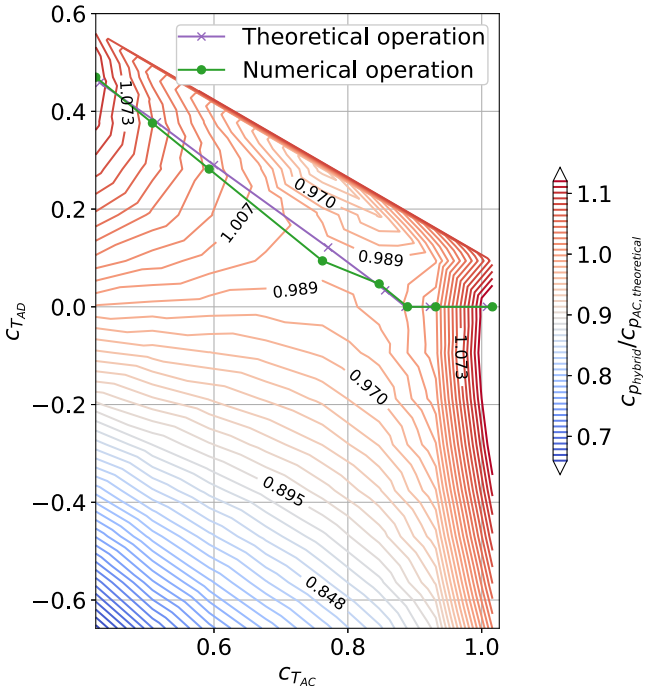

Figure 2.14: Power coefficient of an idealized hybrid VAWT with center AD $c_{p_{hybrid}}/c_{p_{AC,theoretical}}$ for different combinations of $c_{T_{AD}}$ and $c_{T_{AC}}$

To give further information for the design of the idealized hybrid VAWT, the operational conditions are compared under different given forces. The relation between $c_{p_{hybrid}}/c_{p_{Betz}}$ and $c_{T_{AD}}$ for an idealized hybrid VAWT with the center AD is shown in Figure 2.15. For given high-thrust cases $c_{T_{AC}} \geq 0.85$, the power coefficient of the idealized hybrid VAWT decreases with the increasing $c_{T_{AD}}$. While for low-thrust cases where $c_{T_{AC}} \leq 0.76$, the idealized hybrid VAWT exhibits a slight power increase when $c_{T_{AD}}$ reaches a certain value. So, given a low $c_{T_{AC}} \leq 0.76$ for the idealized hybrid VAWT, we should increase the thrust coefficient of the inner AD to get the maximum power. But given a high $c_{T_{AC}} \geq 0.85$, the power performance of the idealized hybrid VAWT will only be worse with the presence of the inner AD.

The relation between $c_{p_{hybrid}}/c_{p_{Betz}}$ and $c_{T_{AC}}$ for an idealized hybrid VAWT with the center AD is shown in Figure 2.16. The case of $c_{T_{AD}} = 0.00$ represents the power coefficient of the single AC. It can be observed that the maximum power coefficient of the idealized hybrid VAWT decreases with the increasing $c_{T_{AD}}$. To achieve the power of the hybrid VAWT as $c_{p_{hybrid}}/c_{p_{Betz}} = 0.7$, the thrust of AC is supposed to increase with the decreasing given $c_{T_{AD}}$. In other words, given a low $c_{T_{AD}}$ requires higher $c_{T_{AC}}$ to gain the same amount of power as the given high $c_{T_{AD}}$.

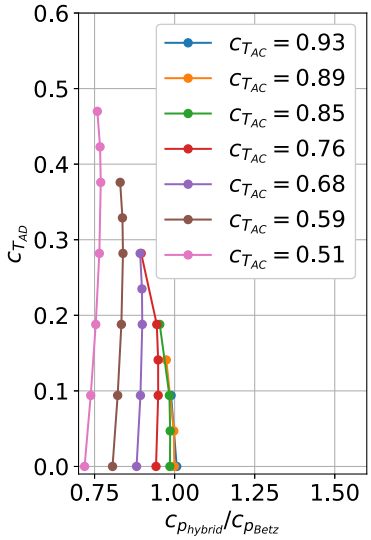

Figure 2.15: $c_{p_{hybrid}}/c_{p_{Betz}}$ vs $c_{T_{AD}}$ for an idealized hybrid VAWT with center AD

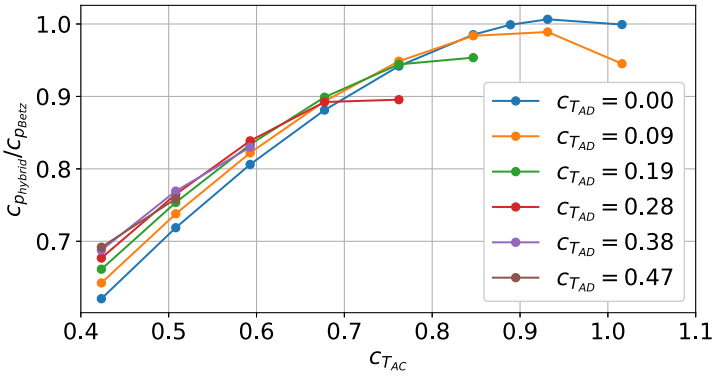

Figure 2.16: $c_{p_{hybrid}}/c_{p_{Betz}}$ vs $c_{T_{AC}}$ for an idealized hybrid VAWT with center AD

ADJUSTED FORCE DISTRIBUTION ON IDEALIZED DARRIEUS, REPRESENTING AC

As analyzed in Section 2.3.2, the hybrid VAWT with a propeller-mode AD has a comparable power coefficient with a single Darrieus. It indicates that the propeller-mode AD effectively counteracts the non-optimal force distribution of hybrid VAWT. Taking an example of an idealized hybrid VAWT with outer AC (representing the non-uniformly loaded Darrieus) and a center AD (representing the uniformly loaded Savonius), the effect of the adjusted force distribution on the performance of the idealized hybrid VAWT is investigated. The angle ψ is proposed, referring to the range of adjusted force distribution for the outer AC. It is the angle between the x-axis and the starting point of the

adjusted region on AC, as shown in Figure 2.17. In this study, the thrust coefficient of the inner AD is set as 0.1, and the outer AC has a non-uniform force distribution. The adjusted force distribution on the outer AC is non-uniform because of the superimposition of the force for propeller-mode AD and the force for AC operating at the optimal condition, shown in Figure 2.10a.

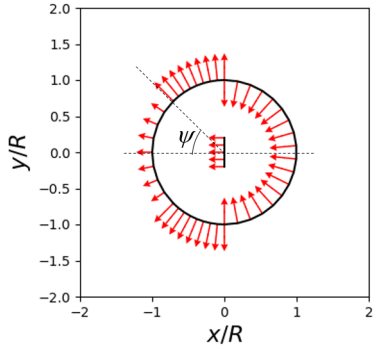

Figure 2.17: A hybrid VAWT with adjusted force distribution

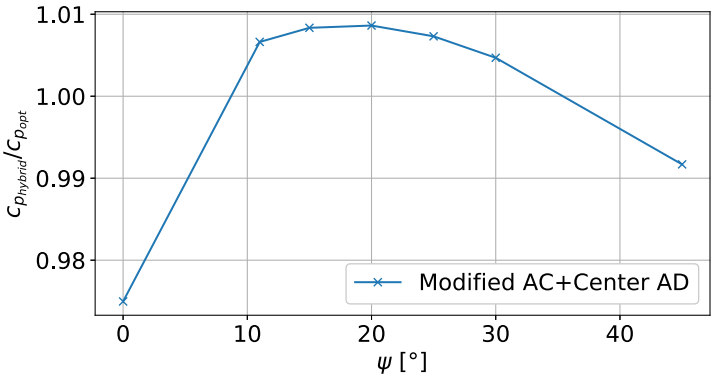

Figure 2.18: Power coefficient $c_p/c_{p_{opt}}$ of a hybrid VAWT with and without adjusted force distribution ($c_{T_{AD}} = 0.1$, $c_{T_{adjusted}} = -0.1$)

The power coefficients of a hybrid VAWT with and without adjusted force distribution on the outer AC are depicted in Figure 2.18. $\psi = 0°$ represents a hybrid VAWT with uniformly loaded AC and AD, shown in Figure 2.9b. And non-zero ψ represents a hybrid VAWT with adjusted force distribution on the outer AC, shown in Figure 2.17. The power coefficient of the hybrid VAWT is normalized by the numerical maximum power coefficient of the single AC $c_{p_{opt}}$. It is observed that the power coefficient increases and then decreases with the increase of angle ψ. The optimal ψ is around 20°, in which case the power coefficient is 3.5% higher than the hybrid VAWT with uniformly loaded AC and

AD. This indicates that power compensation occurs by adjusting force distribution in the outer AC. Among the studied cases of adjusted hybrid VAWT with varying ψ, angles ranging from 8.25° to 34° provide the optimal force distribution of the hybrid VAWT with no power losses. The adjusted force distribution in the upwind half of the AC leads to an optimal power output for the hybrid VAWT.

2.4. CONCLUSIONS

The flow mechanism of hybrid VAWT is complex due to the interaction between Darrieus and Savonius. It is known that the power output of the hybrid VAWT is reduced with the existence of the inner Savonius rotor. Many factors, such as airfoil efficiency and tip speed ratio, dominate the power output. Our understanding of power reduction is further improved by the research on the idealized turbine. To investigate the power performance of the idealized hybrid VAWT, the actuator disk and cylinder models are implemented using Eulerian RANS. The following outcomes are concluded.

- The numerical actuator model is validated against the theoretical actuator model. The extracted maximum power from the numerical actuator cylinder model has a discrepancy of around 0.598% compared to $c_{p_{Betz}}$.
- The maximum power output of the idealized hybrid VAWT with a given $c_{T_{AD}}$ is lower than that of a single actuator due to the non-optimal force distribution on the hybrid case. This indicates that a significant power increase of a hybrid VAWT cannot be realized by varying geometrical and operational parameters. The hybrid configuration is only beneficial to the start-up performance instead of the power performance.
- Given one of the operational conditions of the two actuators, we can determine the optimal condition for the idealized hybrid VAWT. Given a low $c_{T_{AC}} \leq 0.76$ for the idealized hybrid VAWT, we should increase the thrust coefficient of the inner AD to get the maximum power. While given a series of $c_{T_{AD}}$ for the idealized hybrid VAWT, it requires a higher $c_{T_{AC}}$ for low $c_{T_{AD}}$ case to gain the same amount of power as the high $c_{T_{AD}}$ case.
- The power loss in the idealized hybrid VAWT can be compensated by operating the inner AD, representing the idealized Savonius, as a propeller. The propeller-mode actuator balances off the power loss caused by the existence of the AD. The major contribution of increased power is that the actuator disk operating as a propeller prevents rotor blockage.
- Another form of power compensation is to adjust the force distribution of the outer AC. The power output of hybrid VAWT can be optimal by adjusting the upwind force distribution of AC to compensate for power losses caused by the inner AD. Among the studied cases, the hybrid VAWT has an optimal force distribution when adjusting the force distribution at $\psi = 8.25° \sim 34°$.

Overall, the results indicate that an idealized hybrid VAWT does not show a significant power increase compared to an optimal single Darrieus rotor. Therefore, the presence of a Savonius rotor inside a Darrieus rotor, considering losses from a non-ideal

system, will usually lead to a lower maximum power output. The hybrid configuration is primarily advantageous for the start-up performance of the combined rotor, which is not explored in this chapter. These results demonstrated that the numerical and theoretical results yield similar predictions in the low-thrust cases but show differences in the high-thrust cases, where the model reaches its limits of validity.

The complex flow dynamics of hybrid Vertical Axis Wind Turbines featuring a finite set of rotating blades remain unexplored in this thesis. This chapter intends to present a simplified representation of the system. The following chapter will counterpoint by employing a higher-fidelity Eulerian model to simulate the hybrid VAWT, incorporating discrete rotating blades. This approach will facilitate a detailed investigation of the turbine's aerodynamics, the interaction between the blade and vortex, and variations in blade force, utilizing Unsteady Reynolds-Averaged Navier-Stokes (URANS) simulations.

REFERENCES

[1] J. Pan, C. Ferreira, and A. van Zuijlen. Performance analysis of an idealized Darrieus–Savonius combined vertical axis wind turbine. *Wind Energy* n/a.n/a ().

[2] M. Mohamed. Impacts of solidity and hybrid system in small wind turbines performance. *Energy* 57 (Aug. 2013), pp. 495–504.

[3] M. Ahmad, A. Shahzad, and S. I. A. Shah. Experimental investigation and analysis of proposed hybrid vertical axis wind turbine design. *Energy Environment* (2023), p. 0958305X231181675.

[4] H. A. Madsen. "On the ideal and real energy conversion in a straight bladed vertical axis wind turbine". PhD thesis. Technical University of Denmark, 1983.

[5] M. Huang. "Wake and wind farm aerodynamics of vertical axis wind turbines". PhD thesis. 2023.

[6] D. De Tavernier. "Aerodynamic advances in vertical-axis wind turbines". PhD thesis. TU Delft, 2021.

[7] R. E. Froude. On the part played in propulsion by differences of fluid pressure. *Transactions of the Institution of Naval Architects* 30 (1889).

[8] M. Hansen. *Aerodynamics of Wind Turbines*. London, 2001.

[9] T. Burton, D. Sharpe, N. Jenkins, and E. Bossanyi. *Wind Energy Handbook*. Chichester, New York, Sept. 27, 2001.

[10] K. Chaney and A. Eggers. Expanding wake induction effects on thrust distribution on a rotor disc. *Wind Energy* 5.2-3 (2001), pp. 213–226.

[11] H. A. Madsen. "The Actuator Cylinder - A Flow Model for Vertical Axis Wind Turbines". PhD thesis. Technical University of Denmark, Jan. 1982.

[12] H. A. Madsen, U. S. Paulsen, and L. Vitae. Analysis of VAWT aerodynamics and design using the Actuator Cylinder flow model. *Journal of Physics: Conference Series* 555 (Dec. 2014), p. 012065.

[13] A. Ning. Actuator cylinder theory for multiple vertical axis wind turbines. *Wind Energy Science* 1.2 (Dec. 2016), pp. 327–340.

[14] A. Betz. *Introduction to the Theory of Flow Machines*. Oxford: Pergamon Press. 1966.

[15] P. Normandajc Lecanu, J. Breard, and D. Mouazé. *Simplified theory of an active lift turbine with controlled displacement*. 2016.

[16] J. Manwell, J. Mcgowan, and A. Rogers. In: *Wind Energy Explained: Theory, Design and Application*. Chichester, West Sussex, UK: John Wiley and Sons Ltd, Feb. 2012, pp. 92–96.

[17] OpenFOAM. *OpenFOAM User Guide*. 2017.

[18] R. Abdulkadirov and P. Lyakhov. Estimates of Mild Solutions of Navier–Stokes Equations in Weak Herz-Type Besov–Morrey Spaces. *Mathematics* 10.5 (Feb. 2022), p. 680.

[19] M. T. Bouzaher and M. Hadid. Active control of the vertical axis wind turbine by the association of flapping wings to their blades. *Procedia Computer Science* 52 (2015), pp. 714–722.

[20] J. Pan, C. Ferreira, and A. van Zuijlen. A numerical study on the blade–vortex interaction of a two-dimensional Darrieus–Savonius combined vertical axis wind turbine. *Physics of Fluids* 35.12 (2023).

[21] M. Huang, A. Sciacchitano, and C. Ferreira. On the wake deflection of vertical axis wind turbines by pitched blades. *Wind Energy* 26.4 (2023), pp. 365–387.

3

A HIGH-FIDELITY NUMERICAL STUDY ON THE BLADE-VORTEX INTERACTION OF A HYBRID VAWT

Parts of this chapter have been published in Physics of Fluids*.

In Chapter 2, the hybrid VAWT was represented by a fundamental formulation of a force field in an Eulerian RANS model. This chapter will use a higher-fidelity Eulerian URANS model for two-dimensional numerical analysis of vortex dynamics for a hybrid VAWT. The integration of a Savonius rotor in the hybrid VAWT improves self-starting capability but introduces vortices that cause transient load fluctuations on the Darrieus blades. This chapter attempts to characterize the flow features around the hybrid VAWT and correlate them with the Darrieus blade force variation in one revolution. The relevant position of Savonius and Darrieus blades (attachment angle $\gamma = 0°$-$90°$) and Savonius' tip speed ratio λ_S (0.2-0.8, varied Savonius' rotational speed) are investigated. This chapter contributes to a comprehensive understanding of flow dynamics in hybrid VAWTs, revealing the correlation between torque variation and vortex development.

*Jingna Pan, Carlos Ferreira, Alexander van Zuijlen, A numerical study on the blade–vortex interaction of a two-dimensional Darrieus–Savonius combined vertical axis wind turbine, Physics of Fluids 35, 125152 (2023) [1].

3.1. INTRODUCTION

Flow physics of hybrid VAWTs have been an important factor in studying power performance [2, 3, 4]. Chapter 2 has introduced a concept of idealized hybrid VAWT regarding power generation. As a result, the hybrid VAWT configuration mainly benefits from its start-up performance. This chapter is going to enhance the understanding of the hybrid VAWT and further investigate its flow features and blade forces.

Researchers have explored various aspects related to flow structures and turbine performance individually. There exists a gap in our understanding regarding the variation of blade force in response to vortex dynamics. In a word, a comprehensive discussion on the correlation between flow structures and turbine performances has not been thoroughly addressed yet. To address this gap, further studies are required to conduct in-depth analyses that correlate flow structures with specific turbine performance metrics. It involves identifying and quantifying the key flow features, such as vortices, wake interactions, turbulence patterns, and their direct influence on critical turbine parameters, such as power output, torque, and structural loading [5, 6]. This study is an extended work in terms of investigating the correlation between blade-vortex interaction and blade force variation.

The characterization and correlation of the vortex dynamics and blade torque play an important role in the design phase of the hybrid VAWT. Besides, the study of vortex dynamics might be useful for future studies on the engineering model of the hybrid VAWT [7, 8]. A parametric study of hybrid VAWT is conducted to better understand the flow mechanisms and performances of the hybrid VAWT. The presence of the Savonius rotor affects not only the rotor performance but also the downstream wake pattern. Their correlations are explored based on the Savonius-related parameters: attachment angle (position of Savonius blade relative to Darrieus blade) and Savonius' tip speed ratios (varied Savonius' rotation speed) in the current work.

The aforementioned geometrical parameter (attachment angle) and operational parameter (Savonius' tip speed ratio) are all 2D parameters. With the aim of characterizing the flow features of the hybrid VAWT and conducting a cost-effective parametric study, 2D simulations are considered sufficient in this study.

This chapter is structured as follows. The numerical procedure is presented in Section 3.2. The effects of attachment angle and Savonius' tip speed ratio on the hybrid VAWT performances and correlation of vortex dynamics and blade torque are analyzed in Section 3.3. The main results are concluded in Section 3.4, followed by the mesh independence study and meshing strategy in Appendices.

3.2. NUMERICAL PROCEDURE

3.2.1. GEOMETRY OF THE HYBRID TURBINE

The 2D simulations are conducted in OpenFOAM [9]. The hybrid VAWT consists of Savonius blades inside and Darrieus blades mounted on the same rotation axis. The Savonius rotor has two semi-circle blades without overlap and gap distance, which is a relevant work to Reference [10]. The Darrieus blades are chosen as NACA0021, corresponding to the work in Reference [11]. The geometrical and operational parameters of the hybrid VAWT are shown in TABLE 3.1, where $\lambda_S = \frac{\omega_S R_S}{U_\infty}$ and $\lambda_{hybrid} = \lambda_D = \frac{\omega_D R_D}{U_\infty}$.

The attachment angle γ and tip speed ratio of Savonius λ_S are varied to conduct an in-depth study that characterizes the flow structure relevant to blade force variation. It is worth noting that λ_S is changed by varying its rotation speed instead of radius because the operational condition is more convenient to control than the geometrical condition during turbine operation.

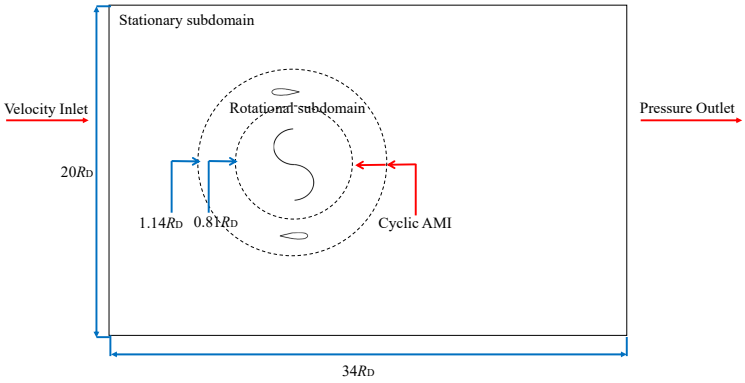

Figure 3.1: Computational domain and boundary conditions (Not true to scale)

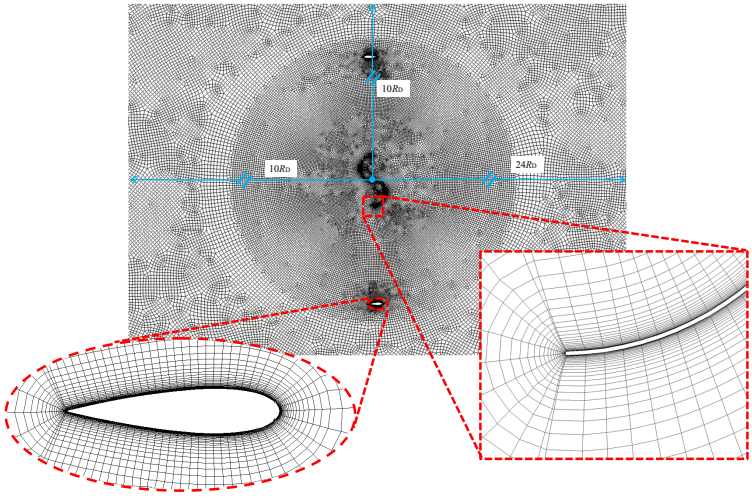

Figure 3.2: Mesh generation in the computational domain

Table 3.1: Detailed geometrical and operational information of the hybrid turbine

Parameter	Value / Specification	Unit
Radius of inner Savonius R_S	0.148	m
Radius of outer Darrieus R_D	0.74	m
Tip speed ratio of inner Savonius λ_S	[0.2, 0.4, 0.6, 0.8]	-
Tip speed ratio of outer Darrieus λ_D	[2.4, 2.9, 3.7, 4.0, 4.2]	-
Tip speed ratio of hybrid VAWT λ_{hybrid}	[1.0, 2.4, 2.9, 3.7, 4.0, 4.2]	-
Blade of inner Savonius	semi-circle	-
Blade of outer Darrieus	NACA0021	-
Chord length of outer Darrieus	0.075	m
Attachment angle γ	[0, 30, 60, 90]	°

3.2.2. TURBULENCE MODEL AND BOUNDARY CONDITIONS

The unsteady, incompressible Reynolds-averaged Navier–Stokes (URANS) equations are solved by PIMPLE (a combination of PISO (pressure-implicit split-operator) and SIMPLE(semi-implicit method for pressure-linked equations) algorithm to improve numerical accuracy upon multi sub-iterations. The governing equations include conservation of mass and conservation of momentum, which are expressed by Equation 3.1 and Equation 3.2, respectively. u_i and u_j represent the velocity components in the i and j directions. The model of Equation 3.2 reflects the fact that the flow around the rotating blade is turbulent, and closure of the URANS equations is achieved using shear stress transport (SST) k-w turbulence model. This turbulence model can predict boundary layers under strong adverse pressure gradients and has been validated in the application of wind turbines with good results [12, 13]. It predicts accurate results for separation flows [14, 15]. The turbulent kinetic energy k and dissipation rate w are expressed as Equations 3.3 and 3.4 [16, 17], respectively. In Equations 3.3 and 3.4, the generation of turbulent kinetic energy and dissipation rate are represented by G_w and G_k, respectively. Γ_k and Γ_w represent the effective diffusivity of k and w. Y_w and Y_k are the dissipation of w and k. S_k and S_w are source terms. D_w is the blending function for the standard k-ϵ and standard k-w model

[12, 13].

$$\frac{\partial u_i}{\partial x_i} = 0 \tag{3.1}$$

$$\rho \frac{\partial u_i}{\partial t} + \rho \frac{\partial (u_i u_j)}{\partial x_j} = -\frac{\partial p}{\partial x_i} + \frac{\partial}{\partial x_j}\left[(\mu + \mu_t) \frac{\partial u_i}{\partial x_j} \right] \tag{3.2}$$

$$\frac{\partial (\rho k)}{\partial t} + \frac{\partial (\rho k u_i)}{\partial x_i} = \frac{\partial}{\partial x_j}\left(\Gamma_k \frac{\partial k}{\partial x_j} \right) + G_k - Y_k + S_k \tag{3.3}$$

$$\frac{\partial (\rho w)}{\partial t} + \frac{\partial (\rho w u_i)}{\partial x_i} = \frac{\partial}{\partial x_j}\left(\Gamma_w \frac{\partial w}{\partial x_j} \right) + G_w - Y_w + D_w + S_w \tag{3.4}$$

The schematic of the computational domain and boundary conditions is depicted in Figure 3.1. The mesh details of the computational domain are shown in Figure 3.2. The inflow comes from left to right of the computational domain, the boundary conditions of the computational domain are determined as follows:

- Inlet boundary: The inlet wind speed is equal to freestream velocity;
- Outlet boundary: The given outlet pressure is standard ambient pressure;
- Wall boundary: No-slip rotating wall boundary conditions are used along the blade surfaces;
- Slip plane: There is a sliding mesh interface between the moving and the stationary grids. CyclicAMI boundary condition is employed to couple conditions between a pair of patches that share the same outer bounds. This boundary condition allows the physical rotation of the rotation subdomain. And the force variation would be well evaluated.

3.2.3. MESH INDEPENDENCE STUDY

Table 3.2: Power coefficient of hybrid VAWT from different mesh configurations, $\lambda_{hybrid} = 4.0$, $U_\infty = 4.01$m/s, $\gamma = 0°$

Mesh	Fine	Medium	Coarse
Number of cells	1.99e5	1.68e5	1.40e5
Darrieus blade discretization	102	76	66
Savonius blade discretization	304	220	140
Power coefficient c_p	0.3753	0.3694 (-1.57%)	0.3651 (-2.72%)

3.2.4. SENSITIVITY STUDY

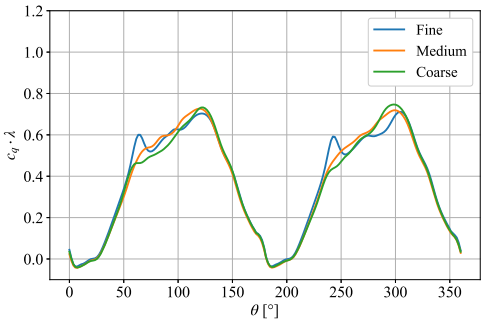

Figure 3.3: Power coefficient variation for hybrid VAWT with different mesh configurations, $\gamma = 0°$, $\frac{R_D}{R_S} = 5.0$, $\lambda_{hybrid} = 4.0$

A mesh independence study of a hybrid VAWT with two semicircular Savonius blades and two Darrieus blades is conducted to determine the appropriate cell size. Three mesh configurations (coarse, medium, fine) are involved with cell numbers of 1.99e5, 1.79e5, 1.40e5, respectively. The computational domain and the first-row's cell height are identical to the single-rotor case, as shown in the Appendix. The simulation residual and time step size are selected as 1e-5 and 0.24°/step to be consistent with the single Savonius and Darrieus simulations. The values of maximum skewness of the three mesh configurations are 0.70, 0.64, 0.67, respectively. The average dimensionless wall distance y^+ is

below one. The power coefficient from different mesh configurations and mesh details are shown in TABLE 3.2. The variations of the power coefficient are depicted in Figure 3.3. The power coefficients of the hybrid VAWT have a similar trend over the three mesh configurations. The fluctuations at θ = 60°-120° and θ = 240°-300° are attributed to the presence of Savonius' wake. This work will focus on torque fluctuation in response to the wake. The average power coefficients in TABLE 3.2 show that the medium mesh configuration yields reasonably accurate results with a 1.57% difference from the fine mesh configuration. To ensure cost-effective computations, a medium mesh is employed in the subsequent analysis.

3.2.5. TIME INDEPENDENCE STUDY

A time independence study for the hybrid VAWT has been conducted to verify the stability of the simulation. Azimuthal increments $d\theta$ of 0.06°, 0.12°, 0.24°, 0.48°, 0.96° and 4.8° are applied and the power coefficients c_p are shown in TABLE 3.3. Azimuthal increment of 4.8° tends to underestimate c_p by 5.1% compared to 0.06°. Among cases with $d\theta \leq 0.96°$, a negligible difference in c_p is observed. The comparison shows that $d\theta = 0.24°$ is a cost-effective choice in this study.

Table 3.3: Power coefficient of hybrid VAWT from different azimuthal increments, $\lambda_{hybrid} = 4.0$, $U_\infty = 4.01$m/s, $\gamma = 0°$

Azimuthal increment $d\theta$	0.06°	0.12°	0.24°	0.48°	0.96°	4.8°
Time step size dt [s]	4.83e-5	9.66e-5	1.932e-4	3.864e-4	7.728e-4	3.864e-3
Power coefficient c_p	0.3693	0.3693	0.3694	0.3693	0.3693	0.3504

The sensitivity study based on the computational domain size has been conducted. The distance between the rotor and domain outlet is varied from $18R_{hybrid}$, $24R_{hybrid}$ to $30R_{hybrid}$. The power coefficients of hybrid VAWT for computational domains with varied outlet distances are listed in TABLE 3.4. The difference between c_p for hybrid VAWT with outlet distance of $18R_{hybrid}$ and $30R_{hybrid}$ is about 13.02%. This deviation drops to 0.43% for the hybrid VAWT with the outlet distance of $24R_{hybrid}$. Therefore, the distance between the rotor and domain outlet is chosen as $24R_{hybrid}$.

Table 3.4: Power coefficient of hybrid VAWT from different distances between the rotor and domain outlet, $\lambda_{hybrid} = 4.0$, $U_\infty = 4.01$m/s, $\gamma = 0°$

Distance between rotor and outlet	$18R_{hybrid}$	$24R_{hybrid}$	$30R_{hybrid}$
Power coefficient c_p	0.3227 (-13.02%)	0.3694 (-0.43%)	0.3710

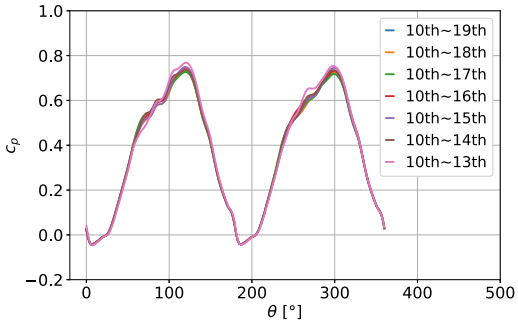

Figure 3.4: Power coefficient variation for hybrid VAWT in different numbers of revolution, $\gamma = 0°$, $\frac{R_D}{R_S} = 5.0$, $\lambda_{hybrid} = 4.0$

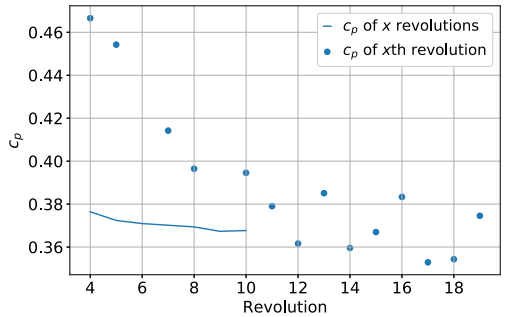

Figure 3.5: Mean power coefficient for hybrid VAWT in different revolutions and different numbers of revolutions, $\gamma = 0°$, $\frac{R_D}{R_S} = 5.0$, $\lambda_{hybrid} = 4.0$ (x-axis: Total number of revolution considered for the mean power coefficient)

Another sensitivity study examines the impact of varying numbers of revolutions on the average results. By systematically altering this parameter, we assess its influence on the power performances of the hybrid VAWT. This analysis provides insights into the stability and reliability of the findings, helping determine the optimal number of revolutions for obtaining consistent and representative results. The power coefficient variation

in one cycle for different numbers of revolution are shown in Figure 3.4. It is observed that the power coefficient tends to have an identical variation if more revolutions are taken into account. The mean power coefficient against different revolutions and different numbers of revolutions is depicted in Figure 3.5. Due to the complex turbulence around the hybrid VAWT, the mean power coefficient of the single revolution fluctuates between 0.36 and 0.38. The mean power coefficient of several revolutions tends to converge at a magnitude of 0.37 when the 10th to 17th revolutions are averaged. In this work, eight revolutions (10th~17th) are used for the calculation of the mean power coefficient for the hybrid VAWT.

3.3. RESULTS AND DISCUSSIONS

The start-up and power performances of a hybrid VAWT with a two-bladed Savonius and two-bladed Darrieus are estimated in this section. The effects of attachment angle and inner Savonius' tip speed ratio (varied Savonius' rotation speed) on the power performances of the hybrid VAWT are analyzed in this section. To further understand the flow physics of the hybrid VAWT, the Darrieus blade force variation is correlated with the wake patterns, which will provide insights into the hybrid VAWT design.

Power performances of single Savonius, single Darrieus and hybrid VAWT with various tip speed ratios are shown in Figure 3.6. The power coefficient of the hybrid VAWT is observed to be lower than that of the single Darrieus. The CFD simulations of Savonius have been validated against experimental results in Reference [18] by Blackwell. The numerical results of Darrieus are validated in Appendix B. There is a lack of experimental investigation on the studied hybrid VAWT, but a similar numerical method and meshing strategy have been applied to the hybrid VAWT. The sensitivity study of the hybrid VAWT indicates that the simulation stability and convergence are sufficient. The single Savonius results from experiments are lower than those from CFD simulations. This can be attributed to the absence of 3D effects (e.g., tip vortices), which are not discussed in this work.

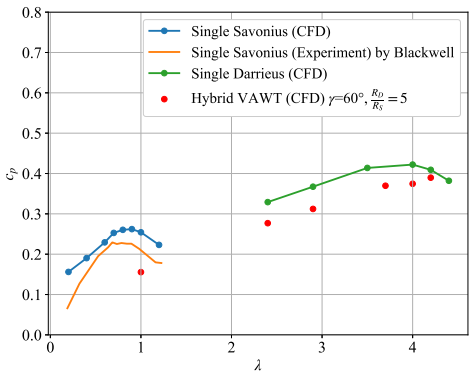

Figure 3.6: Power coefficient of single Savonius, single Darrieus and hybrid VAWT

3.3.1. START-UP PERFORMANCE

As shown in Figure 3.6, the single Savonius can operate at a tip speed ratio lower than 1, but the single Darrieus has a higher power output at high tip speed ratios. As studied in References [19, 20], reducing the size of Savonius would increase the maximum power performance of the hybrid VAWT. In Figure 3.6, the optimum tip speed ratio of the single Darrieus is about five times that of the single Savonius. So, the radius of the outer Darrieus part is selected as five times that of the inner Savonius part in the baseline hybrid VAWT to gain optimum power for the combined configuration as well as a good start-up performance.

The comparison of the torque coefficients for the single Savonius and Savonius in hybrid VAWT is shown in Figure 3.7. The variations of torque coefficient with tip speed ratio have the same trend: torque coefficient decreases with the increasing tip speed ratio. But the torque coefficient of Savonius in hybrid VAWT is lower than that of single Savonius due to the velocity deficit caused by the rotor rotating. The rotation of the hybrid VAWT leads to a high induction to the flow field, so the performance of the Savonius (or Darrieus) part in the hybrid VAWT is different from that of the single rotor with the same operational conditions. Since the Darrieus is the major contributor to the power generation in the hybrid VAWT, its tip speed ratio remains at optimal condition, and the effect of Savonius' tip speed ratio on the performance of the hybrid VAWT is studied. The Savonius' tip speed ratio is varied by changing the rotation speed of Savonius. Their flow features and blade forces are analyzed in Section 3.3.2.

As the Savonius blade position at static conditions influences the static torque [21], the static torque of the Savonius blade in hybrid VAWT is investigated under varied angular positions. The static torque coefficients of the single Savonius and Savonius in hybrid VAWT are compared in Figure 3.8. It is observed that the Savonius in hybrid VAWT has a similar static torque variation to the single Savonius. The static torque is positive at most phase positions except 50°-69°. So, the hybrid VAWT can self-start at most positions.

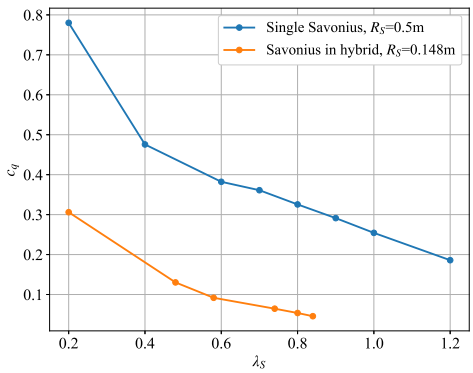

Figure 3.7: Torque coefficients of single Savonius and Savonius in hybrid VAWT

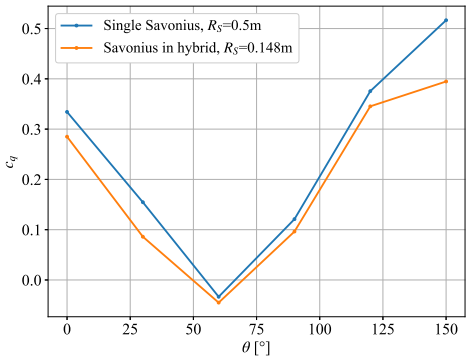

Figure 3.8: Static torque coefficient of single Savonius and Savonius in hybrid VAWT

3.3.2. POWER PERFORMANCE

Regarding the hybrid VAWT, advantages are taken from two types of single rotors in the way of starting up easily and maintaining as high power as a single Darrieus. However, the presence of Savonius in hybrid VAWT would suppress power generation [20]. This section aims to find out the correlation between torque variation and vortex dynamics with varied attachment angle and Savonius' tip speed ratio (varied Savonius' rotation speed) in one revolution.

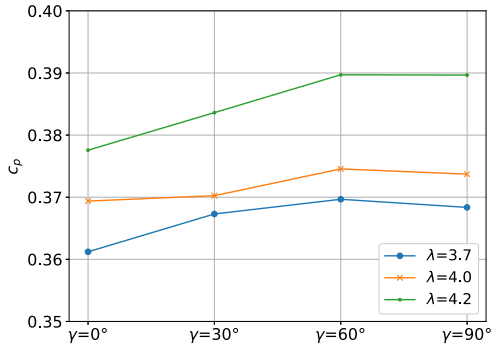

Figure 3.9: Effect of λ_{hybrid} on power coefficient of hybrid VAWT, $\frac{R_D}{R_S} = 5$

EFFECT OF ATTACHMENT ANGLE

To understand the vortex dynamics effects on the blade forces, a detailed blade-vortex interaction study is conducted in this section. The interaction scheme between Savonius' wake and Darrieus blade is varied by the attachment angle. The power coefficients of hybrid VAWT with four attachment angles are depicted in Figure 3.9 at three tip speed ratios. It is observed that hybrid VAWT with $\gamma = 60°$ and 90° generates a relatively high power coefficient regardless of tip speed ratio.

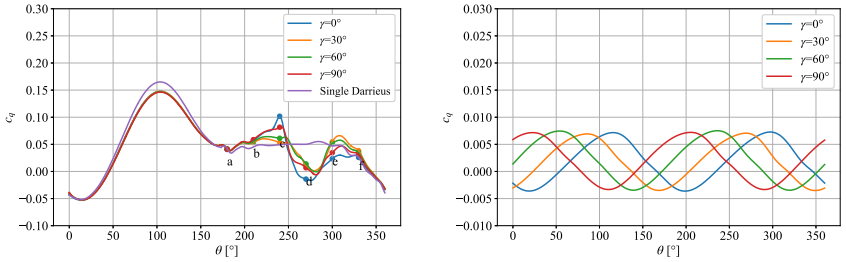

(a) Darrieus blade in hybrid turbine

(b) Savonius blade in hybrid turbine

Figure 3.10: Effect of attachment angle on the torque generation of Darrieus and Savonius blade, $\lambda_{hybrid} = \lambda_D = 4$, $\frac{R_D}{R_S} = 5$, (a) Darrieus blade in hybrid turbine, (b) Savonius blade in hybrid turbine

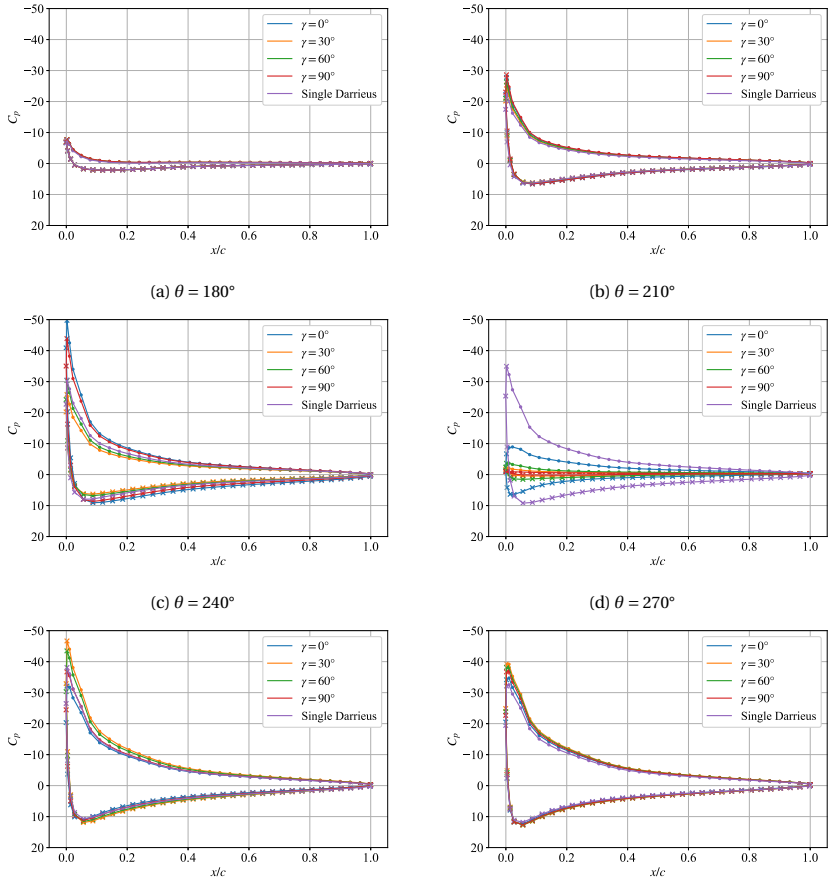

(a) $\theta = 180°$

(b) $\theta = 210°$

(c) $\theta = 240°$

(d) $\theta = 270°$

(e) $\theta = 300°$

(f) $\theta = 330°$

Figure 3.11: Effect of attachment angle on the pressure distribution along the Darrieus blade, $\lambda_{hybrid} = \lambda_D = 4$, $\frac{R_D}{R_S} = 5$, (a) $\theta = 180°$, (b) $\theta = 210°$, (c) $\theta = 240°$, (d) $\theta = 270°$, (e) $\theta = 300°$, (f) $\theta = 330°$

Taking an example of λ_{hybrid} = 4.0, the torque contributions of the Darrieus and Savonius blades in the hybrid VAWT are discussed below. The effect of attachment angle on the torque generation of the Darrieus and Savonius blades is shown in Figure 3.10. It is observed that the torque variation trend of the Savonius blade in hybrid VAWT shows very little variation in different attachment angles, while that of the Darrieus blade in hybrid VAWT is highly distinguished at θ = 180°-360°. The presence of the Savonius reduces the upwind Darrieus blade torque in hybrid VAWT due to the blockage effect. The torque coefficient in $\gamma = 0°$ decreases from 0.10 to -0.013 in 30°. Its gradient ($\frac{0.10+0.013}{30} = 0.0038$) is larger than the other three cases, which are 0.0022, 0.0016, and 0.0013 for γ = 90°, 60° and 30°, respectively. Besides, the difference between the maximum and minimum torque coefficients in the second-half rotation of γ = 0° is the highest among the four cases. The rapid variation of the blade forces occurring in the second-half rotation may cause fatigue loads for the Darrieus blade.

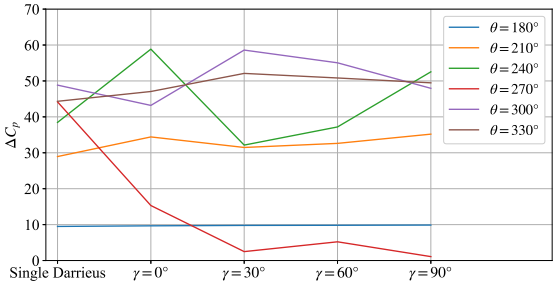

Figure 3.12: Variation of pressure difference with varied attachment angles at different phases, $\Delta C_p = C_{p_{max}}$ - $C_{p_{min}}$

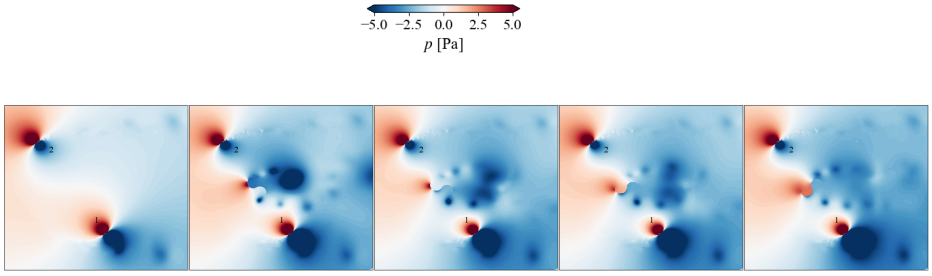

(a) Single Darrieus (b) $\gamma = 0°$ (c) $\gamma = 30°$ (d) $\gamma = 60°$ (e) $\gamma = 90°$

Figure 3.13: Pressure fields of the single Darrieus and hybrid VAWT at θ = 210°, (a) Single Darrieus, (b) $\gamma = 0°$, (c) $\gamma = 30°$, (d) $\gamma = 60°$, (e) $\gamma = 90°$

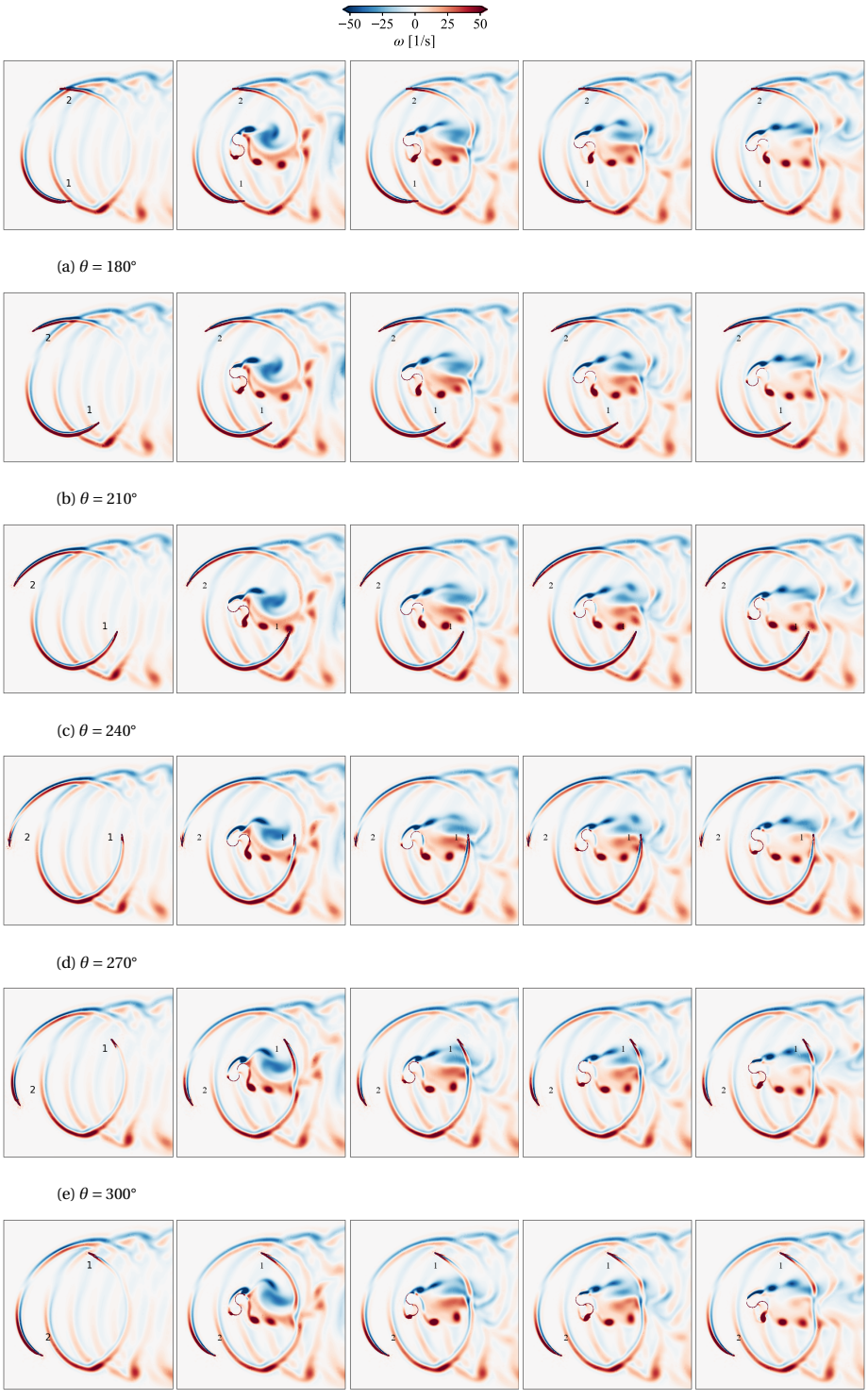

(a) $\theta = 180°$

(b) $\theta = 210°$

(c) $\theta = 240°$

(d) $\theta = 270°$

(e) $\theta = 300°$

(f) $\theta = 330°$

Figure 3.14: Effect of γ on vorticity fields at six phase angles, $\lambda_{hybrid} = 4$, $\lambda_S = 0.8$, $\frac{R_D}{R_S} = 5$, (a) $\theta = 180°$, (b) $\theta = 210°$, (c) $\theta = 240°$, (d) $\theta = 270°$, (e) $\theta = 300°$, (f) $\theta = 330°$ (Left to right: Single Darrieus, $\gamma = 0°$, $\gamma = 30°$, $\gamma = 60°$, $\gamma = 90°$)

To study the effects of attachment angle on the blade forces and correlate the vortex dynamics to the blade forces, the pressure distributions along the blade surface and the vorticity fields at different phase angles are depicted in Figure 3.11 and Figure 3.14, respectively. The difference between maximum and minimum pressure coefficients on the Darrieus blade is denoted by ΔC_p. Its variation with attachment angles is shown in Figure 3.12. Through analysis of pressure distribution and vorticity field at $\theta = 180°$, 210° and 330° (denoted by phases a, b, and f), blade 1 is not significantly affected by the perturbed region due to the presence of Savonius part, so the pressure distributions and pressure differences slightly vary with the attachment angles. It indicates that the attachment angle shows little effect on the torque when the Darrieus blade is outside of the Savonius' wake region. This also indicates the benefits of the large radius ratio to the power performance of the hybrid VAWT. In Figure 3.10a, it is observed that the torque coefficient of the Darrieus blade in the hybrid VAWT increases with the phase angle ranging from $\theta = 180°$ to $\theta = 240°$. The pressure fields of the single Darrieus and hybrid VAWT at $\theta = 210°$ are shown in Figure 3.13. The low-pressure region at the outer side of the Darrieus blade in hybrid VAWT is larger than that in single Darrieus. The increasing size of the low-pressure region at the outer side of the Darrieus blade is attributed to the vortex flow behind the Savonius rotor. The torque is observed to increase from $\theta = 180°$ to $\theta = 240°$ in Figure 3.10a, which can be attributed to the rotation of the Darrieus blade from the high-pressure region to the low-pressure region (Savonius' wake region).

At $\theta \approx 240°$ (phase c), blade 1 rotates into the shed vortex from the advanced Savonius blade. For $\gamma = 0°$ and 90°, the leading edge of blade 1 is approaching the shed vortex from the advanced Savonius blade. In Figures 3.11c and 3.12, the pressure differences of $\gamma = 0°$ and 90° at $\theta = 240°$ are larger than ΔC_p of single Darrieus, leading to a higher torque generation compared to the single Darrieus. The pressure differences at $\gamma = 30°$ and 60° are lower than the single Darrieus, but their torque coefficients are still higher than the single Darrieus. It is worth noting that forces and moments are output in their total and constituent components in OpenFOAM [9]. In this work, the sum of pressure and viscous contributions to moments is equal to the blade torque. Because blade 1 interacts with the shed vortex of Savonius directly at $\gamma = 0°$ and 90° as shown in Figure 3.14c, where the pressure contribution dominates the torque generation. While blade 1 at $\gamma = 30°$ and 60° do not directly interact with shed vortices, in which case the viscous contribution dominates the torque generation.

After $\theta = 240°$ (after phase c), blade 1 goes through the large separated region behind the Savonius, where the Darrieus blade has a strong interaction with the Savonius' wake and a significant velocity deficit. Compared to the single Darrieus case, less power can be converted by the rotor [22]. At $\theta = 270°$ (phase d), the pressure coefficients and adverse pressure gradient at the leading edge decrease as the attachment angle increases. In Figure 3.12, the pressure difference of the hybrid VAWT is lower compared to the single Darrieus. At this phase, the Darrieus blade torque drops to a certain amount and experiences a subsequent increase due to the flow perturbances of Savonius. It is observed that blade 1 interacts with the shed vortices from the two Savonius blades at $\gamma = 30°$-90°. This interaction between blade 1 and wake makes the flow around the blade more perturbed so that the the flow near the blade internal side differs much from the external side, in which case the pressure contribution dominates the torque generation. This

leads to a torque decrease with the pressure difference decrease. The torque generation at $\gamma = 30°$-$90°$ is more than $\gamma = 0°$, but the pressure differences of the former three cases are lower than that of the latter case because blade 1 is situated in between the shed vortices from the advancing and advanced Savonius blades in the case of $\gamma = 0°$ where viscous contribution dominates the torque generation. So, the attachment angle of 30°-90° can be used as a flow control guide to reduce power losses from downstream blades of the hybrid VAWT.

At $\theta = 300°$ (phase e), blade 1 is rotating out of the Savonius wake disturbances. The shed vortex from the advancing Savonius blade appears on the internal side of blade 1, and the pressure difference between the internal and external sides of blade 1 increases compared to $\theta = 270°$ (phase d). The torque coefficient of blade 1 at phase e yields a higher magnitude than that at phase d. In Figure 3.14e, for cases where $\gamma = 30°$ and 60°, blade 1 is notably influenced to a greater extent by the nearby shed vortices originating from the advancing Savonius blade in comparison to cases where $\gamma = 0°$ and 90°. The pressure differences and torque coefficients at $\gamma = 30°$ and 60° are higher, and the Darrieus blades have higher adverse pressure gradients compared to those at $\gamma = 0°$ and 90°.

Overall, the toque generations of the four attachment angles at $\theta = 240°$ and 210° are higher compared to the single Darrieus blade, shown in Figure 3.10. Therefore, the shed vortex from the advanced Savonius blade increases the torque generation. This dependency of the torque increase on the shed vortex from the advanced Savonius blade is observed in various attachment angle cases.

Effect of Savonius' rotation speed

As the inner Savonius perceives a lower incoming flow during rotation of the hybrid VAWT, the equivalent tip speed ratio for Savonius is different from the original tip speed ratio. To study the effect of Savonius' rotation on the hybrid VAWT, Savonius and Darrieus are assumed to be mounted in separate rotation axes. The relation between the original tip speed ratio and the power coefficient of the hybrid VAWT is shown in TABLE 3.5. It shows a slight power increase for the case with a lower λ_S. Therefore, slowing down the inner Savonius after start-up is beneficial for the power performance of the hybrid VAWT. Reducing the size of the inner Savonius leads to the same effect, but it is difficult to achieve during turbine operation. Apart from the mean power of the hybrid VAWT, the torque variation during rotation is also analyzed.

Table 3.5: Power coefficient of hybrid VAWT with different rotation speeds of Savonius, $\lambda_{hybrid} = 4.0$, $\gamma = 0°$

	$\lambda_S = 0.2$	$\lambda_S = 0.4$	$\lambda_S = 0.6$	$\lambda_S = 0.8$
$c_{p_{hybrid}}$	0.40007	0.38982	0.38462	0.36938

The torque variations of blade 1 in hybrid VAWT and single Darrieus are compared in Figure 3.15. The force fluctuation in the second-half revolution is investigated. The torque coefficient at $\lambda_S = 0.8$ has the most rapid change compared to the other three

cases. This is due to the large shedding frequency of the Savonius's wake. So, there is a higher possibility of the occurrence of fatigue. From $\theta = 180°$ to $\theta = 240°$, the same trends of torque increase as the varied γ cases are observed due to the blade rotation from high-pressure region to low-pressure region (Savonius' wake region).

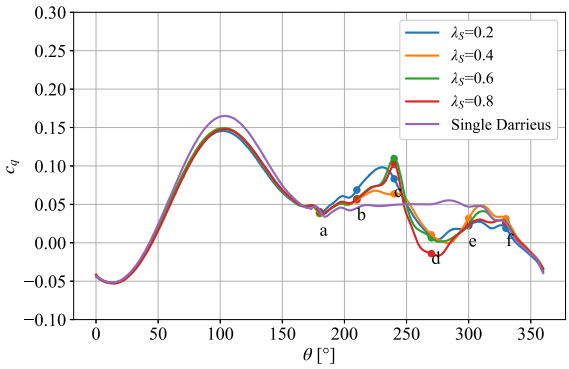

Figure 3.15: Effect of Savonius' tip speed ratio on torque variation of the top Darrieus blade in hybrid VAWT and single Darrieus, $\lambda_{hybrid} = \lambda_D = 4$ ($\gamma = 0°$, $\lambda_S = \frac{\Omega_S R_S}{U_\infty}$)

To analyze flow physics in the second-half revolution of hybrid VAWT with varied λ_S, six angular positions from 180° to 330° are denoted by phases a to f. The pressure distribution along the blade surface, pressure difference between the maximum and minimum values, and vorticity field around the rotor at the six phases are shown in Figures 3.17, 3.16 and 3.18, respectively. The torque coefficients of blade 1 in the single Darrieus rotor at $\theta = 180°$ and 330° (phases a and f) are similar to those in the hybrid VAWT when varying the rotation speed of the inner Savonius because blade 1 only interacts with the wake shedding from the Darrieus blades, with no disturbances introduced from the Savonius wake. At $\theta = 210°$ (phase b), blade 1 rotates towards the shed vortex shed from the advanced Savonius blade tip. As the size of the shed vortex blob grows with the decreasing rotation speed, the pressure difference between the internal and external sides of blade 1 and its torque coefficient at $\lambda_S = 0.2$ is higher compared to that at $\lambda_S = 0.4$-0.6. At $\theta = 240°$ (phase c) $\lambda_S = 0.6$ and 0.8, the shed vortex from the advanced Savonius blade appears at the internal side of the blade 1, resulting in a stronger adverse pressure gradient and larger pressure difference at the leading edge. The torque generation is also higher than $\lambda_S = 0.2$ and 0.4.

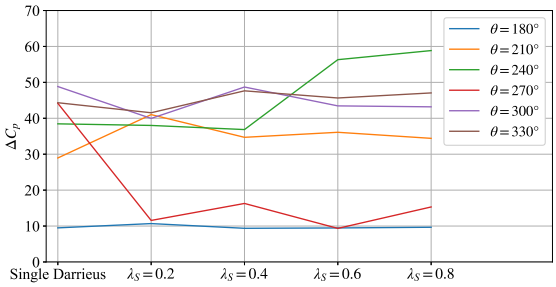

Figure 3.16: Variation of pressure difference with varied Savonius' tip speed ratios at different phases, $\Delta C_p = C_{p_{max}} - C_{p_{min}}$

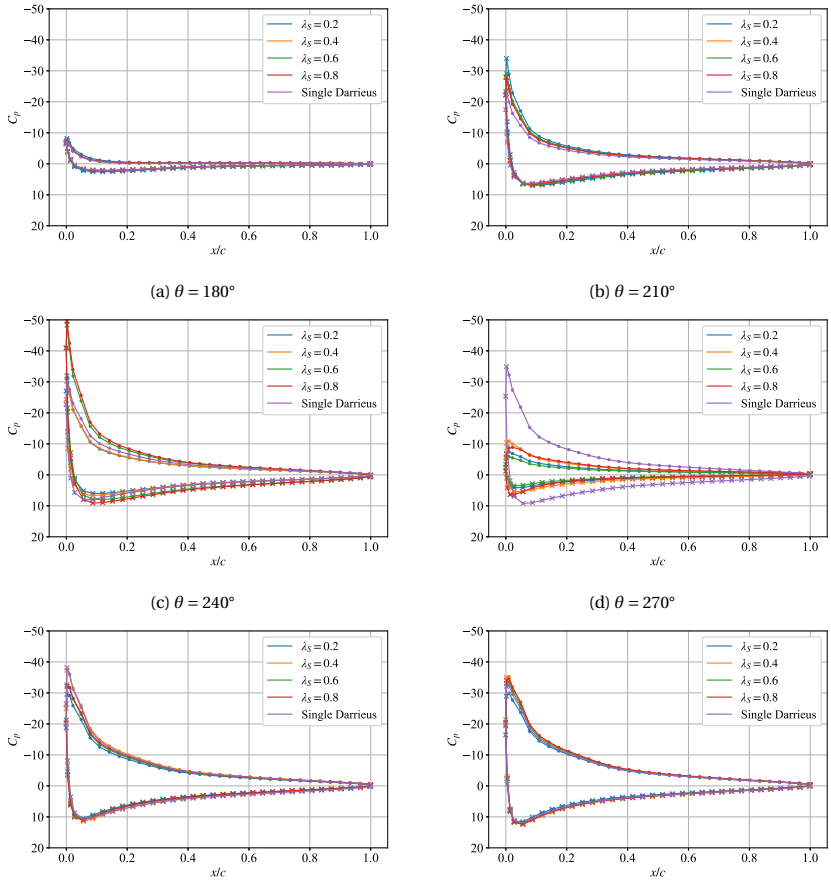

(a) $\theta = 180°$ (b) $\theta = 210°$

(c) $\theta = 240°$ (d) $\theta = 270°$

(e) $\theta = 300°$ (f) $\theta = 330°$

Figure 3.17: Effect of λ_S on the pressure distribution along the Darrieus blade, $\lambda_{hybrid} = \lambda_D = 4$, $\frac{R_D}{R_S} = 5$, (a) $\theta = 180°$, (b) $\theta = 210°$, (c) $\theta = 240°$, (d) $\theta = 270°$, (e) $\theta = 300°$, (f) $\theta = 330°$

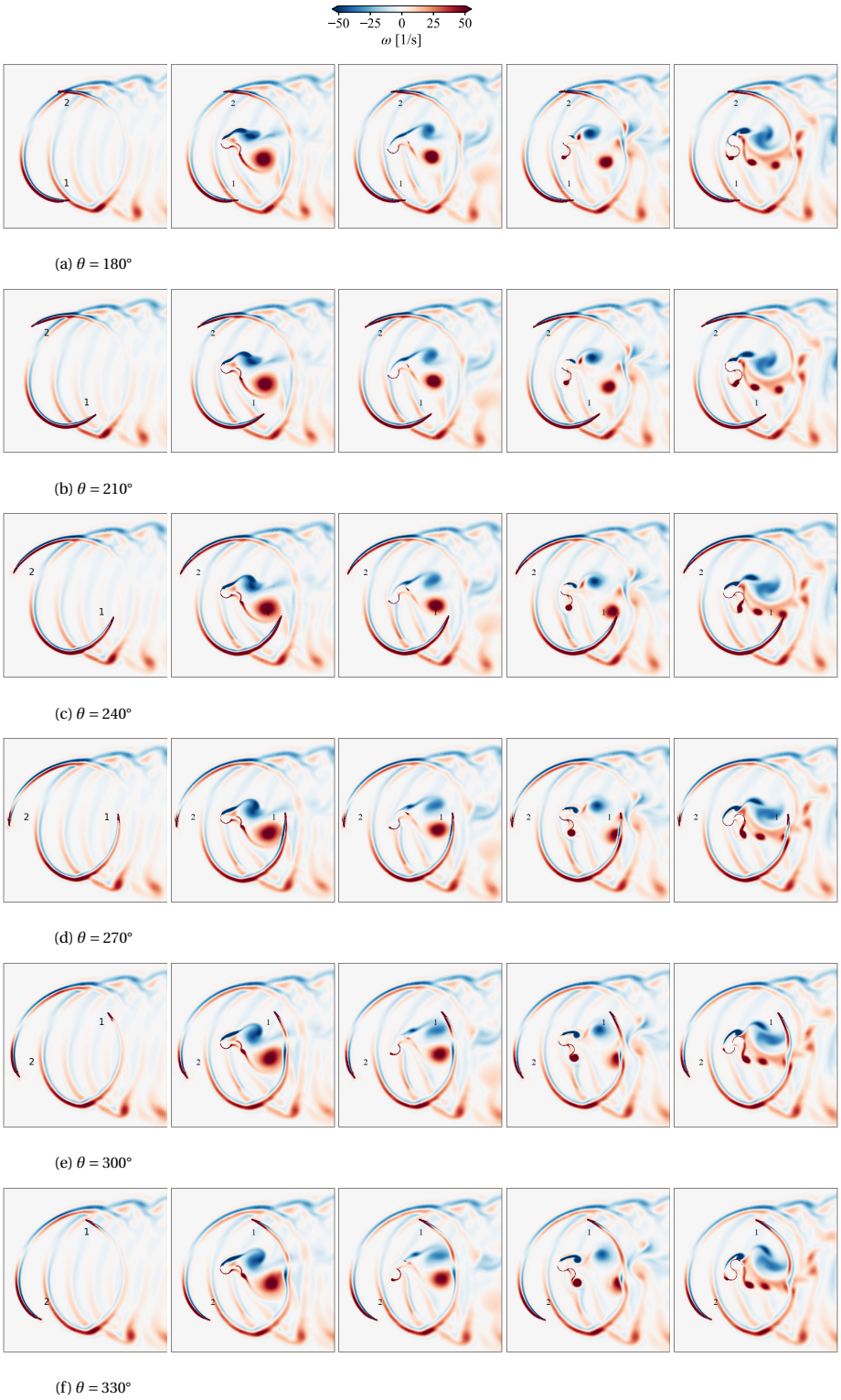

(a) $\theta = 180°$

(b) $\theta = 210°$

(c) $\theta = 240°$

(d) $\theta = 270°$

(e) $\theta = 300°$

(f) $\theta = 330°$

Figure 3.18: Effect of λ_S on vorticity fields at six phase angles, $\lambda_{hybrid} = 4$, $\gamma = 0°$, $\frac{R_D}{R_S} = 5$, (a) $\theta = 180°$, (b) $\theta = 210°$, (c) $\theta = 240°$, (d) $\theta = 270°$, (e) $\theta = 300°$, (f) $\theta = 330°$ (Left to right: Single Darrieus, $\lambda_S = 0.2$, $\lambda_S = 0.4$, $\lambda_S = 0.6$, $\lambda_S = 0.8$)

At $\theta = 270°$ (phase d), blade 1 is behind the Savonius and experiences a large velocity deficit. The pressure difference between the internal and external sides of the leading edge reduces, leading to the reduction of torque generation. $\lambda_S = 0.8$ has more power losses than the other cases due to Savonius' high induction to the flow field. So, reducing the rotation speed of inner Savonius would decrease the power losses downstream. Compared to the single Darrieus, the pressure differences of blade 1 in hybrid VAWT at four Savonius' tip speed ratios are lower, shown in Figures 3.17 and 3.16. It is observed that the pressure difference decreases in the order of single Darrieus, $\lambda_S = 0.4$, $\lambda_S = 0.8$, $\lambda_S = 0.2$, $\lambda_S = 0.6$, but the blade torque decreased in the order of single Darrieus, $\lambda_S = 0.4$, $\lambda_S = 0.2$, $\lambda_S = 0.6$, $\lambda_S = 0.8$. The outlier $\lambda_S = 0.8$ may be because the pressure contribution cannot dominate the blade torque generation. At $\theta = 300°$ (phase e), blade 1 rotates outwards of the shed vortex from the advancing Savonius blade. At $\lambda_S = 0.4$, the near vortex has a bigger impact on blade 1 compared to the other Savonius' tip speed ratios, leading to the highest ΔC_p and c_q at $\theta = 300°$.

3.4. CONCLUSIONS

The effects of attachment angle and Savonius' rotation speed on the blade-vortex interaction and performances of a hybrid VAWT have been thoroughly investigated in the present chapter. The studies were conducted employing a computational fluid dynamic approach. Four attachment angles for the hybrid VAWT and four rotation speeds for the inner Savonius have been evaluated systematically. Several conclusions can be drawn from the chapter:

1. The two-bladed Savonius without gap distance can self-start at most phase angles except 50°-69°.

2. At $\gamma = 60°$ and 90°, the power coefficient of the hybrid VAWT is larger compared to 0° and 30°.

3. In the downwind part, the torque variation is dependent on the blade-vortex interaction. The torque coefficient of the Darrieus blade in hybrid VAWT is higher than that in the single Darrieus while the blade interacts with the shed vortex from the advanced Savonius blade. This dependency is observed in varied attachment angles and varied tip speed ratio cases.

4. The effect of Savonius' rotation on the performance of the hybrid VAWT is studied. The results indicate that slowing down the Savonius in hybrid VAWT leads to less induction to the flow field and more available energy downstream. Lower λ_S is beneficial to the power performance of the Darrieus part in the hybrid VAWT regardless of the complex mechanics of the rotation axis.

5. From $\theta = 180°$ to 240°, the blade torque increases with the increasing phase angle because the Darrieus blade rotates from high-pressure region to low-pressure region (Savonius' wake region), leading to the torque increase in the rotation direction.

6. When the Darrieus blade does not interact directly with shed vortices, e.g., blade 1 is situated in between vortices at $\theta = 270°$, $\lambda_S = 0.8$, the viscous contribution would dominate the torque generation.

7. A rapid force variation occurs when the Darrieus blade interacts with the Savonius' wake. The Darrieus blade in hybrid VAWT with $\gamma = 0°$ and $\lambda_S = 0.8$ has the largest gradient of force drop, which might lead to fatigue for the hybrid VAWT.

From the power and start-up performance point of view, it is suggested to apply an attachment angle of 60° or 90°, and low λ_S of 0.2 to improve the rotor performance.

This chapter tackled the relation between the blade-vortex interaction and blade forces of hybrid VAWT using high-fidelity simulation. Results demonstrate the capability of numerical modeling in handling a wide range of operational conditions: the relevant position of Savonius and Darrieus blades (attachment angle $\gamma = 0°$-90°) and Savonius' tip speed ratio λ_S (0.2-0.8, varied Savonius' rotational speed). This is an extremely expensive tool as mentioned in Chapter 1. In the following work, a less expensive method is going to be explored and its computational efficiency and accuracy are estimated in various types of VAWTs.

REFERENCES

[1] J. Pan, C. Ferreira, and A. van Zuijlen. A numerical study on the blade–vortex interaction of a two-dimensional Darrieus–Savonius combined vertical axis wind turbine. *Physics of Fluids* 35.12 (2023).

[2] M. Asadi and R. Hassanzadeh. Effects of internal rotor parameters on the performance of a two bladed Darrieus-two bladed Savonius hybrid wind turbine. *Energy Conversion and Management* 238 (2021), p. 114109.

[3] S. Chegini, M. Asadbeigi, F. Ghafoorian, and M. Mehrpooya. An investigation into the self-starting of darrieus-savonius hybrid wind turbine and performance enhancement through innovative deflectors: A CFD approach. *Ocean Engineering* 287 (2023), p. 115910.

[4] S. Bhuyan and A. Biswas. Investigations on self-starting and performance characteristics of simple H and hybrid H-Savonius vertical axis wind rotors. *Energy Conversion and Management* 87 (2014), pp. 859–867.

[5] J. Pacheco, F. Pimenta, S. Guimarães, G. Castro, Á. Cunha, J. C. Matos, and F. Magalhães. Experimental evaluation of fatigue in wind turbine blades with wake effects. *Engineering Structures* 300 (Feb. 2024), p. 117140.

[6] K. Shaler, K. M. Kecskemety, and J. J. McNamara. "Wake Interaction Effects Using a Parallelized Free Vortex Wake Model". In: *34th Wind Energy Symposium*. American Institute of Aeronautics and Astronautics, Jan. 2016.

[7] A. Zanon, P. Giannattasio, and C. J. Simão Ferreira. A vortex panel model for the simulation of the wake flow past a vertical axis wind turbine in dynamic stall. *Wind Energy* 16.5 (June 2012), pp. 661–680.

[8] G. Tescione. "On the aerodynamics of a vertical axis wind turbine wake". PhD thesis. 2016.

[9] OpenFOAM. *OpenFOAM User Guide*. 2017.

[10] J. Pan, C. Ferreira, and A. vanZuijlen. Estimation of power performances and flow characteristics for a Savonius rotor by vortex particle method. *Wind Energy* 26.1 (Jan. 2023), pp. 76–97.

[11] B. LeBlanc and C. Ferreira. Estimation of blade loads for a variable pitch vertical axis wind turbine from particle image velocimetry. *Wind Energy* 25.2 (2022), pp. 313–332.

[12] C. D. Argyropoulos and N. Markatos. Recent advances on the numerical modelling of turbulent flows. *Applied Mathematical Modelling* 39.2 (2015), pp. 693–732.

[13] S. Aftab, A. Mohd Rafie, N. Razak, and K. Ahmad. Turbulence model selection for low Reynolds number flows. *PloS one* 11.4 (2016), e0153755.

[14] F. R. Menter. Two-equation eddy-viscosity turbulence models for engineering applications. *AIAA journal* 32.8 (1994), pp. 1598–1605.

[15] F. R. Menter, M. Kuntz, R. Langtry, et al. Ten years of industrial experience with the SST turbulence model. *Turbulence, heat and mass transfer* 4.1 (2003), pp. 625–632.

[16] D. C. Wilcox. Reassessment of the scale-determining equation for advanced turbulence models. *AIAA Journal* 26.11 (1988), pp. 1299–1310.

[17] D. Wilcox. *Turbulence Modeling for CFD (Third Edition) (Hardcover)*. Jan. 2006.

[18] B. F. Blackwell, L. V. Feltz, and R. E. Sheldahl. *Wind tunnel performance data for two-and three-bucket Savonius rotors*. Sandia Laboratories Springfield, VA, USA, 1977.

[19] P. Kumar, M. Surya, K. Sivalingam, T.-C. Lim, S. Ramakrishna, and W. he. Computational Optimization of Adaptive Hybrid Darrieus Turbine: Part 1. *Fluids* 4 (May 2019), p. 90.

[20] K. Liu, M. Yu, and W. Zhu. Enhancing wind energy harvesting performance of vertical axis wind turbines with a new hybrid design: A fluid-structure interaction study. *Renewable Energy* 140 (Sept. 2019), pp. 912–927.

[21] M. H. M. Yazik, W. S. Chang, M. H. H. Ishak, E. Fatahian, and F. Ismail. Effect of surface roughness and blade material on the performance of a stationary Savonius wind turbine under different operating conditions. *Physics of Fluids* 35.3 (Mar. 2023).

[22] A. Pallotta, D. Pietrogiacomi, and G. P. Romano. HYBRI – A combined Savonius-Darrieus wind turbine: Performances and flow fields. *Energy* 191 (2020), p. 116433.

III

LAGRANGIAN METHOD

4

ESTIMATION OF POWER PERFORMANCE AND FLOW FEATURES FOR A SAVONIUS ROTOR BY VORTEX PARTICLE METHOD

Parts of this chapter have been published in Wind Energy*.

Chapters 2 and 3 have studied flow physics of VAWTs using Eulerian methods. However, they require relatively high computational time and resources. In this chapter, Savonius' performance will be examined using a cost-effective vortex method. The efficiency and accuracy of the vortex particle method (VPM) are investigated in estimating the power performance and flow characteristics of a Savonius rotor. VPM used for airfoils always have a clearly defined leading/trailing edges. But this does not apply to the Savonius rotor. In this chapter, a double-trailing-edge-wake-modelling vortex particle method (DTVPM) is presented to extend the working range of VPM for dealing with full rotation amplitudes (0°-360°) and high tip speed ratios (TSRs, 1.0 and 1.2) of Savonius rotors. DTVPM results in symmetrical torque predictions for a Savonius rotor. However, due to the absence of viscous effects near the surface in DTVPM, the original method cannot capture detailed wake structures at high TSRs (1.0, 1.2). To capture complex wake structures, such as reverse flow structures, the addition of viscous correction for trailing-edge vortices (TEVs) is suggested in this chapter. This chapter focuses on the simulation and validation of DTVPM for predicting torque coefficients and wake patterns, as well as comparisons to URANS results to evaluate the accuracy and efficiency of the method. Two-dimensional and incompressible flow is assumed and TSR ranges between 0.2 and 1.2. For the studied cases, a maximum power coefficient is obtained at a TSR of around 0.8*, consistent with published experimental data. In addition, the process of trailing-edge vortex generation and detachment is captured by DTVPM.*

*Jingna Pan, Carlos Ferreira, Alexander van Zuijlen, Estimation of power performances and flow characteristics for a Savonius rotor by vortex particle method, Wind Energy 26 (1), 76-97 (2023) [1].

4.1. INTRODUCTION

The conventional Savonius rotors play a key role in the start-up performance of hybrid VAWTs [2, 3, 4]. The computational efficiency of VAWTs matters for the design of hybrid VAWTs. The vortex method is one of the alternatives to Eulerian methods. In this chapter, a double-trailing-edge-wake-modeling vortex particle method (DTVPM) is presented to adapt VPM for Savonius rotors without gap width. Because VPM cannot predict viscous flow due to the assumption of incompressible potential flow, the viscous effect is considered by a self-correction procedure for tip vortices in DTVPM. As a result, the simulation of DTVPM with viscous correction improves the accuracy of predictions, as will be discussed in the following sections.

This chapter focuses on elucidating DTVPM simulation and validating it against Eulerian URANS model and is structured as follows. The modeling information is elaborated in Section 4.2. The proposed method is then applied to a Savonius rotor without gap width and compared with Eulerian URANS model and published experimental results in Section 4.3. The effects of tip speed ratio λ (TSR) and phase angle θ on power performances and flow characteristics are also investigated. Conclusions are discussed in Section 4.4.

4.2. NUMERICAL PROCEDURE

This section elaborate the simulation of DTVPM in the case of a Savonius rotor. The Savonius tips are defined as two trailing edges to avoid the asymmetrical force prediction. The viscous effects are also taken into account to enhance the computational accuracy of DTVPM. Detailed information about the corresponding numerical simulation and published experimental setup are included in this section.

4.2.1. PRINCIPLE OF VPM

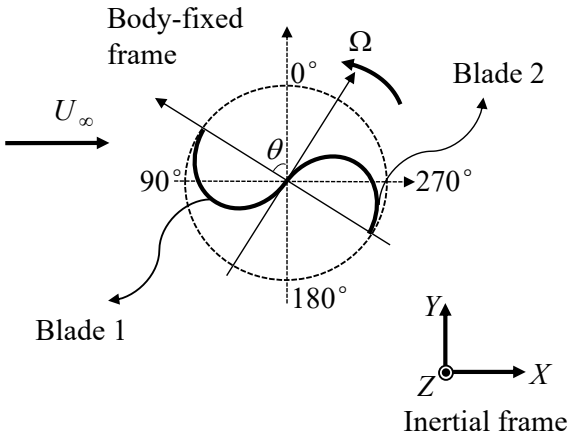

Figure 4.1: Schematic of a Savonius rotor

A schematic of the Savonius rotor is depicted in Figure 4.1. It includes two semicircular blades and a rotational axis located at the origin. The VPM is employed to simulate the incompressible flow around the 2D Savonius. It is based on the Navier-Stokes (NS) equation, describing fluid dynamics in the velocity $\vec{u}$ and vorticity $\vec{\omega}$ formulation at time t [5, 6, 7]. For the incompressible inviscid flow, the continuity equation is given by Equation 4.1. The NS equation in terms of vorticity is written as Equation 4.2 assuming viscosity $\upsilon = 0$. According to the relation of circulation Γ and vorticity $\vec{\omega}$, the circulation can be defined as flux of voriticity through a specific surface, given by Equation 4.3. In the current 2D case, Γ is the vortex circulation in Z direction. With the distribution of circulations, the vorticity field can be obtained.

$$\nabla \cdot \vec{u} = 0 \tag{4.1}$$

$$\frac{\partial \vec{\omega}}{\partial t} + (\vec{u} \cdot \nabla)\vec{\omega} = \upsilon \nabla^2 \vec{\omega} = 0 \tag{4.2}$$

$$\Gamma = \int\int_S \vec{\omega} \cdot d\vec{S} \tag{4.3}$$

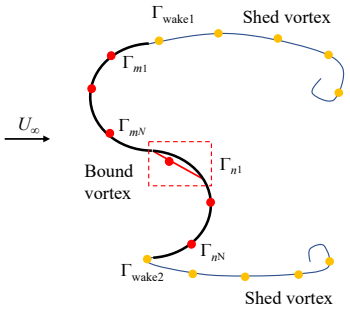

(a) Distribution of vortex particles

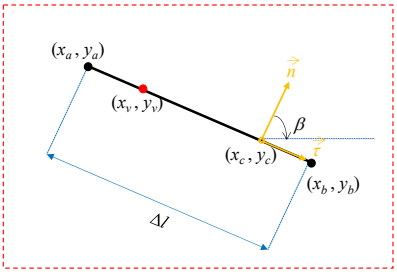

(b) Nomenclature of vortex element

Figure 4.2: Schematic of bound and shed vortex particles

A brief introduction to VPM is also given in this section, emphasising the specific details for the Savonius rotor. Interested readers may refer to *Low Speed Aerodynamics*[8] for extensive information. The distribution of vortex particles and the nomenclature of the Savonius rotor are depicted in Figure 4.2. A vortex element consists of end points (x_a, y_a) and (x_b, y_b), bound vortex point (x_v, y_v) at one-quarter chord from (x_a, y_a), and control point (x_c, y_c) at three-quarter chord from (x_a, y_a). Unit vectors $\vec{n}, \vec{\tau}$ are in the directions normal and tangential to the surface of the vortex element. β is the angle between element's normal and inflow directions. Δl is the vortex element's length. Γ_m, Γ_n represent bound vortex circulations of Blade 1 and Blade 2, respectively. Γ_{wake} is the latest shed vortex circulation.

To predict vortex characteristics, various vortex core models are compared in Section 4.3.2. Taking example of Vatistas model with order of 2 [9], the vortex-induced velocities in tangential and normal directions u, v by vortex point (x_v, y_v) are obtained in Equation 4.4 and Equation 4.5, where r_c is the vortex core radius.

$$u = \frac{\Gamma}{2\pi} \frac{y_c - y_v}{\sqrt{((x_c - x_v)^2 + (y_c - y_v)^2)^2 + r_c^4}} \tag{4.4}$$

$$v = \frac{\Gamma}{2\pi} \frac{-(x_c - x_v)}{\sqrt{((x_c - x_v)^2 + (y_c - y_v)^2)^2 + r_c^4}} \tag{4.5}$$

The Neumann boundary condition should be satisfied at each control point as the fluid cannot go through a surface. By substituting the normal vortex-induced velocity at control point 1 into the Neumann boundary condition, Equation 4.6 is obtained with unknown circulations (Γ_{m_1}-Γ_{m_N}, Γ_{n_1}-Γ_{n_N}, Γ_{wake2}, Γ_{wake1}).

$$\begin{aligned} &a_{m_1 m_1}\Gamma_{m_1} + \cdots + a_{m_1 m_N}\Gamma_{m_N} + a_{m_1 n_1}\Gamma_{n_1} + \cdots + a_{m_1 n_N}\Gamma_{n_N} + \\ &a_{m_1 \text{wake2}}\Gamma_{\text{wake2}} + a_{m_1 \text{wake1}}\Gamma_{\text{wake1}} + (\vec{U}_\infty + \vec{U}_{\text{wake}} + \vec{U}_{\text{rot}}) \cdot \vec{n} = 0 \end{aligned} \tag{4.6}$$

In Equation 4.6, $a_{m_1 j}$ ($j = m_1$-m_N, n_1-n_N, wake1, wake2) is the influence coefficient of the normal velocity component induced by vortex element Γ_j, N is the number of vortex elements for one blade, $\vec{U}_\infty$ is the inflow velocity, $\vec{U}_{\text{wake}}$ is vortex-induced velocity by shed vortices (except the latest shed vortex), $\vec{U}_{\text{rot}}$ is rotational velocity. The last three terms are moved to the right hand side during simulation of VPM, given by $\text{RHS}_{m_1} = -(\vec{U}_\infty + \vec{U}_{\text{wake}} + \vec{U}_{\text{rot}}) \cdot \vec{n}$. Besides Neumann boundary condition, Kelvin condition also serves for the VPM because the time rate of circulation change in a closed curve should be conserved as zero, see Equation 4.7. In this equation, $\Gamma_{\text{b},t}, \Gamma_{\text{b},t-\Delta t}$ represent the sum of bound vortex circulations at current time t and previous time $t - \Delta t$.

$$\Gamma_{\text{b},t} + \Gamma_{\text{wake}} = \Gamma_{\text{b},t-\Delta t} \tag{4.7}$$

Assuming the bound and shed vortex elements' locations are known, the circulations' distribution is numerically solved and henceforth applied to aerodynamic computations. Meanwhile, a time stepping procedure is implemented in VPM, ensuring Kelvin condition and the Neumann boundary condition are satisfied at each time step.

However, the locations of leading and trailing edges of the rotating Savonius are ambiguous in VPM, since the two semicircular blades alternate during rotation. A self-correction technique is proposed by enabling two trailing edges at rotor tips in Section 4.2.2.

4.2.2. DTVPM FOR SAVONIUS

Each semicircular blade is discretized into N elements along the camber, representing the 2D Savonius in VPM. As shown in Figure 4.1, the two blades connect at the rotor center, resulting in two types of profile in Figure 4.3. In Figure 4.3a, the two blade tips are considered as a leading edge (LE) and a trailing edge (TE) in VPM. Control point and vortex point are distributed at the three-quarter and one-quarter of each vortex element, resulting in a fact that the relative position of control point vortices and the blade tip at $\theta = 0°$ is different from the relative position of control point vortices and the blade tip at $\theta = 180°$. According to the expression of normal vortex-induced velocity in Equation 4.5, any change of vortex points distribution will affect the influence coefficient at the control point. This asymmetrical rotation will cause inequivalent influence coefficient and henceforth unbalanced force variations. Therefore, a symmetrical distribution is applied to avoid asymmetrical issues in Figure 4.3b, where two TEs are considered in the simulation of VPM, namely DTVPM. The influence coefficient from shed vortices will stay equivalent in the first and second 180° rotations. The results of two rotor profiles will be discussed in Section 3.3.

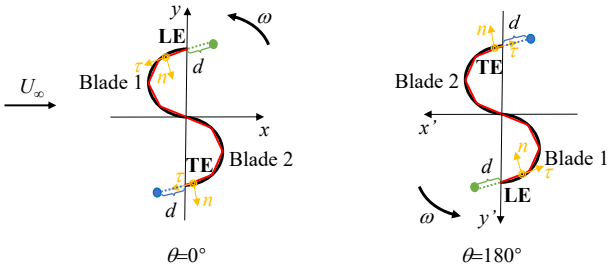

(a) Asymmetrical rotation

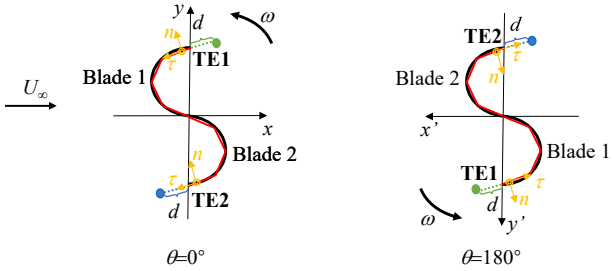

(b) Symmetrical rotation

Figure 4.3: Two types of rotor profile

4.2.3. VISCOUS CORRECTION FOR TIP VORTICES

To accurately predict the blade forces of the Savonius, the viscous effects are included in this section. In this section, differences between viscous and inviscid flow physics from DTVPM are presented for a high-TSR case. The latest shed vortex is assumed to be located at a certain distance d from the blade tip, shown in Figure 4.3b. The distance is calculated by inflow velocity decomposed in the tangential direction of the closest vortex element $U_{\infty,\tau}$ and time step size Δt in Equation 4.8, where constant f is chosen between 0.1 and 0.3.

$$d = f U_{\infty,\tau} \Delta t \tag{4.8}$$

The latest shedding vortices play a key role in simulating flow features and predicting aerodynamic forces of the Savonius rotor. For low TSR, the vortex displacement $\vec{x}$ is commonly determined by local velocity [8] without considerations of viscosity, see Equation 4.9. While for high TSR, the effect of viscosity cannot be neglected, especially near the blade surface. So, Equation 4.10 is applied to the near-wake region to correct tip vortex locations.

$$\frac{\mathrm{d}\vec{x}}{\mathrm{d}t} = \vec{u}_1(\vec{x}, t, \Gamma) \tag{4.9}$$

$$\frac{\mathrm{d}\vec{x}}{\mathrm{d}t} = \vec{u}_1(\vec{x}, t, \Gamma) + \vec{u}_2(\lambda, \vec{x}_{\mathrm{TE}}) \tag{4.10}$$

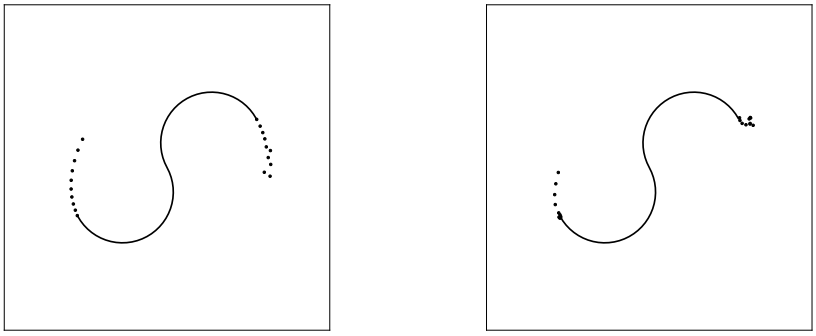

(a) Without viscous correction

(b) With viscous correction

Figure 4.4: Tip vortex trajectory for $\lambda = 1.2$

In the current work, the velocity in Equation 4.10 is applied to the latest $5 \cdot \lambda$ (round to the closest integer) shed vortices (also called tip vortices) and they are relocated according to TSRs. The velocity in Equation 4.10 is applied to the latest vortices. Taking an example of $\lambda = 1.2$, the vortex trajectory without viscous correction is shown in Figure 4.4a, where the latest few particles follow the path of blade tips rotation. However, the flow pattern is quite different with viscous correction as shown in Figure 4.4b. The modified vortex trajectory could capture the typical flow structure, resulting in reasonable predictions of blade forces. Further comparisons can be found in Section 4.3.3.

4.2.4. AERODYNAMIC CALCULATIONS

According to the unsteady Bernoulli's equation, the pressure difference Δp of the surface is obtained from Equation 4.11.

$$\Delta p_j = \rho((U_\infty + u_{\text{vortex}}, v_{\text{vortex}})\vec{\tau}_j \frac{\Gamma_j}{\Delta l_j} + \vec{u}_{\text{rot}}\vec{\tau}_j \frac{\Gamma_j}{\Delta l_j} + \frac{\partial}{\partial t}\sum_{k=1}^{j}\Gamma_k) \tag{4.11}$$

The normal force F_n on the surface is obtained by integrating the pressure difference (per unit length) over the surface in Equation 4.12, including circulatory, kinematics, and added-mass effects.

$$F_n = \int_0^c \Delta p_j dc \tag{4.12}$$

In addition to the normal force, there is a leading-edge suction force acting on the surface, given by Blasius formula [8]. For a flat plate, the suction force (tangential force) pointing from leading edge to trailing edge is given by $\rho\pi c U_\infty^2 A_0^2$, where A_0 is Fourier coefficient, c is the chord length. In Figure 4.3b, the Savonius rotor is discretized into several vortex elements. If we consider each element as a flat plate, the suction force per unit length $F_{s,j}$ can be given by Equation 4.13. The torque Q on the Savonius rotor is calculated by forces and the force arm d_j in the form of Equation 4.14. The torque coefficient c_q is evaluated by dividing the torque with $\frac{1}{2}\rho U_\infty^2 DR$ in Equation 4.15, where D and R are rotor diameter and radius, respectively. The power coefficient c_p is given by Equation 4.16, where $\lambda = \frac{\Omega R}{U_\infty}$. Ω represents rotational speed.

$$F_{s,j} = \rho\pi\Delta l_j U_\infty^2 A_0^2 \tag{4.13}$$

$$Q = \sum_{j=1}^{2N}(F_{n,j}\cdot\vec{n}_j d_j + F_{s,j}\cdot\vec{\tau}_j d_j)\cdot\vec{e}_{\text{rot}} \tag{4.14}$$

$$c_q = \frac{Q}{\frac{1}{2}\rho U_\infty^2 DR} \tag{4.15}$$

$$c_p = c_q \cdot \lambda \tag{4.16}$$

4.2.5. DTVPM

The Savonius rotor's geometry and its motion kinematics are used as input in the simulation of DTVPM. The overall numerical procedure of DTVPM is depicted in Figure 4.5. As mentioned in Section 4.2.2, vortex-induced velocity is affected by the location of trailing edges. DTVPM is implemented to ensure equivalent influence coefficient and periodic force predictions. Once the distribution of vortices is determined, a linear system of equations can be built in Equation 4.17, representing the Neumann boundary condition (first $2N$ rows) and Kelvin theorem (last two rows). The wake shape is updated by a time stepping method [8]. In the simulation of DTVPM, viscous effects are corrected near blade tips.

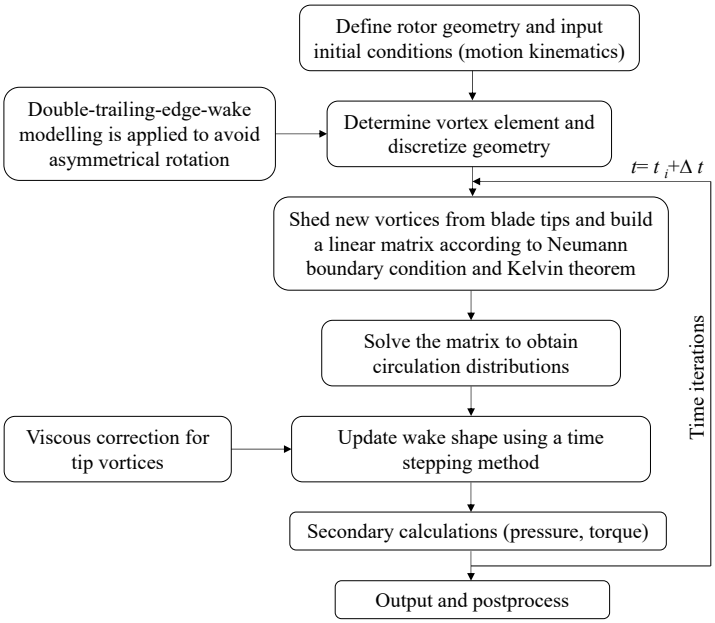

Figure 4.5: Flow chart of DTVPM

$$\begin{pmatrix} a_{m_1m_1} & \cdots & a_{m_1m_N} & a_{m_1n_1} & \cdots & a_{m_1n_N} & a_{m_1\mathrm{TE}2} & a_{m_1\mathrm{TE}1} \\ \vdots & \ddots & \vdots & \vdots & \ddots & \vdots & \vdots & \vdots \\ a_{m_Nm_1} & \cdots & a_{m_Nm_N} & a_{m_Nn_1} & \cdots & a_{m_Nn_N} & a_{m_N\mathrm{TE}2} & a_{m_N\mathrm{TE}1} \\ a_{n_1m_1} & \cdots & a_{n_1m_N} & a_{n_1n_1} & \cdots & a_{n_1n_N} & a_{n_1\mathrm{TE}2} & a_{n_1\mathrm{TE}1} \\ \vdots & \ddots & \vdots & \vdots & \ddots & \vdots & \vdots & \vdots \\ a_{n_Nm_1} & \cdots & a_{n_Nm_N} & a_{n_Nn_1} & \cdots & a_{n_Nn_N} & a_{n_N\mathrm{TE}2} & a_{n_N\mathrm{TE}1} \\ 1 & \cdots & 1 & 0 & \cdots & 0 & 0 & 1 \\ 0 & \cdots & 0 & 1 & \cdots & 1 & 1 & 0 \end{pmatrix} \begin{pmatrix} \Gamma_{m_1} \\ \vdots \\ \Gamma_{m_N} \\ \Gamma_{n_1} \\ \vdots \\ \Gamma_{n_N} \\ \Gamma_{\mathrm{TE}2} \\ \Gamma_{\mathrm{TE}1} \end{pmatrix} = \begin{pmatrix} \mathrm{RHS}_{m_1} \\ \vdots \\ \mathrm{RHS}_{m_N} \\ \mathrm{RHS}_{n_1} \\ \vdots \\ \mathrm{RHS}_{n_N} \\ \Gamma_{b_1(t-\Delta t)} \\ \Gamma_{b_2(t-\Delta t)} \end{pmatrix} \tag{4.17}$$

4.2.6. NUMERICAL AND EXPERIMENTAL DETAILS

In this work, the URANS simulation is conducted in OpenFOAM to validate the proposed DTVPM. In OpenFOAM, the simulated Savonius rotor has the same geometry as in DTVPM, but with thickness of $0.001D$. Tip speed ratios of 0.2-1.2 are employed with inflow velocity of 7m/s. Although the Savonius rotor operates in a confined flow, its power performance and forces are insensitive to blockage effects when separated flow is presented [10, 11]. As reported in literature [11], turbines operating with blockage ratio of 10%-60% (larger than 6.67% in current work) at $\lambda = 1.4$ have a similar power performance and forces. The computational domain with blockage ratio of 6.67% is shown in Figure 4.7. The rotating axis is located at a distance of $15R$ from the inlet boundary. The whole domain is divided into the rotational and the stationary subdomains. The transfer of field variables across the domains is achieved through an arbitrary mesh interface (AMI). This study is based on URANS approach, in which SST $k-\omega$ turbulence model is employed to simulate the incompressible, viscous transient flow. A second-order upwind scheme is used for the spatial discretization of the momentum equations in the simulations. The first row's cell height of the outer boundary layer is $0.0102\%R$, calculated based on $y^+ = 1.0$. The angle interval (angle step size) for $\lambda = 0.2$-1.2 is chosen as 0.24°.

The experiments were conducted in the Vought Systems Division 4.9m×6.1m Low Speed Wind Tunnel [12] to evaluate aerodynamic performance of a Savonius rotor. The presented results are power and torque coefficients as a function of tip speed ratio. Different parameters were studied in this experiment, including number of blades (2 and 3), gap width (0-0.1m), and rotor height (1m and 1.5m). The diameter of each blade is 0.5m. All configurations were tested at inflow velocities of 7m/s and 14m/s, respectively. A schematic of the Savonius rotor, instrumentation, load and control system is shown in Figure 4.6.

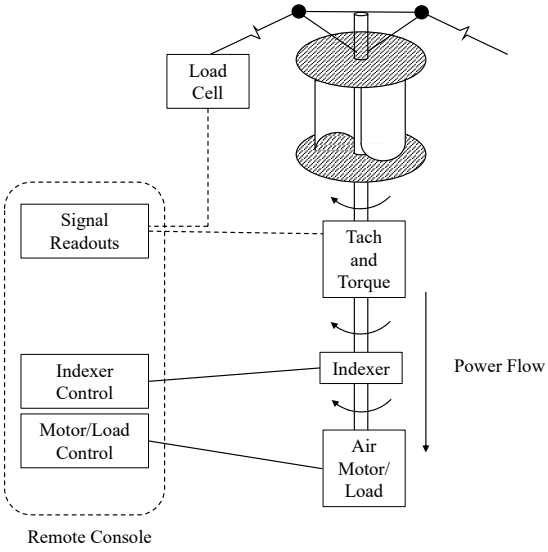

Figure 4.6: Schematic of the Savonius rotor/instrumentation load system [12]

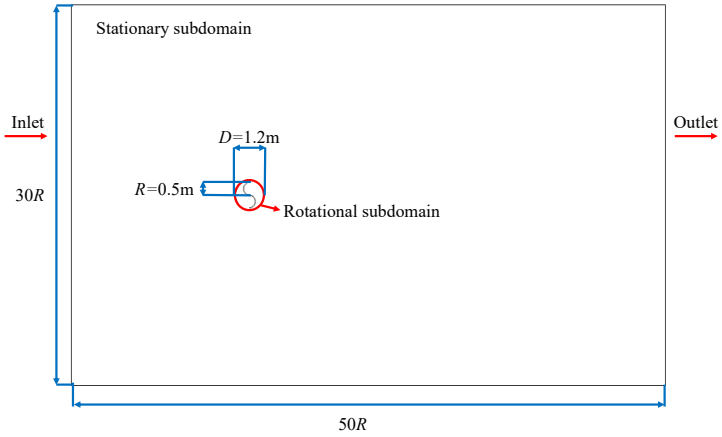

(a) Computational domain

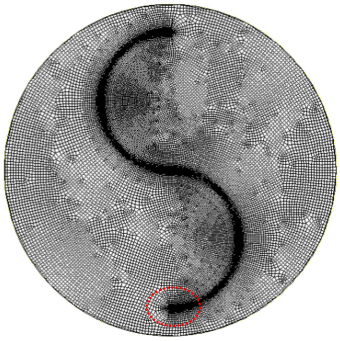

(b) Rotational subdomain

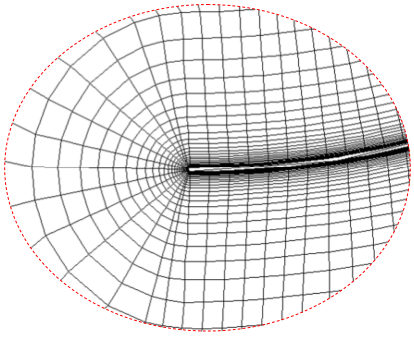

(c) Structured grid around the rotor

Figure 4.7: Computational domain and mesh for Eulerian URANS simulation in OpenFOAM

4.3. RESULTS AND DISCUSSIONS

4.3.1. VALIDATION AGAINST URANS AND EXPERIMENTS

The power coefficients c_p versus λ from Eulerian URANS model, experiment, Lagrangian DTVPM with and without viscous corrections are depicted in Figure 4.8. The variation trend of c_p increases from $\lambda = 0.2$ to $\lambda = 0.8$ and decreases from $\lambda = 0.8$ to $\lambda = 1.2$ in the three simulation methods, which is comparable with experimental results [12] for all TSRs. The maximum power output occurs at $\lambda \approx 0.8$. However, DTVPM without viscous correction underestimates c_p when $\lambda > 0.8$. Despite discrepancies of DTVPM without viscous correction, power coefficients from DTVPM with viscous correction, Eulerian URANS model and experiment are in a reasonable agreement. To validate the simulation of DTVPM, detailed results of DTVPM are compared with URANS simulations in the following sections.

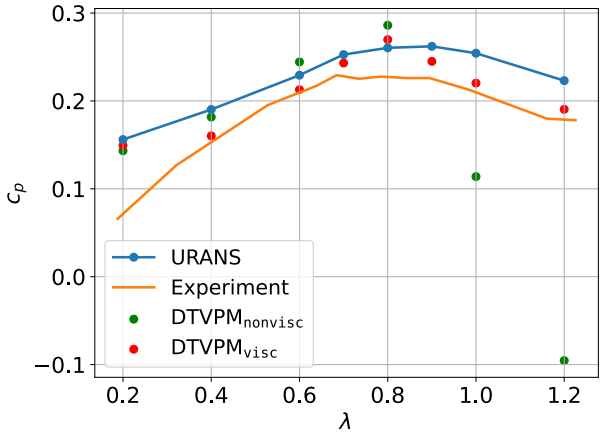

Figure 4.8: Power coefficient for different TSRs

Table 4.1: Deviations of simulations for power coefficients at different TSRs

Δc_p	$\lambda = 0.2$	$\lambda = 0.4$	$\lambda = 0.6$	$\lambda = 0.8$	$\lambda = 1.0$	$\lambda = 1.2$	Standard deviation σ
URANS	0.08	0.04	0.02	0.03	0.04	0.04	0.02
DTVPM$_{\text{nonvisc}}$	0.07	0.03	0.03	0.06	-0.10	-0.27	0.12
DTVPM$_{\text{visc}}$	0.08	0.01	0.00	0.04	0.01	0.01	0.02

In Figure 4.8, the difference between the two methods DTVPM with and without viscous corrections can be attributed to the potential flow assumption of the conventional vortex particle method.

In order to quantify the validation results of power coefficient, deviations of simulations for power coefficients at different TSRs are presented in Table 4.1. Δc_p is the difference between numerical and experimental results. It is observed that URANS and DTVPM with viscous correction predict more stable results for varied tip speed ratio with a standard deviation of 0.02. With the premise of stable prediction, URANS and DTVPM with viscous correction are prior to DTVPM without viscous correction. Among the two simulations of DTVPM, the viscous correction tends to predict more accurate c_p with Δc_p=0.01 for λ=1.0, 1.2.

4.3.2. SENSITIVITY ANALYSIS AND CONVERGENCE STUDY

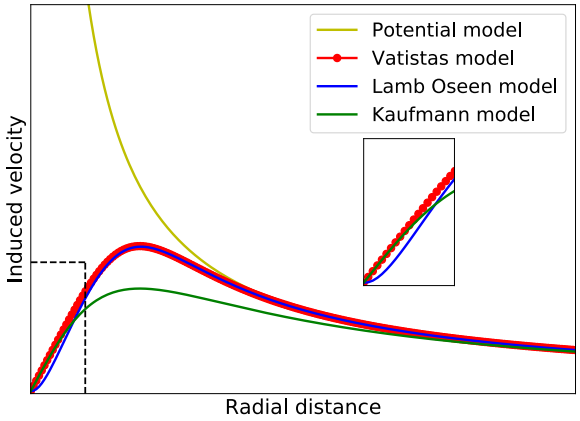

Figure 4.9: Vortex-induced velocity distribution of various vortex core models

For a rotating Savonius, a proper vortex core model has a significant effect on vortex interactions. Among all available vortex core models, a common approach for the vortex induced velocity $\vec{V}$ is using a desingularized algebraic profile with a constant vortex core size or a diffusive core growth with time. Hald [13] has proved that adjacent vortices distancing is a key parameter for the convergence of the vortex method. Hence, the vortex core radius needs to be compared and selected for the simulation of DTVPM. Kaufmann [14], Vatistas [9], and Lamb Oseen [15, 16] models commonly overcome the singular nature of potential vortex. Kaufmann [14] model reduces the maximum induced velocity in the form of Equation 4.18. Vatistas [9] proposed a family of disingularized vortex core model with $n = 1,2,3...$, expressed as Equation 4.19. Lamb Oseen model [15, 16] is developed to approximate the viscous core structure by taking the diffusion effect into account, expressed as Equation 4.20. r_{c0} is initial core radius at the origin of vortex. By differentiating Equation 4.20 concerning radial distance $\vec{r}$ and setting the derivative as zero, the viscous vortex core radius r_c is then obtained to grow with time as Equation

4.21, where the Oseen parameter $\sigma = 1.25643$ [17].

$$\vec{V} = \frac{1}{2\pi} \frac{\vec{r}}{\vec{r}^2 + r_c^2} \times \vec{e}_Z \Gamma \tag{4.18}$$

$$\vec{V} = \frac{1}{2\pi} \frac{\vec{r}}{(\vec{r}^{2n} + r_c^{2n})^{1/n}} \times \vec{e}_Z \Gamma \qquad (n = 1, 2, 3...) \tag{4.19}$$

$$\vec{V} = \frac{1}{2\pi \vec{r}} (1 - e^{-\frac{\vec{r}^2}{4\upsilon t + r_{c0}^2}}) \times \vec{e}_Z \Gamma \tag{4.20}$$

$$r_c(t) = \sqrt{4\sigma\upsilon t + r_{c0}^2} \tag{4.21}$$

Figure 4.9 shows the induced velocity distributions on the basis of various vortex models. As Kaufmann model tends to underestimate induced velocities, Vatistas with $n = 2$ and Lamb Oseen models have a similar trend except the vortex origin. As shown in the detail of Figure 4.9, Lamb Oseen model shows a smoother variation from the vortex origin to a finite radial distance than Vatistas model. The two models are further investigated and evaluated based on the downstream velocity, particle map, and torque coefficient. Vatistas model with $r_c = 0.012, 0.022, 0.032$m and Lamb Oseen model with $r_{c0} = 0, 0.005, 0.01, 0.015$m are employed. Figure 4.10 shows comparisons of downstream velocity for Vatistas and Lamb Oseen models at $\lambda = 0.8$. As shown in Figure 4.10a and Figure 4.10c, two vortex core models predict a similar velocity distribution in the near-wake region $x/R = 2$. $\Delta(U/U_\infty)$ is the difference between DTVPM and URANS. Vatistas model with $r_c = 0.012$m has a maximum $\Delta(U/U_\infty)$ of 0.43 (0.65 while $r_c = 0.022$m) with a standard deviation of 0.08 (0.15 while $r_c = 0.022$m) at $x/R = 2$. In the far-wake region $x/R = 18$ of Figure 4.10b and Figure 4.10d, Vatistas model with $r_c = 0.012$m differs from URANS in a maximum $\Delta(U/U_\infty)$ of 0.12 (0.26 while $r_c = 0.022$m) with a standard deviation of 0.03 (0.06 while $r_c = 0.022$m). The maximum $\Delta(U/U_\infty)$ predicted by Lamb Oseen model differs from URANS by at least 0.37 with a standard deviation of 0.09 at $x/R = 2$, and at least 0.22 with a standard deviation of 0.05 at $x/R = 18$. To obtain a better prediction of downstream velocity fields, Vatistas model with $r_c = 0.012$m is suggested when $\lambda = 0.8$.

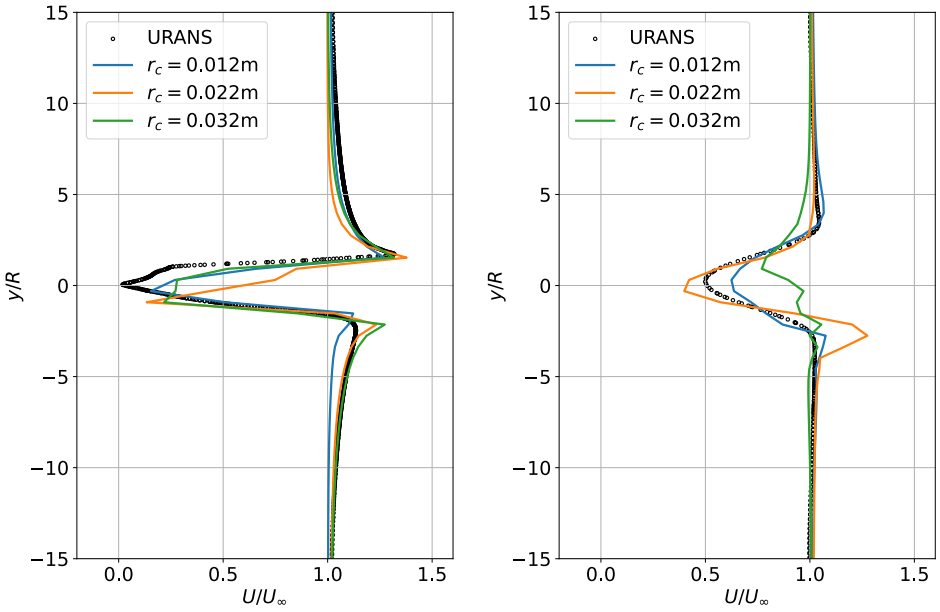

(a) Vatistas, $x/R = 2$

(b) Vatistas, $x/R = 18$

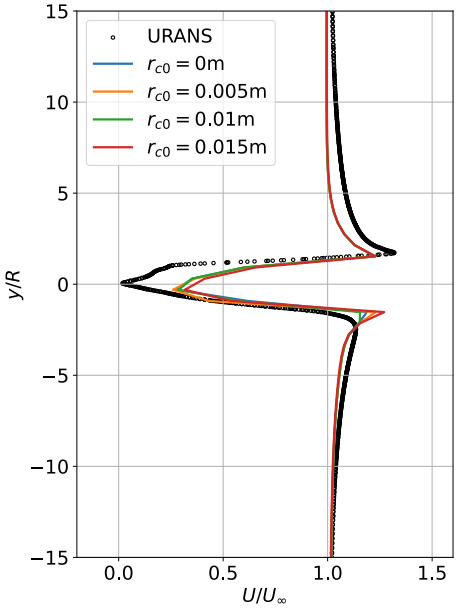

(c) Lamb Oseen, $x/R = 2$

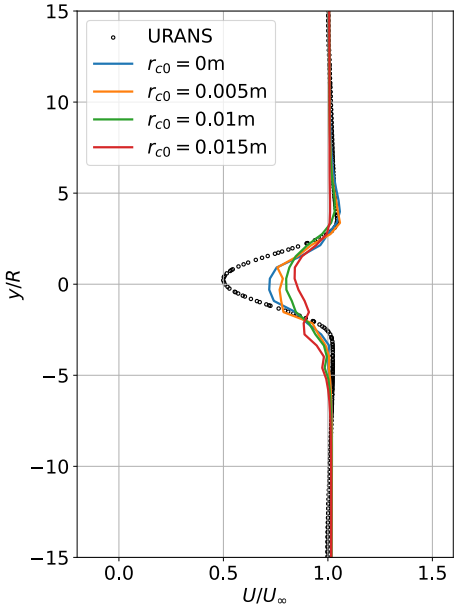

(d) Lamb Oseen, $x/R = 18$

Figure 4.10: Sample downstream velocity curve for two vortex core models, $\lambda = 0.8$

Figure 4.11 and Figure 4.12 present the effect of vortex core model on the particle map and torque coefficient c_q, respectively. It is observed that the vortex blobs are located at similar positions in the Lamb Oseen and Vatistas models. Additionally, both models estimate the periodic variation of the torque acting on the rotor with the largest $c_q \approx 1.0$. Table 4.2 lists power coefficients from different vortex core models and URANS. Vortex core radius of 0.024m predicts a more comparable c_p with URANS. Although c_q from Vatistas model slightly fluctuates near $\theta = 30°$, the Vatistas model with $n = 2$ and $r_c = 0.024$m is suggested for $\lambda = 0.8$ considering the wake profile and power performance predicted by the two vortex core models.

The power performances are further investigated in three different inflow conditions using DTVPM with viscous correction. Lamb Oseen [15, 16] model is employed due to its viscous term. The inflow conditions are characterized by three Reynolds numbers: $Re \approx$2.86e5, 5.85e5 and 1.14e6. Figure 4.13 shows power coefficient c_p as a function of tip speed ratio (TSR) for Savonius rotor with various Reynolds numbers. It is observed that increasing Reynolds number appears to slightly increase c_p for majority TSRs. The dependence of Reynolds number has also been reported in Ref. [12, 18], and it is resulted from a delay of flow separation on the convex side of the rotor for a high Reynolds number.

(a) Lamb Oseen

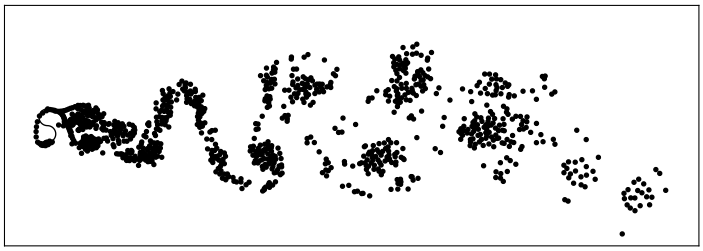

(b) Vatistas

Figure 4.11: Effect of vortex core model on the particle map, $\lambda = 0.8$

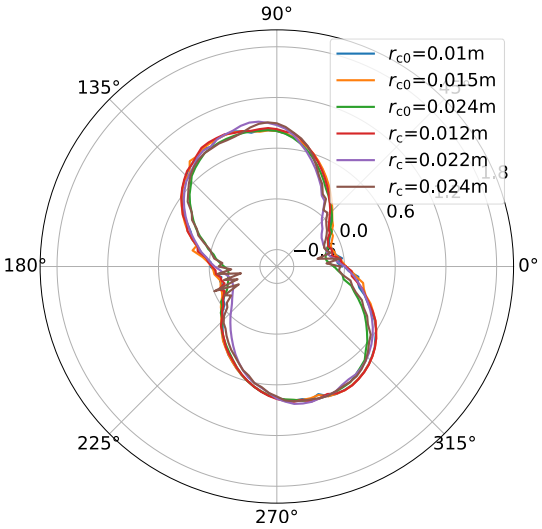

Figure 4.12: Effect of vortex core model on the torque coefficient c_q, $\lambda = 0.8$, Lamb Oseen: r_{c0}, Vatistas: r_c

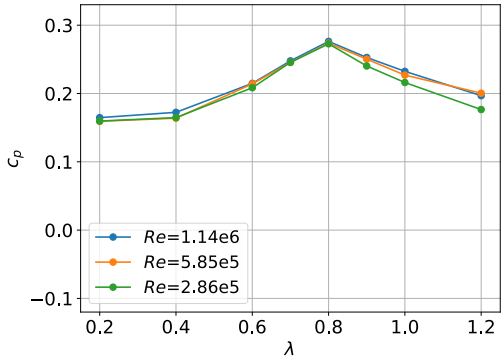

Figure 4.13: Power coefficient of Savonius rotor with different Reynolds numbers

Table 4.2: Power coefficients from different vortex core models and URANS

	Lamb Oseen			Vatistas			URANS
r_c [m]	0.01	0.015	0.024	0.012	0.022	0.024	-
c_p	0.318	0.328	0.274	0.321	0.281	0.270	0.260

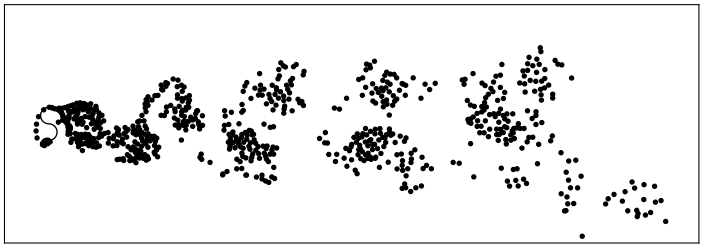

(a) $\Delta\theta = 4.76°$

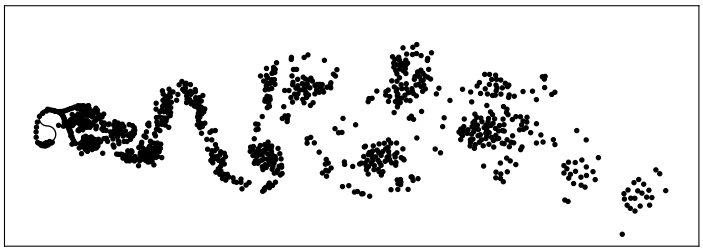

(b) $\Delta\theta = 3.6°$

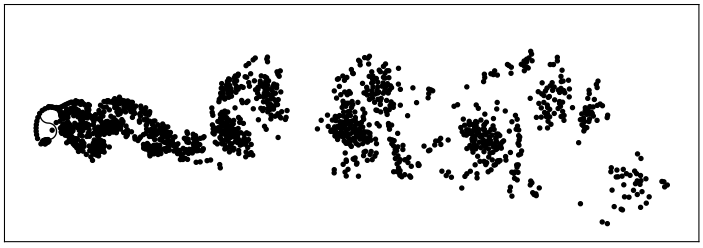

(c) $\Delta\theta = 2.44°$

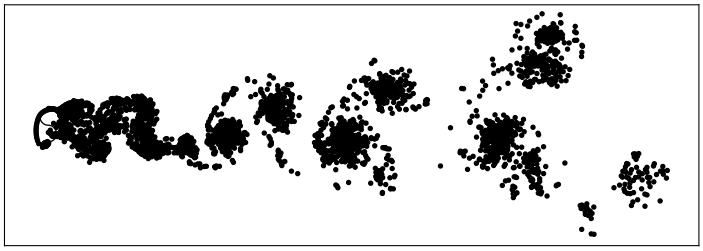

(d) $\Delta\theta = 1.28°$

Figure 4.14: Particle maps after the fifth rotation, $\lambda = 0.8$

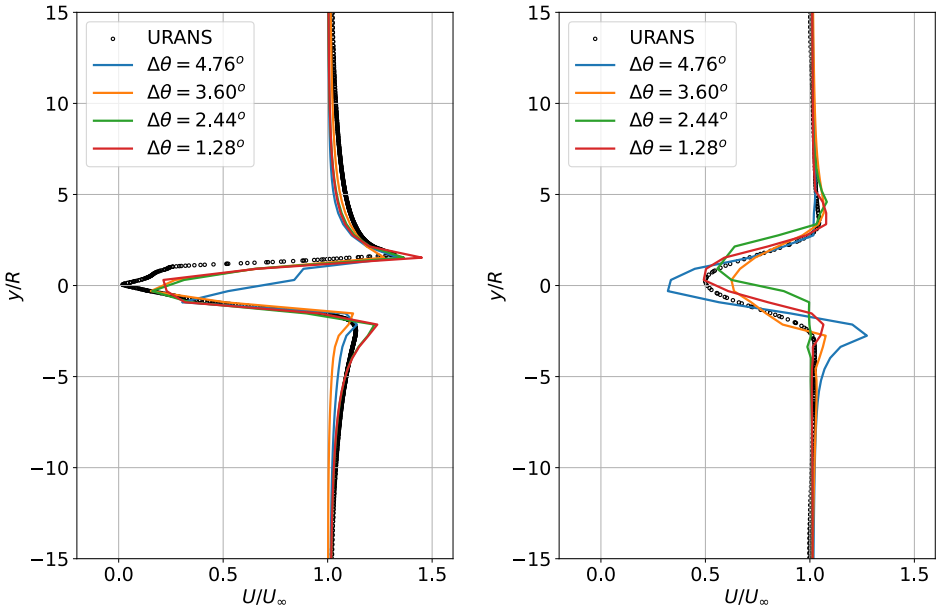

(a) $x/R = 2$ (b) $x/R = 18$

Figure 4.15: Sample downstream velocity curve for different angle intervals, $\lambda = 0.8$

The convergence study is performed based on the angle interval $\Delta\theta$ = 4.76°-1.28°. Their particle maps are shown in Figure 4.14. It is observed that the particle maps are converging to a specific distribution profile as $\Delta\theta$ decreases. To further study the convergence of DTVPM, the velocity variations at downstream are compared with URANS results in Figure 4.15. Four rotations are taken into account for each velocity curve. As observed in Figure 4.15, DTVPM predicts similar variation trends with URANS. In the near-wake region x/R = 2, the nondimensional velocity at $y/R \approx 1.5$ is much higher than that at $y/R \approx -1.5$. The asymmetry velocity variation is well captured by URANS and the four cases of DTVPM. This asymmetry could be consequence of staggered distributed vortex blobs in the x direction. DTVPM with $\Delta\theta$ = 3.60° differs from URANS in a maximum $\Delta(U/U_\infty)$ of 0.43 (same with $\Delta\theta$ = 1.28°) and average $\Delta(U/U_\infty)$ of -0.01 (0.004 while $\Delta\theta$ = 1.28°) with a standard deviation of 0.08 (0.09 while $\Delta\theta$ = 1.28°) along the section of x/R = 2. For x/R = 18, the maximum and average $\Delta(U/U_\infty)$ predicted by DTVPM with $\Delta\theta$ = 3.60° are 0.12 and 0.02 (0.19 and 0.01 while $\Delta\theta$ = 1.28°), respectively. The standard deviation of $\Delta(U/U_\infty)$ is 0.03 (0.05 while $\Delta\theta$ = 1.28°). Even though decreasing $\Delta\theta$ from 3.60° to 1.28° may allow DTVPM to predict a bit more consistent results with URANS, the simulation will be more computationally expensive with smaller $\Delta\theta$. As mentioned above, because DTVPM with $\Delta\theta$ = 3.60° provides acceptable accuracy and computational efficiency, it is selected in the following cases.

4.3.3. EFFECT OF VISCOUS CORRECTION FOR TIP VORTICES

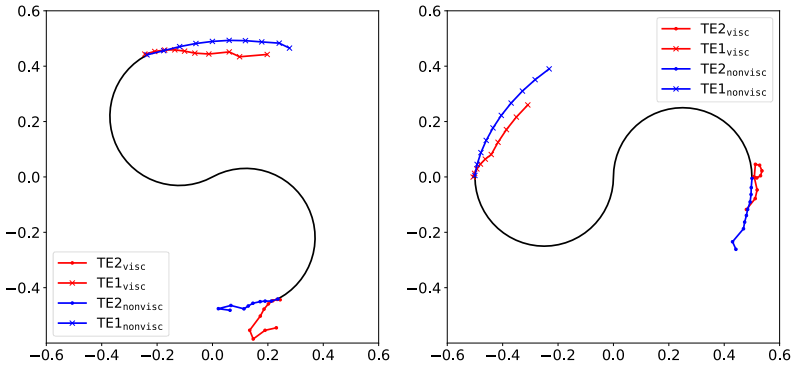

(a) $\theta = 30°$, DTVPM (b) $\theta = 90°$, DTVPM

(c) $\theta = 120°$, DTVPM (d) $\theta = 150°$, DTVPM

Figure 4.16: Latest 10 vortex particle trajectory from DTVPM with and without viscous corrections at $\lambda = 1.2$

This section is to verify the viscous corrections for tip vortices stated in Section 4.3.3. Figure 4.16 and Figure 4.17 depict the inputs and effects of the vortex system corresponding to the optimized DTVPM with viscous correction and original DTVPM without correction for $\lambda = 1.2$. Figure 4.16 presents the vortex particle map at four phase angles. In these maps, the latest 10 vortex particles are displayed, showing notable differences between DTVPM with and without viscous effects near blade tips. In the viscous cases, the vortex particles shedding from trailing edges tend to recirculate back to the rotating directions. The viscous effects on the velocity field are shown in Figure 4.17. It compares the velocity fields from URANS, and DTVPM with and without viscous corrections at phase angle of 30°. The reverse flow mentioned above is also observed in velocity fields from URANS, shown in Figure 4.17a, which is expected in practical since there are significant viscous effects near the rotor. As shown in Figure 4.17b, the reverse flow near the bottom blade tip is well captured by the corrected method. But in Figure 4.17c, this phenomenon is not observed due to lack of roll up vortex particles. So, the viscous correction for tip vortices is required for Savonius rotor with high TSRs.

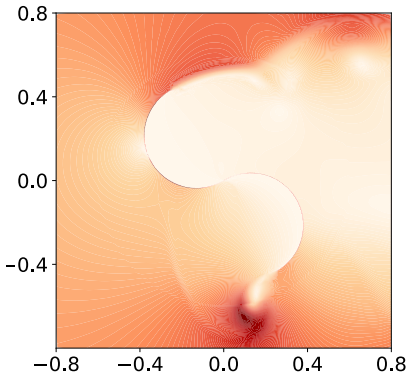

(a) URANS

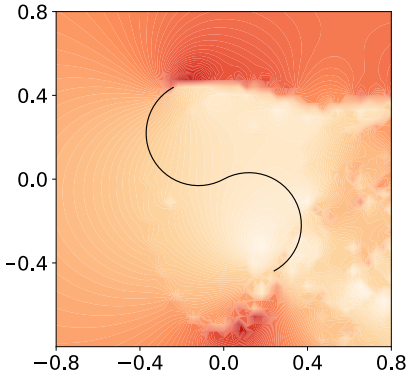

(b) With correction

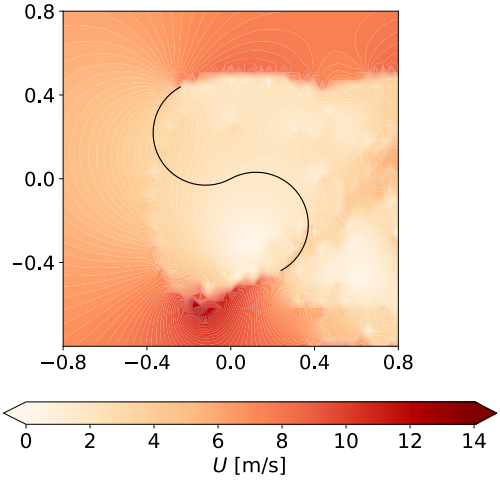

(c) Without correction

Figure 4.17: Velocity field from DTVPM with and without viscous corrections at $\theta = 30°, \lambda = 1.2$

4.3.4. EFFECT OF TSR

Table 4.3: Deviations of three simulations of VPM for torque coefficient over one revolution

Δc_q	Method	$\lambda = 0.2$	$\lambda = 0.4$	$\lambda = 0.6$	$\lambda = 0.8$	$\lambda = 1.0$	$\lambda = 1.2$	Average
Standard deviation σ	VPM	0.20	0.22	0.27	0.26	0.25	0.23	0.24
	$\text{DTVPM}_{\text{nonvisc}}$	0.32	0.14	0.09	0.10	0.10	0.21	0.16
	$\text{DTVPM}_{\text{visc}}$	0.37	0.17	0.14	0.11	0.17	0.24	0.20
Maximum	VPM	0.53	0.63	0.76	0.68	0.74	0.57	0.65
	$\text{DTVPM}_{\text{nonvisc}}$	0.47	0.28	0.20	0.26	0.33	0.83	0.39
	$\text{DTVPM}_{\text{visc}}$	0.57	0.38	0.31	0.25	0.34	0.44	0.38

A comparison of the torque variation from URANS, VPM, and DTVPM with and without viscous effects near blade tips is shown in Figure 4.18. Table 4.3 lists standard deviation and maximum value of Δc_q over one revolution. As discussed in Section 4.2.2, the biggest

difference between VPM and DTVPM is the distributions of TEs. Figure 4.18 shows that DTVPM with and without viscous corrections yield more symmetrical torque predictions than VPM. During the second 180° rotation, VPM tends to overestimate/underestimate the torque on the rotor in a maximum difference of 0.65 with a standard deviation of 0.24, which are higher than the two simulations of DTVPM. Hence, for the simulation of rotating Savonius, it is essential to apply double-trailing-edge-wake-modelling to VPM.

Through comparison between DTVPM with and without viscous corrections in Figure 4.18 and Table 4.3, the proposed viscous corrections for tip vortices will insignificantly affect the accuracy of torque calculations at $\lambda < 1.0$. However, DTVPM without viscous correction at $\lambda = 1.2$ is different from URANS with a maximum difference of 0.83, which is greatly reduced to 0.44 when including viscous correction. The average standard deviations for the three simulations of VPM are 0.24, 0.16 and 0.20. Figure 4.18a depicts a phase shift of about 25° for torque coefficients of DTVPM without/with viscous corrections, resulting in an increase of standard deviation from 0.20 to 0.32/0.37.

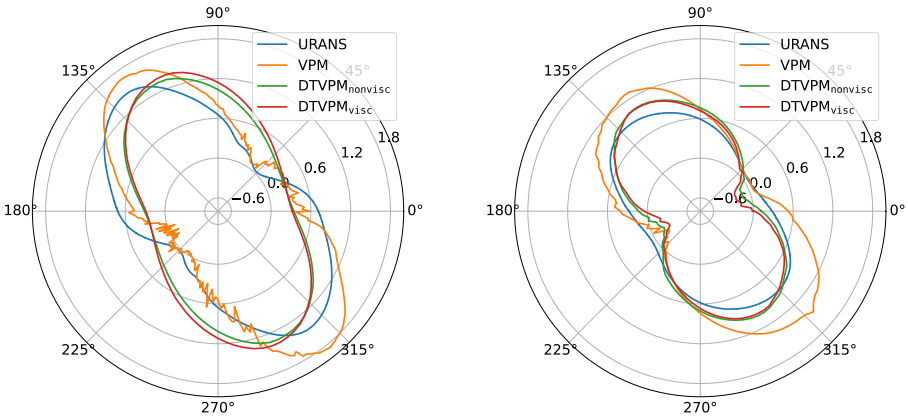

(a) λ=0.2

(b) λ=0.4

(c) λ=0.6

(d) λ=0.8

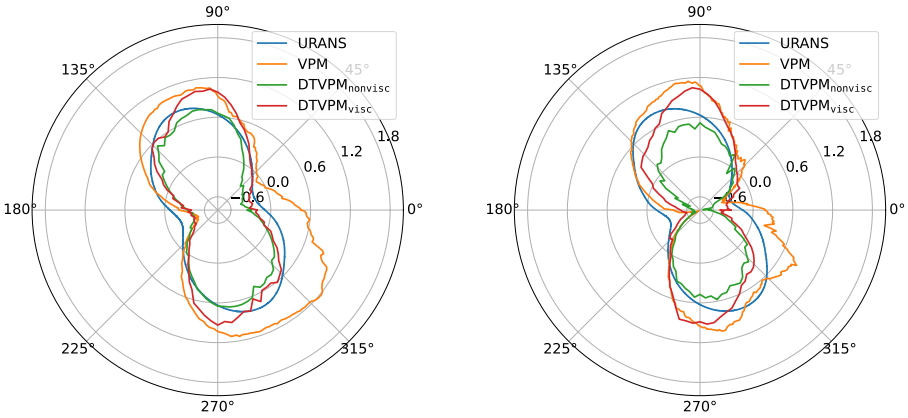

(e) λ=1.0 (f) λ=1.2

Figure 4.18: Torque coefficient over one revolution at different TSRs

4.3.5. EFFECT OF PHASE ANGLE

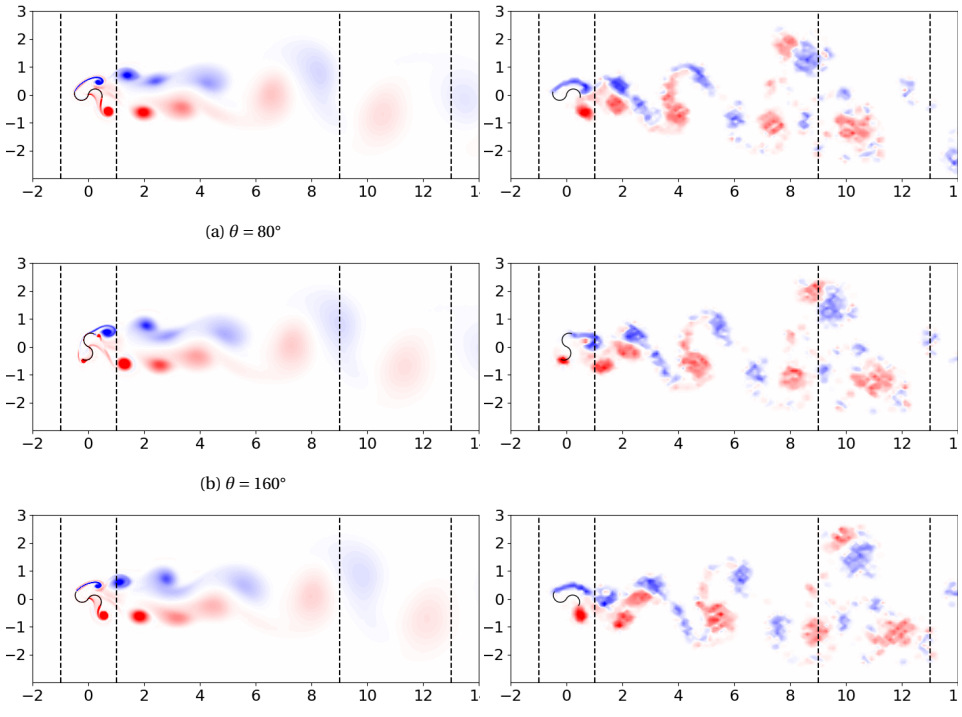

(a) $\theta = 80°$

(b) $\theta = 160°$

(c) $\theta = 240°$

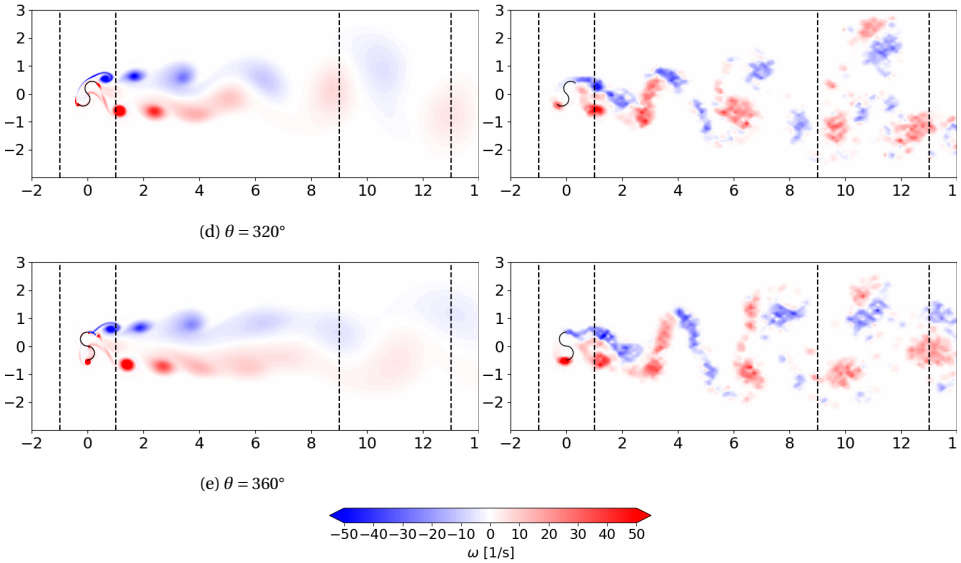

Figure 4.19: Comparison of flow features between URANS (left) and DTVPM with viscous correction (right) over one revolution, $\lambda = 0.8$, coordinate axis: x [m], y [m]

DTVPM can also be utilized to learn flow characteristics behind Savonius rotor in an efficient way. In this section, the influence of the rotor phase angle is investigated by comparing URANS and DTVPM with viscous correction. Figure 4.19 depicts flow features over one revolution at $\lambda = 0.8$ with three downstream locations represented by dashed lines, $x/R = -2, 2, 18, 26$. The observations include:

- Vortex blobs have a staggered and periodic distribution that agrees with Kármán vortex street phenomenon, also appears in literature [19].
- The near-wake region at $0 \leq x/R \leq 2$ is well predicted by DTVPM for vortex positions and velocity magnitude.
- The shedding vortices at far-wake region ($x/R \geq 2$) are found to be deflected with a larger amplitude in the y direction. It could be due to the neglect of viscous effects at downstream, which can be improved by employing particle strength exchange.

The vorticity fields at near-wake region are depicted in Figure 4.20. At $\theta = 160°$, the trailing-edge vorties (TEVs) start to appear at the two blade tips. As the rotor keeps rotating, the sizes of TEVs gradually grow and are large enough to be shed from the blade tips at $\theta = 240°$. Due to the symmetrical feature of rotation, when it rotates at around $\theta = 320°$, a new process of TEV generation and detachment start to alternate in the flow field. Through comparison of vorticity field from URANS and DTVPM, the near-wake flow characteristics are considered to be in good agreement. The concentrated TEV blobs near the rotor are located at roughly the same positions. In addition, TEV generation near the driving blade (left blade in Figure 4.20a) tip causes reverse flow, which contributes to torque generation from $\theta = 80°$ to $\theta = 160°$. TEV detaches from the driving blade (top blade in Figure 4.20b) tip, restricting torque generation from $\theta = 160°$ to $\theta = 240°$.

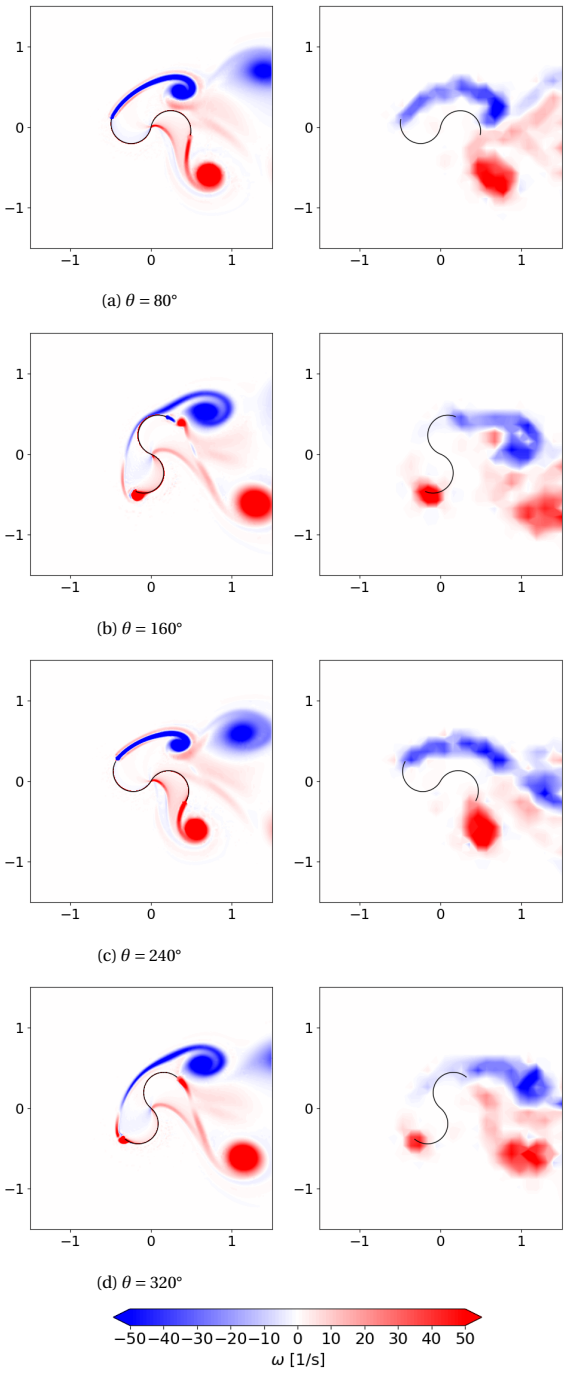

Figure 4.20: Vorticity fields at near-wake region from URANS (left) and DTVPM with viscous correction (right), $\lambda = 0.8$, coordinate axis: x [m], y [m]

To provide a more detailed analysis of the inflow and wake features, velocity curve variations at four downstream positions and five phase angles are presented in Figure 4.21 - Figure 4.24. Figure 4.21 presents velocity curve variations in front of Savonius rotor. For given phase angles, the wake width is well captured by DTVPM. In Figure 4.22, DTVPM and URANS can clearly capture the wake asymmetry. Figures 4.23 and 4.24 show that the wake profile at further downstream is dominated by instabilities of DTVPM, showing larger differences from URANS on the velocity curves. As shown in Figures 4.23d and 4.19d, DTVPM predicted a maximum $\Delta(U/U_\infty)$ of 0.31 with a standard deviation of 0.08 at x/R=18, θ=320° from URANS, which corresponds to the vortex migration at x=9m. Other quantifiable examples are U/U_∞ at x/R=26, θ=80° predicted by DTVPM being no more than 0.25 higher than that predicted by URANS, and U/U_∞ at x/R=26, θ=360° predicted by DTVPM being at most 0.52 higher than that predicted by URANS. Overall, discrepancies of the velocity magnitudes behind the rotor for URANS and DTVPM can be attributed to the limitations of DTVPM modeling in which the turbulence viscosity is absent.

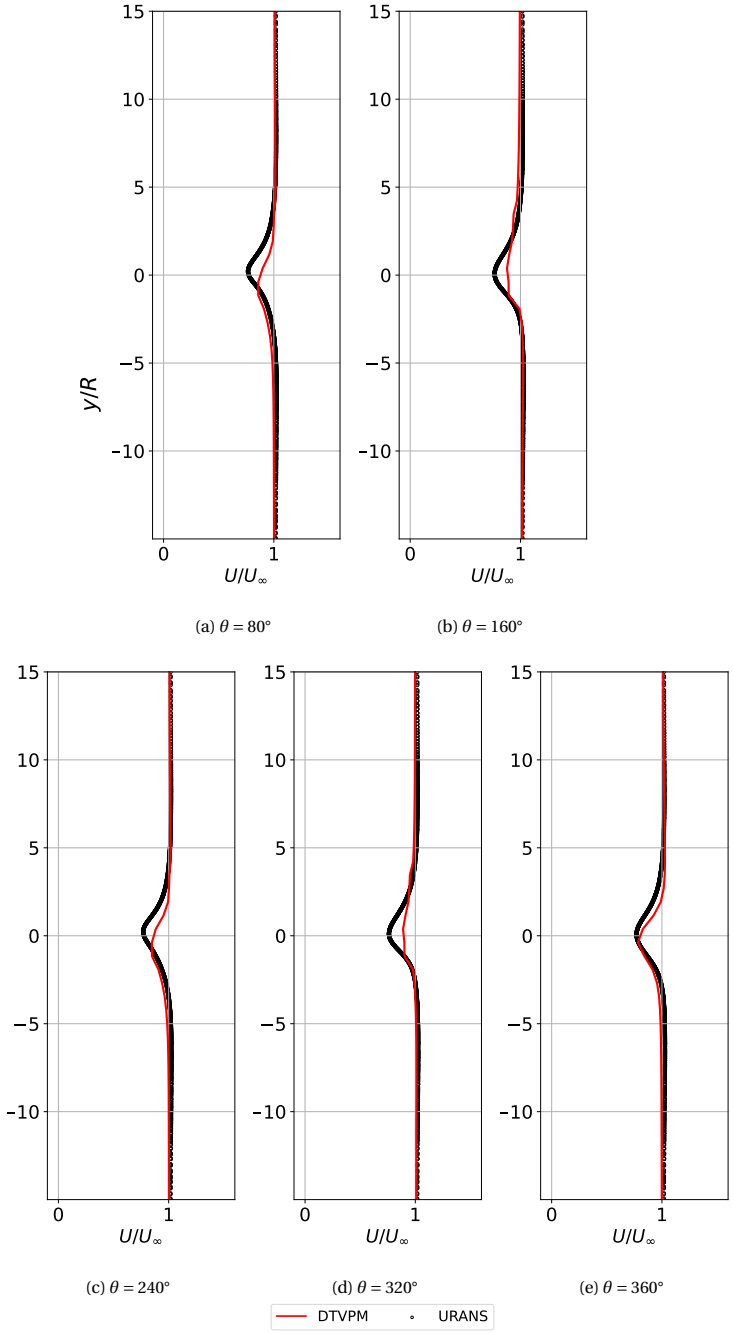

(a) $\theta = 80°$ (b) $\theta = 160°$

(c) $\theta = 240°$ (d) $\theta = 320°$ (e) $\theta = 360°$

Figure 4.21: Velocity curve variations at x/R=-2 over one revolution, $\lambda = 0.8$

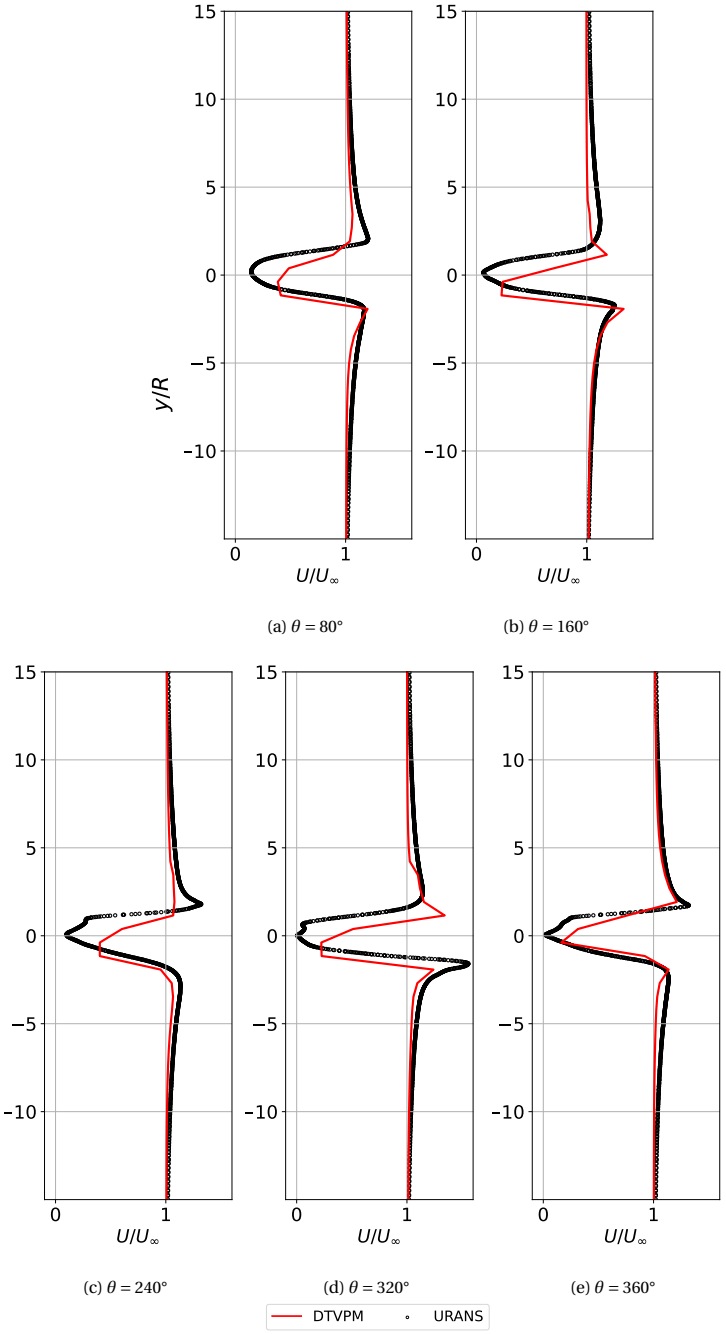

Figure 4.22: Velocity curve variations at x/R=2 over one revolution, $\lambda = 0.8$

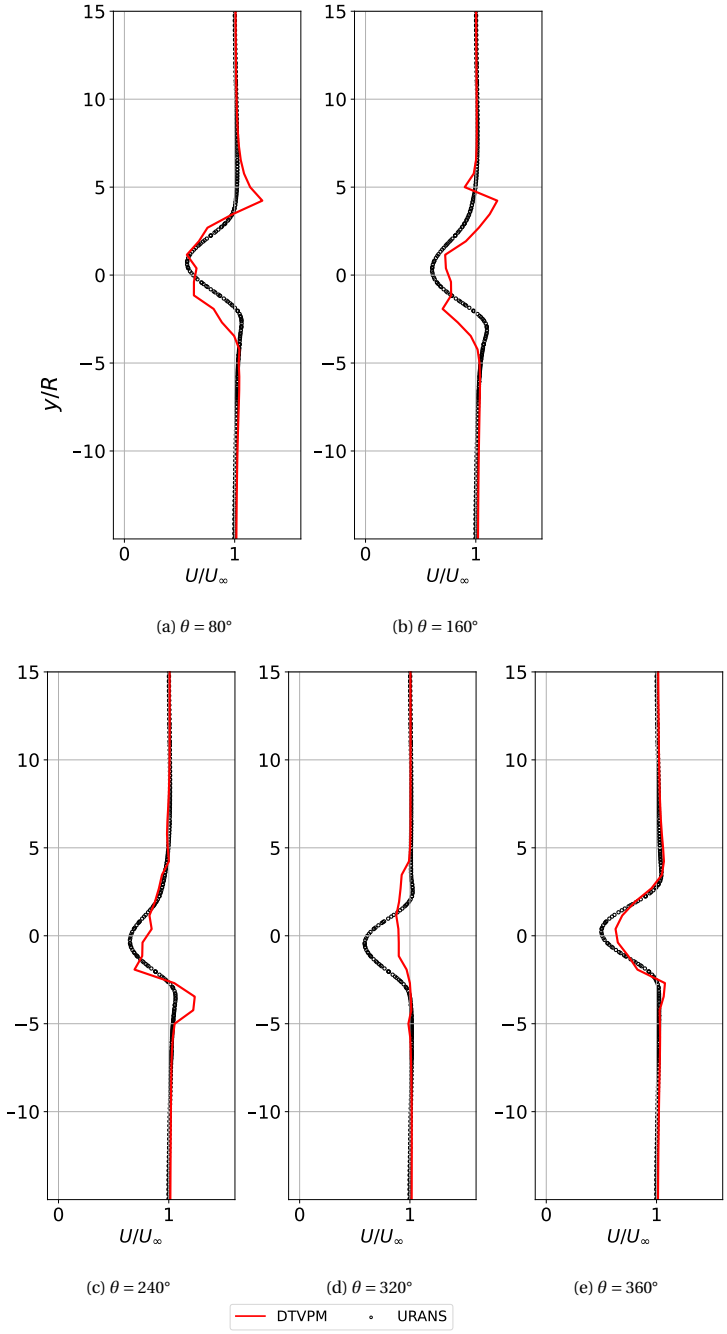

(a) $\theta = 80°$ (b) $\theta = 160°$

(c) $\theta = 240°$ (d) $\theta = 320°$ (e) $\theta = 360°$

Figure 4.23: Velocity curve variations at x/R=18 over one revolution, $\lambda = 0.8$

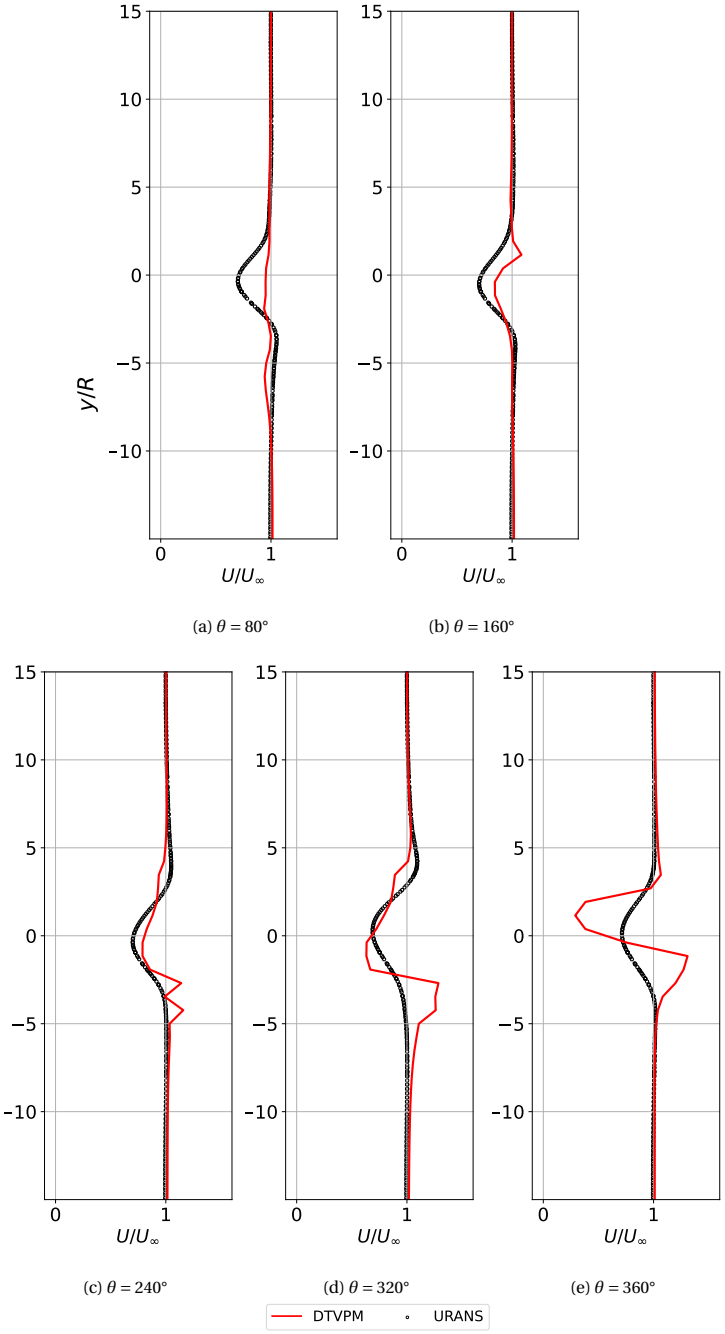

Figure 4.24: Velocity curve variations at x/R=26 over one revolution, $\lambda = 0.8$

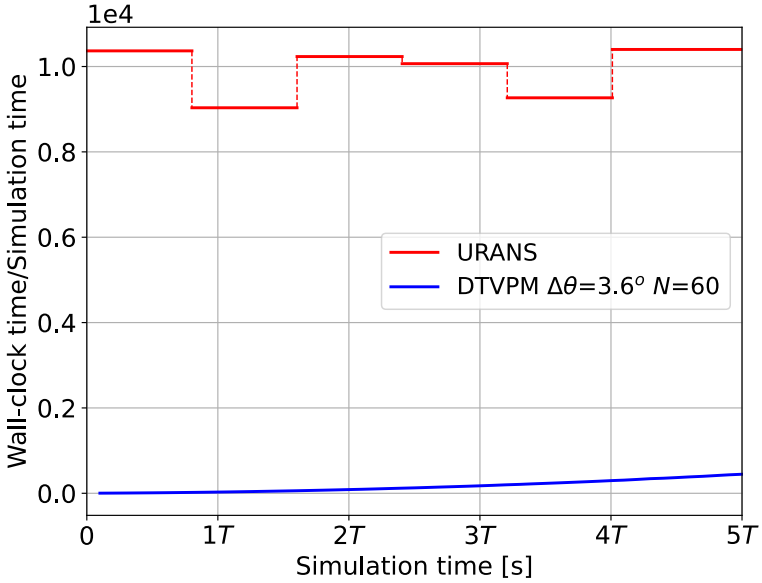

Figure 4.25: Computational efficiency of DTVPM and URANS

4.3.6. COMPUTATIONAL EFFICIENCY

In this chapter, one URANS simulation is executed on 20 cores per case. The computational domain size is 15m×25m, discretized to 1.8e5 cells. The computer cluster operating system is Linux-based. The CPU processor used in this case is Intel(R) Xeon(R) E5-2640v4 with a frequency of 2.4 GHz. The DTVPM is computed as an order of $O(N_v^2)$ in serial processor, where N_v is the number of wake particles. Figure 4.25 compares DTVPM and URANS based on computational efficiency. The x axis represents simulation time for the first 5 revolutions. T is the rotation period of Savonius rotor. And y axis represents computational efficiency of numerical methods, which is characterized by the ratio of wall-clock time and simulation time. It is observed that the serial DTVPM simulation is about 20 to 1e4 times faster than the parallel URANS simulation in 5 revolutions. On the other hand, as indicated in Table 4.3, the maximum Δc_q predicted by DTVPM with viscous correction is 0.38 on average. Hence, under the premise of ensuring reasonable accuracy, DTVPM with viscous correction is a good alternative to study unsteady Savonius rotor.

4.4. CONCLUSIONS

Vortex-based methods have been limited by small angle assumptions. To break the constraint, a VPM with double wake for a single-stage two-bladed semicircular Savonius rotor with no gap width is proposed at the beginning of the work. But it predicts asymmetrical forces on the Savonius rotor. To avoid asymmetrical rotation, a double-trailing-edge-wake-modelling is applied to VPM, namely DTVPM. It is suitable for full-period

rotations, and independent from empirical parameters and post-corrected procedures for the Savonius rotor. The location of trailing edge is illustrated to be essential to force calculation. DTVPM is effective to avoid asymmetrical force variations. Meanwhile, the computational accuracy is compared based on the selection of vortex core models. Results show that Vatistas and Lamb Oseen models predict a similar velocity distribution at $x/R = 2$. Vatistas model with $r_c = 0.012$m has a maximum $\Delta(U/U_\infty)$ of 0.43 with a standard deviation of 0.08 at $x/R = 2$. In the far-wake region $x/R = 18$, Vatistas model with $r_c = 0.012$m differs from URANS in a maximum $\Delta(U/U_\infty)$ of 0.12 with a standard deviation of 0.03. A remarkable finding is that the downstream velocity variation and power performance are dependent more on the choice of vortex core radius.

In general, the bound and latest wake vortex circulations are calculated at each time step. The wake vortex particles are convected with the local velocity. However, the assumption of inviscid flow cannot represent the practical local velocity. So, the viscous correction for tip vortices is implemented to simulate viscous effects near blade tips. And Δc_p is improved from -0.10 to 0.01 and from -0.27 to 0.01 at $\lambda = 1.0, 1.2$ after viscous correcting, respectively.

The proposed DTVPM with viscous correction is shown to be a cost-effective method by comparison with high-fidelity computational results for a number of Savonius motions. The serial DTVPM simulation with maximum Δc_q of 0.38 on average is around 1e4 times faster than the parallel URANS simulation. Results of c_p from different methods show that URANS and DTVPM with viscous correction predict more stable results for varied tip speed ratio with standard deviation of 0.02. Through observations of flow characteristics for different phase angles at $\lambda = 0.8$, DTVPM is able to capture flow structures at $0 \leq x/R \leq 2$ but predicts a larger deflection of vortex position in y direction at $x/R \geq 2$. It can be improved by considering viscous effects downstream.

In this chapter, a cost-effective vortex method, DTVPM, has been applied to a Savonius rotor. It is capable of tackling the absence of flow viscosity and enhances computational efficiency. The hybrid VAWT has yet to gain popularity. A comprehensive analysis of hybrid VAWTs using a lower-fidelity model is of great importance. To extend the application of the cost-effective method and contribute to the hybrid VAWT design, it should be adapted into more complex cases, e.g., hybrid VAWT system. In the next chapter, the vortex method is implemented to a hybrid VAWT case. Results are compared to those from URANS simulations.

REFERENCES

[1] J. Pan, C. Ferreira, and A. vanZuijlen. Estimation of power performances and flow characteristics for a Savonius rotor by vortex particle method. *Wind Energy* 26.1 (Jan. 2023), pp. 76–97.

[2] G. Solari. *Wind Science and Engineering: Origins, Developments, Fundamentals and Advancements*. Springer, 2019.

[3] B. N. Owens. *The Wind Power Story: A Century of Innovation that Reshaped the Global Energy Landscape*. John Wiley and Sons, 2019.

[4] J.-L. Menet and N. Bourabaa. Increase in the Savonius rotors efficiency via a parametric investigation (2004).

[5] C. Mimeau and I. Mortazavi. A Review of Vortex Methods and Their Applications: From Creation to Recent Advances. *Fluids* 6.2 (2021), p. 68.

[6] G.-H. Cottet and P. D. Koumoutsakos. *Vortex Methods: Theory and Practice*. Cambridge University Press, 2000.

[7] H. Tryggeson. "Analytical Vortex Solutions to the Navier-Stokes Equation. Thesis for the degree of Doctor of Philosophy". PhD thesis. Sweden; Göteborg, 2007.

[8] J. Katz and A. Plotkin. *Low-Speed Aerodynamics*. 2nd ed. Cambridge Aerospace Series. Cambridge University Press, 2001.

[9] G. H. Vatistas, V. Kozel, and W. C. Mih. A simpler model for concentrated vortices. *Experiments in Fluids* 11 (1991), pp. 73–76.

[10] A. Abutunis and V. G. Menta. Comprehensive Parametric Study of Blockage Effect on the Performance of Horizontal Axis Hydrokinetic Turbines. *Energies* 15 (2022), p. 2585.

[11] T. Kinsey and G. Dumas. Impact of channel blockage on the performance of axial and cross-flow hydrokinetic turbines. *Renewable Energy* 103 (2017), pp. 239–254.

[12] B. F. Blackwell, L. V. Feltz, and R. E. Sheldahl. *Wind tunnel performance data for two-and three-bucket Savonius rotors*. Sandia Laboratories Springfield, VA, USA, 1977.

[13] O. Hald and V. M. del Prete. Convergence of vortex methods for Euler's equations. *Mathematics of Computation* 32 (1978), pp. 791–809.

[14] W. Kaufmann. Über die Ausbreitung kreiszylindrischer Wirbel in zahen Flussigkeiten. *Ing. Arch.* 31 (1962), pp. 1–9.

[15] H. Lamb. *Hydrodynamics*. Cambridge University Press (6th edition), London, 1932.

[16] C. W. Oseen. Über Wirbelbewegung in Einer Reibenden Flüssigkeit. *Arkiv för matematik, astronomi och fysik* 7 (1912), pp. 14–21.

[17] J. G. L. M. J. Bhagwat. "Generalized viscous vortex model for application to free-vortex wake and aeroacoustic calculations". In: *58thAnnual Forum and Technology Display of the American Helicopter Society International, Montréal,Canada*. 2002.

[18] A. D. Aliferis, M. S. Jessen, T. Bracchi, and R. J. Hearst. Performance and wake of a Savonius vertical-axis wind turbine under different incoming conditions. *Wind Energy* 22.9 (2019), pp. 1260–1273.

[19] K. Ramesh, A. Gopalarathnam, K. Granlund, M. V. Ol, and J. R. Edwards. Discrete-vortex method with novel shedding criterion for unsteady aerofoil flows with intermittent leading-edge vortex shedding. *Journal of Fluid Mechanics* 751 (2014), pp. 500–538.

5

A VISCOUS VORTEX PARTICLE METHOD FOR A HYBRID VAWT

Parts of this chapter have been submitted to Physics of Fluids.

Chapter 4 implemented a viscous VPM to a Savonius rotor. It shows the capability of VPM in studying the flow features and power performance of the Savonius rotor. To develop VPM for various types of VAWTs, this chapter examines the capability and flexibility of the vortex particle method in Darrieus and hybrid VAWT cases. The inviscid vortex particle method is first applied to the single Darrieus and hybrid VAWT, but the quantification results are overestimated due to the neglect of the viscosity. The viscous polar is coupled with the inviscid vortex particle method and the results are verified against the unsteady Reynolds Averaged Navier Stokes (URANS) simulations in Chapter 3. The flow features are well captured in inviscid and viscous vortex particle methods compared to the URANS simulations. The quantitative predictions for power performances yield substantial deviations from the inviscid vortex particle method. However, the flexibility of the vortex particle method allows us to apply the viscous effects to the VAWT cases.

Jingna Pan, Carlos Ferreira, Alexander van Zuijlen, A viscous vortex particle method for a Darrieus-Savonius combined vertical axis wind turbine, under review.

5.1. INTRODUCTION

The modeling of VAWTs remains a challenge compared to HAWTs due to the insufficiently accurate/cost-effective numerical approaches and previous conclusions favoring HAWTs, leading to reduced investment of VAWT development [1, 2]. Vortex methods present a distinct advantage in terms of computational efficiency compared to the Eulerian methods [3, 4, 5, 6]. Previous work has analyzed the flow physics and blade forces of a Savonius using the vortex method. Based on the implementation of DTVPM, the vortex method is extended to various types of VAWTs. This chapter stands out due to its novelty in studying the application of VPM on a hybrid VAWT. While previous studies have explored the benefits of VPM in improving computational efficiency, the analysis of this method on a hybrid VAWT with a complex wake structure is unique. This chapter aims to extend the application of VPM with cost-effective simulations for the complex wake dynamics of VAWTs. This study delves into a comprehensive numerical analysis of a two-dimensional (2D) hybrid VAWT, focusing on improving the VPM and validating against high-fidelity simulation. The primary work is to assess the efficiency and precision of these two methods in simulating the hybrid turbine's wake dynamics and blade forces.

The outcomes of this research are expected to offer valuable insights into the selection of appropriate numerical methods for investigating flow dynamics in hybrid VAWTs. These insights hold the potential to drive advancements in wind energy technology and enhance the understanding of intricate turbine behavior, contributing to the sustainable energy landscape.

This chapter is structured as follows. Section 5.2 presents the methodology of VPM and the high-fidelity numerical tool (URANS). Section 5.3 compares the numerical results of the two methods. The main conclusions are drawn in Section 5.4.

5.2. METHODOLOGY

To simulate the hybrid VAWT using the vortex particle method, we decompose the hybrid VAWT into three substeps: simulation of two-bladed Savonius, simulation of two-bladed Darrieus, and simulation of the interaction between Savonius and Darrieus. The flow around the Savonius has been resolved using DTVPM [7], which is used for the Savonius part of hybrid VAWT in this chapter. The implementation of the vortex particle method on the Darrieus part will be first addressed in this section, followed by the implementation of the interaction between Savonius and Darrieus. The vortex method is validated against URANS simulation.

5.2.1. DTVPM WITH VISCOUS CORRECTION FOR DARRIEUS

The Darrieus blade is discretized into several vortex elements. The vortex element is shown in Figure 5.1. Each element has a vortex point (x_v, y_v) at the quarter-chord position (x_c, y_c) and a control point at the three-quarter-chord position [8, 9, 10]. The normal direction $\vec{n}$ is vertical to the vortex element and towards the rotation axis. The tangential direction $\vec{\tau}$ is from the leading edge to the trailing edge. The wake particle is shed from the trailing edge. Each vortex will induce velocity at the control point to avoid the singularity problem, which is a problem of infinite self-induced velocities of vortex particles

[11, 3].

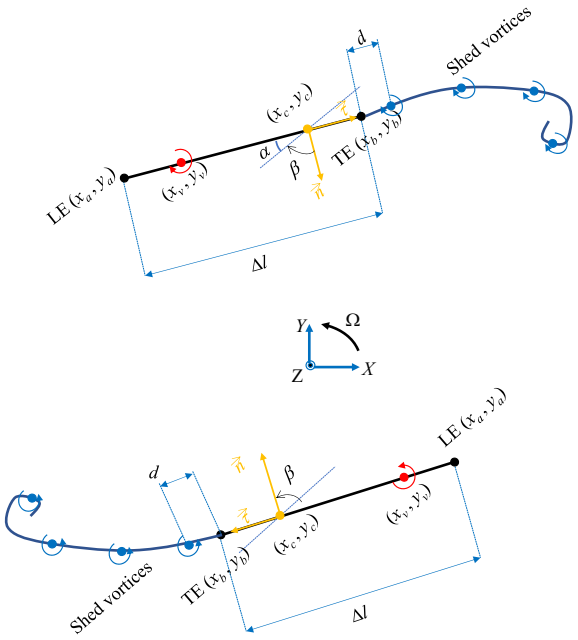

Figure 5.1: Vortex element for Darrieus blade

The flow chart of the principle vortex particle method is shown in the yellow rectangle of Figure 5.2. Kelvin's theorem serves for the vortex particle method because the time rate of circulation change in a closed curve should be conserved as zero [12, 9], see Equation 4.7. Additionally, the Neumann boundary condition satisfies each airfoil's control point as the fluid cannot go through a surface [13], also known as the non-entry boundary condition (non-entry BC). Once the bound and shed vortex elements are determined, their circulations can be obtained and applied to secondary computations. Meanwhile, a time-stepping procedure is implemented in a matrix for the vortex particle method, ensuring Kelvin's theorem and the Neumann boundary condition at each time step.

The viscous correction of the vortex particle method is shown in Figure 5.2 based on the principle vortex particle method. The assumption of the vortex particle method is incompressible, inviscid, irrotational flow, so it cannot predict viscous effects. In this section, the viscous effects are considered by implementing a viscous polar on the blade. Given the flow field from the principle VPM, the blade angle of attack (AoA) on the quarter-chord position can be calculated in one revolution. Since the mounted position is half-chord position, the pitch angle is taken into account while implementing viscous correction. The imposed polar is usually obtained from experiments. As the airfoil in the Darrieus rotor is not in an unbounded fluid, the Kutta-Joukowski theorem ($L = \rho U_\infty \Gamma$) does not apply to get the bound circulation Γ. In the Darrieus rotor case, the presence of the second airfoil requires the application of the generalized Kutta-Joukowski theorem

developed in Ref. [9, 14, 15]. Coupled with the imposed polar, the bound circulation can be calculated from lift force, shown as Equation 5.1. In this equation, U_∞ is the freestream velocity, U_{ind} is the velocity induced by other vortices at the airfoil vortex location, and U_{rot} is the blade rotation speed. This step replaces the Neumann boundary condition. After the calculation of the bound circulation, the same procedure as the principle VPM (shown in the blue rectangle) is applied.

$$L = \rho(U_\infty + U_{ind} + U_{rot})\Gamma \tag{5.1}$$

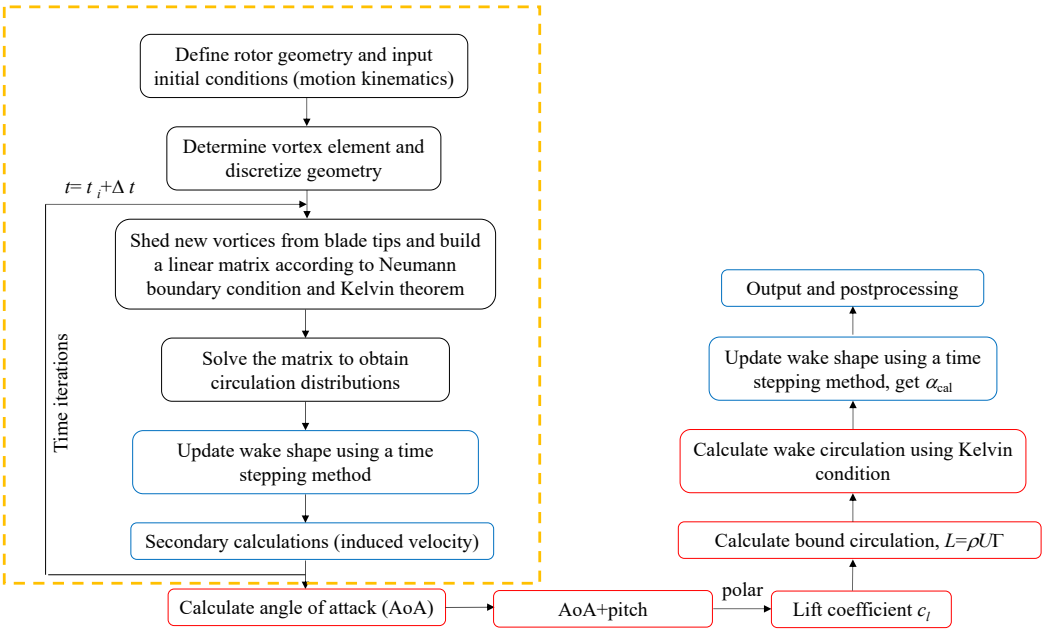

Figure 5.2: Flow chart of the viscous correction in the vortex method

Given the airfoil polar, the aerodynamic force coefficients c_n, c_t, c_x, c_y are calculated from Equations 5.2, 5.3, 5.4 and 5.5.

$$c_n = c_l \cdot \cos\alpha + c_d \cdot \sin\alpha \tag{5.2}$$

$$c_t = c_l \cdot \sin\alpha - c_d \cdot \cos\alpha \tag{5.3}$$

$$c_x = c_n \cdot \sin\theta - c_t \cdot \cos\theta \tag{5.4}$$

$$c_y = -c_n \cdot \cos\theta - c_t \cdot \sin\theta \tag{5.5}$$

5.2.2. DTVPM WITH VISCOUS CORRECTION FOR HYBRID VAWT

In the case of hybrid VAWT, the Darrieus blade is represented by one vortex element, and the Savonius blade is discretized into 36 vortex elements. The two Darrieus blades in hybrid VAWT use a similar procedure to the single Darrieus shown as Figure 5.2. The angle of attack is obtained from the vortex particle method. The Savonius in the hybrid VAWT introduces blockage in front of the hybrid VAWT and creates perturbance to the flow field behind the hybrid VAWT, so the velocity deficit is supposed to be higher than the single Darrieus rotor. Due to the blade-wake interaction in the hybrid VAWT, the angle of attack used for the Darrieus part of the hybrid VAWT differs from the single Darrieus rotor.

The viscous correction is applied to the hybrid VAWT. The force on the Darrieus part is calculated from the polar, and the force of the Savonius is calculated from the pressure difference of the blade using the unsteady Bernoulli equation. The detailed information on the force calculation for the Savonius part can be found in Ref. [7]. The force of the hybrid VAWT is the superposition of the Savonius' force and Darrieus' force.

5.2.3. URANS SIMULATION

This section briefly introduces the simulation settings of URANS. The detailed information can be found in Chapter 3.

COMPUTATIONAL DOMAIN AND MESH

A hybrid VAWT with a thin Savonius and two NACA0021 airfoils rotating around the same axis is investigated in this study. The computational domain is split into two rotational subdomains and a stationary subdomain as shown in Chapter 3. Each rotational subdomain contains a Darrieus or Savonius part. The computational domain is $34R_D$ in width and $20R_D$ high, where R_D is the radius of Darrieus. The cyclic Arbitrary Mesh Interface (AMI) is applied to the interface between the dynamic and static subdomains, dynamic and dynamic subdomains to enable flow simulation across disconnected and adjacent mesh domains [16, 17]. The near-wall mesh is refined as shown in Chapter 3.

NUMERICAL CONDITIONS AND SETTINGS

The URANS simulation case uses SST k-ω turbulent solver with pimpleDyMFoam application. The simulation parameters are summarized in Table 5.1. For the two-dimensional incompressible flow, "RAS" is specified as the simulation type in "constant/turbulenceProperties" to simulate viscous flow.

Table 5.1: Simulation and geometrical parameters of hybrid VAWT

Geometrical parameter	Value / Specification	Unit
Radius of Darrieus rotor R_D	0.74	m
Radius of Savonius rotor R_S	0.148	m
Inlet velocity U_∞	4.01	m/s
Blade of Darrieus rotor	Flat plate in VPM, NACA0021 in URANS	-
Blade of Savonius rotor	Semi-circle	-
Thickness of Savonius blade t_S	0 in VPM, 1e-3*R_S in URANS	m
Number of blades	2 in Darrieus rotor, 2 in Savonius rotor	-
Tip speed ratio λ	4.0	-
Attachment angle γ	[0, 30, 60, 90]	°
Simulation parameter	**Value**	**Unit**
Dynamic viscosity μ	1.808e-5	kg/(m·s)
Angle step size $\Delta\theta$	0.24	°
Total number of cell	167902	-
Height of first row's cell	0.022	mm
Growth factor of boundary layer	1.2	-
Number of boundary layer rows	28	-

5.3. RESULTS

The application of DTVPM on the Savonius rotor has been validated in terms of power performance and flow features [7]. A similar vortex method (VPM) is implemented for the Darrieus rotor and hybrid VAWT. The sensitivity study of VPM on the Darrieus rotor and hybrid VAWT is elaborated in the Appendix. This section will mainly compare the URANS and the VPM with inviscid and viscous polars imposed for the Darrieus rotor and hybrid VAWT. The inviscid polar is from the thin airfoil theory and relevant to lift coefficient $c_l = 2\pi \sin\alpha_{eff}$ and drag coefficient $c_d = 0$ with the assumption of inviscid incompressible flow. α_{eff} is the sum of the measured angle of attack on the quarter chord position and the pitch angle of the Darrieus blade. The viscous polar for NACA0021 is taken from Ref. [18]

5.3.1. RESULTS OF DARRIEUS ROTOR

The normal force coefficients of the top blade of the Darrieus rotor from URANS and VPM are depicted in Figure 5.3. It is observed that VPM with polars agree well with the URANS results. The plateau at θ = 60°-150° from VPM with viscous polar refers to the dynamic stall occurrence at high angle of attack. The thrust coefficient and lateral force coefficient from URANS validate the VPM for Darrieus rotor.

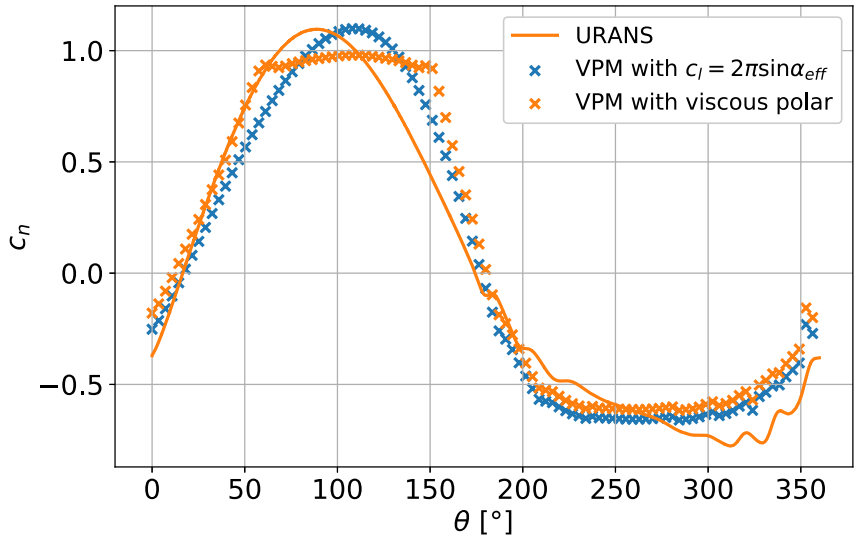

Figure 5.3: Normal force coefficient of the top blade of Darrieus rotor

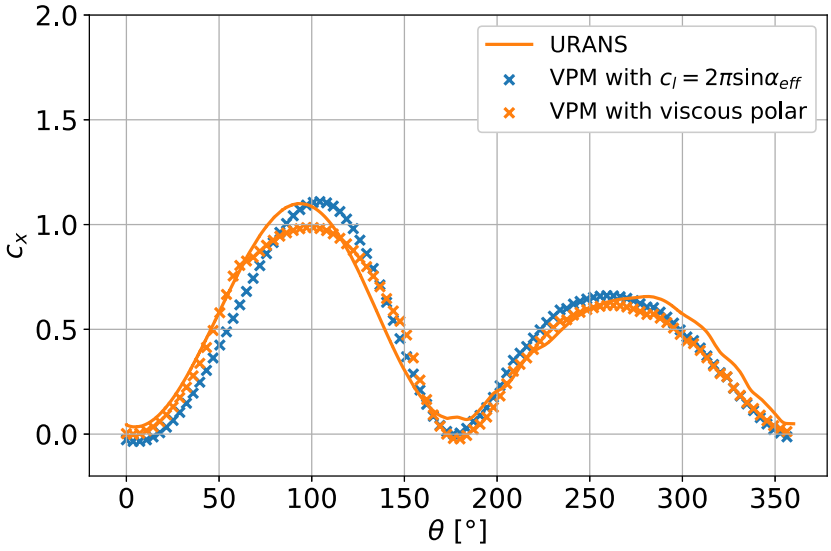

Figure 5.4: Thrust coefficient of the top blade of Darrieus rotor

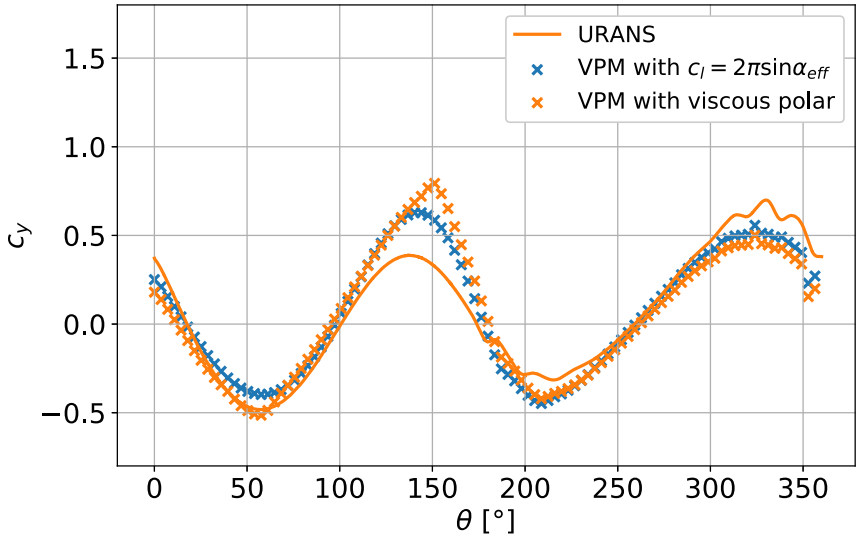

Figure 5.5: Lateral force coefficient of the top blade of Darrieus rotor

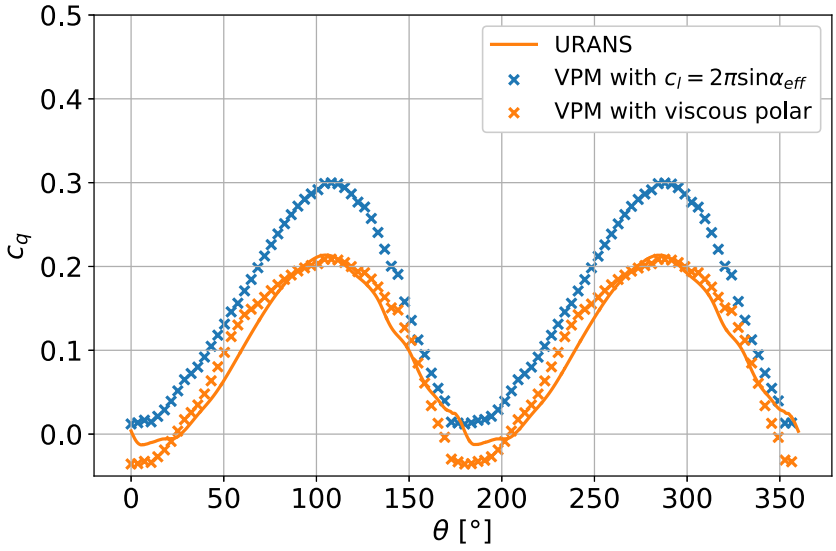

Figure 5.6: Torque coefficient of the Darrieus rotor

The torque coefficient of the Darrieus rotor from URANS and VPM are depicted in Figure 5.6. It is observed that the torque coefficient from VPM with viscous polar agrees well with that from URANS. However, VPM with $c_l = 2\pi\sin\alpha_{eff}$ overestimates the torque coefficient of the Darrieus rotor. This is attributed to the neglect of viscosity. The viscous polar correction improves power performance prediction compared with the VPM with $c_l = 2\pi\sin\alpha_{eff}$. Variations of c_q from the three methods have a similar trend. The magnitude of the $c_{q_{max}}$ from VPM with $c_l = 2\pi\sin\alpha_{eff}$ is around 50% higher than that from URANS. It can be attributed to the modeling of the airfoil as a flat plate in VPM with $c_l = 2\pi\sin\alpha_{eff}$. The other two methods model the blade as NACA0021. At $\theta = 50°$-$150°$ (upwind side), the viscous polar introduces flow separation effects to the force calculation, which enhance the prediction accuracy of VPM. But the flow field does not show obvious flow separation due to the limitation of single wake model. To capture the flow separation phenomenon in the flow field, a double wake model would be developed in the future.

Table 5.2: Comparison of power coefficients for a Darrieus rotor

	URANS	VPM with viscous polar	VPM with $c_l = 2\pi\sin\alpha_{eff}$
c_p	0.406	0.413	0.629

Power coefficients of Darrieus rotor are compared between VPM with $c_l = 2\pi\sin\alpha_{eff}$, URANS and VPM with viscous polar in Table 5.2. The VPM with viscous polar and $c_l =$

$2\pi\sin\alpha_{eff}$ predicts 1.72% and 54.9% difference from the URANS simulation. The negligible difference between VPM with viscous polar and URANS proves the flexibility of VPM and validity of viscous correction.

The vorticity and velocity fields of the Darrieus rotor from URANS, VPM with viscous polar and VPM with $c_l = 2\pi\sin\alpha_{eff}$ are depicted in Figures 5.7 and 5.8. It is observed that the three methods have a similar pattern for the vorticity and velocity predictions. The DTVPM with polar correction can capture the main flow structure of the single Darrieus compared to the URANS simulation. The analysis will be extended to the hybrid VAWT in Section 5.3.2.

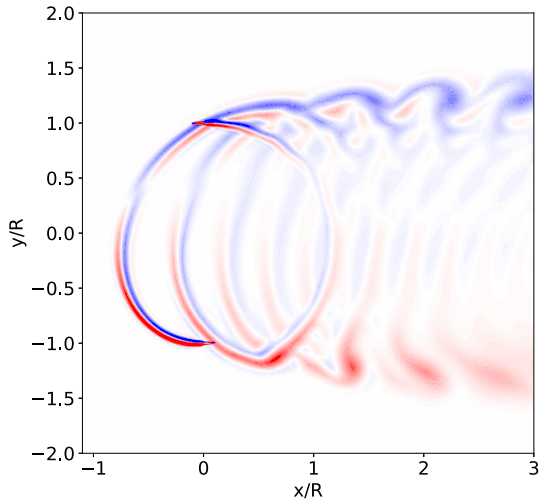

(a) URANS

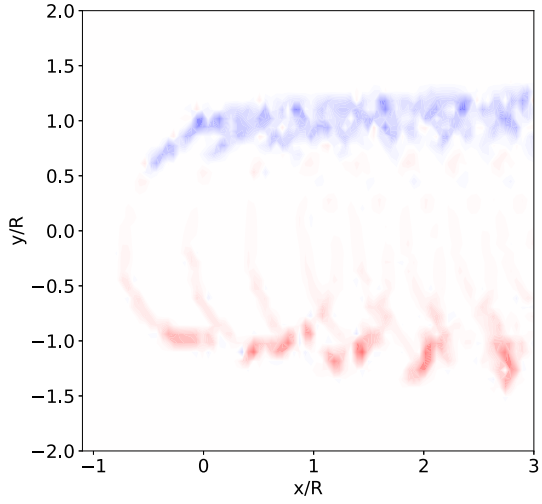

(b) VPM (viscous polar)

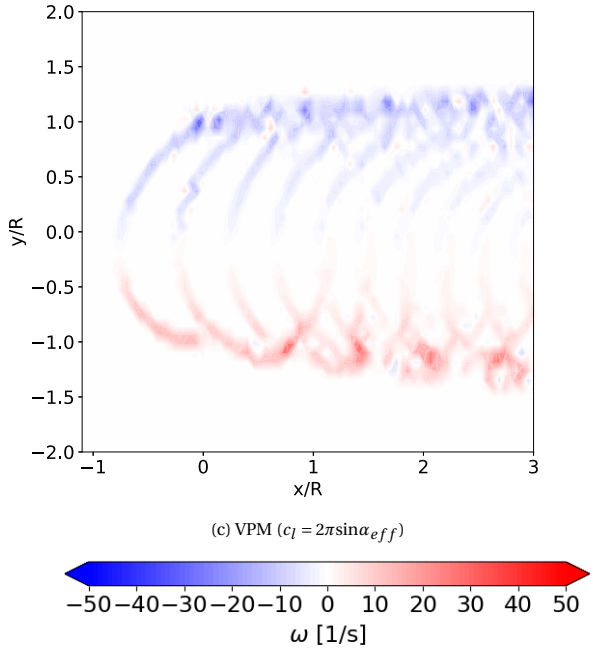

(c) VPM ($c_l = 2\pi \sin\alpha_{eff}$)

Figure 5.7: Comparison of vorticity field for Darrieus rotor from URANS, VPM with viscous polar and $c_l = 2\pi \sin\alpha_{eff}$, $\lambda_D = 4.0$, $\theta = 360°$

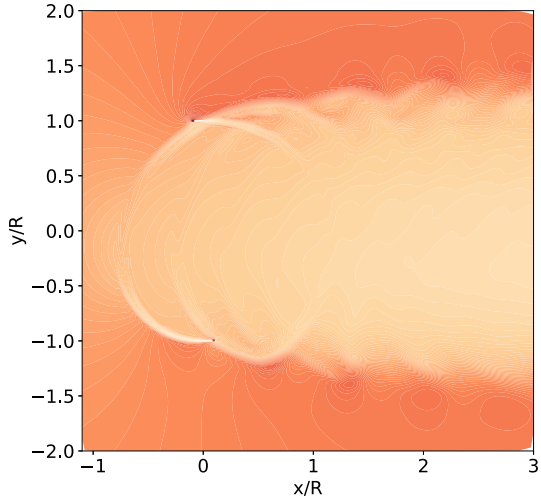

(a) URANS

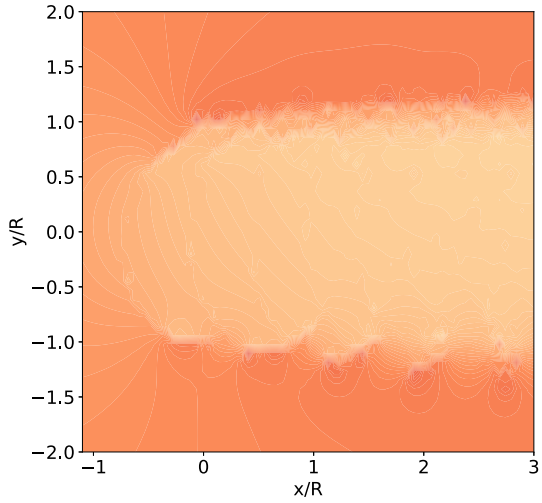

(b) DTVPM (viscous polar)

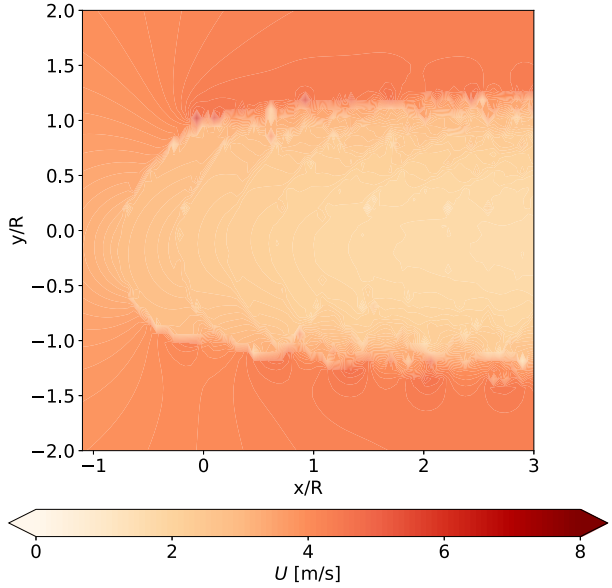

(c) DTVPM ($c_l = 2\pi \sin\alpha_{eff}$)

Figure 5.8: Comparison of velocity field for Darrieus rotor from URANS, VPM with viscous polar and $c_l = 2\pi \sin\alpha_{eff}$, $\lambda_D = 4.0$, $\theta = 360°$

5.3.2. Results of hybrid VAWT

The forces and flow fields of hybrid VAWT are compared between URANS and the vortex method in this section. With the presence of Savonius in hybrid VAWT, DTVPM with viscous polar is implemented for hybrid VAWT.

COMPARISON OF THE VORTEX CORE MODEL: LAMB OSEEN AND VATISTAS MODELS

The vortex core model is used to characterize the size of the shedding vortex. It can be categorized into two groups: constant vortex core radius and growing vortex core radius. Lamb Oseen and Vatistas models represent the two groups, respectively. This section compares the two models in terms of the vorticity field. Figure 5.9 depicts the vorticity fields of hybrid VAWT from the URANS, DTVPM with Vatistas model, and DTVPM with Lamb Oseen model. It is observed that DTVPM with different vortex core models can capture the main flow features of the hybrid VAWT compared to URANS results. The counter-clockwise vortex (shed from Savonius) of the Lamb Oseen model moves faster than that of the URANS and Vatistias model. The vortex blob appears at $x/R = 3$ in the flow fields of URANS and Vatistas model, but it appears at $x/R = 2$ in the flow fields of the Lamb Oseen model. The torque variation of the hybrid VAWT from URANS and different vortex core models is shown in Figure 5.10. It is shown that the predicted torque from the three methods has a similar trend. The power coefficient of the hybrid VAWT is predicted as 0.36938, 0.38028, and 0.48466 by URANS, DTVPM with Vatistas and Lamb Oseen models. The overestimation from the Lamb Oseen model is attributed to the vortex core radius assumption. To accurately predict the flow pattern and power coefficient of the hybrid VAWT, DTVPM with Vatistas model is chosen for this work.

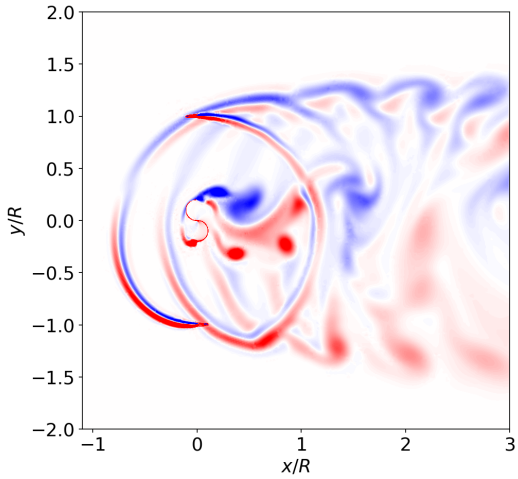

(a) URANS

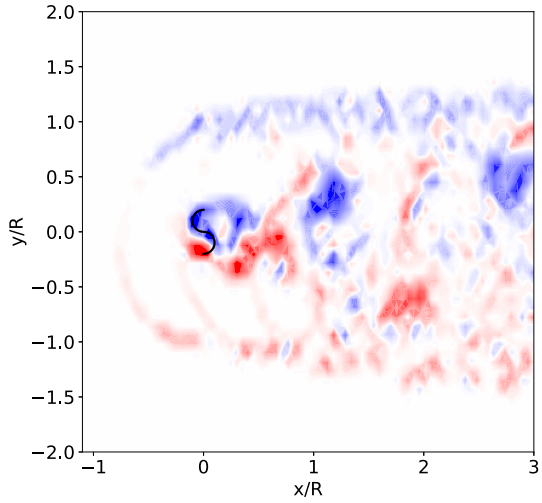

(b) Vatistas model

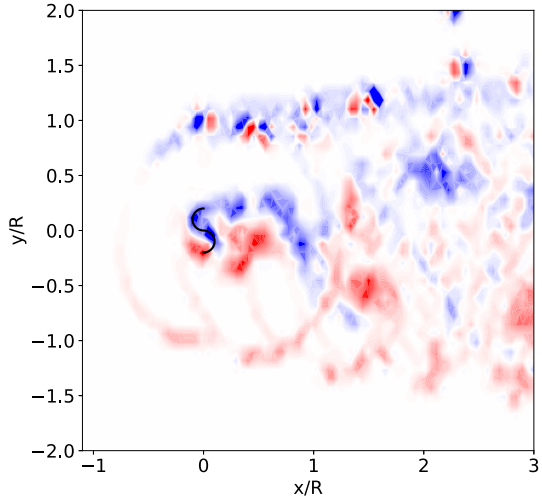

(c) Lamb Oseen model

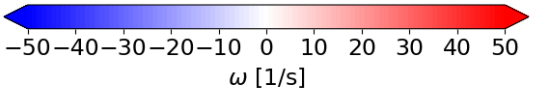

Figure 5.9: Vorticity fields of hybrid VAWT from URANS, Vatistas and Lamb Oseen models, $\theta = 360°$

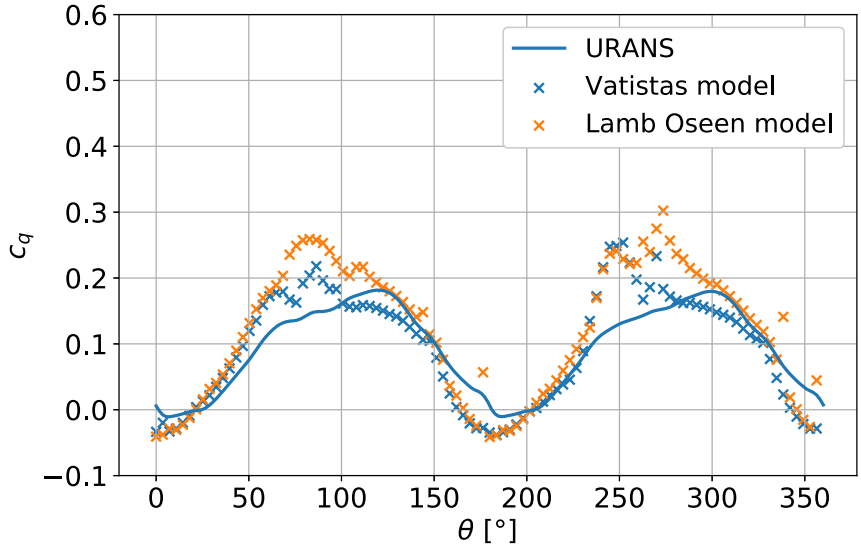

Figure 5.10: Torque coefficient of the hybrid VAWT from URANS, Vatistas and Lamb Oseen models

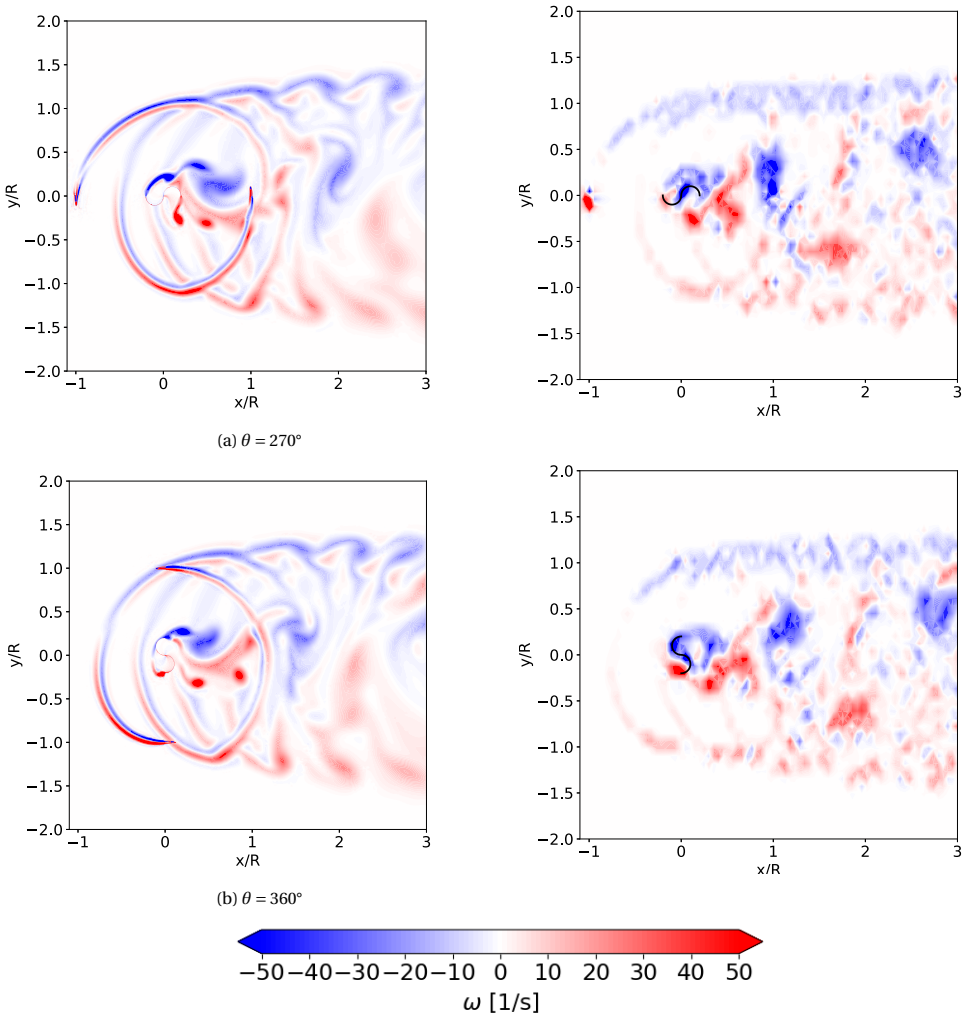

Figure 5.11: Vorticity fields of a hybrid VAWT, $\lambda = 4.0$, $\gamma = 0°$ (Left: URANS, right: DTVPM with viscous polar)

Results from DTVPM with viscous polar are compared to those of URANS simulation. The vorticity fields of the hybrid VAWT at various azimuth positions are shown in Figure 5.11. At azimuth angles $\theta = 270°$ and 360°, the generation and detachment of the trailing edge vortex blobs from Savonius blade tips alternate in the flow field. The shedding wake from the Darrieus blades is modified by the wake of Savonius rotor, resulting in the force fluctuation of the hybrid VAWT. Through comparisons between two numerical methods, DTVPM could predict comparable vorticity fields for the hybrid VAWT.

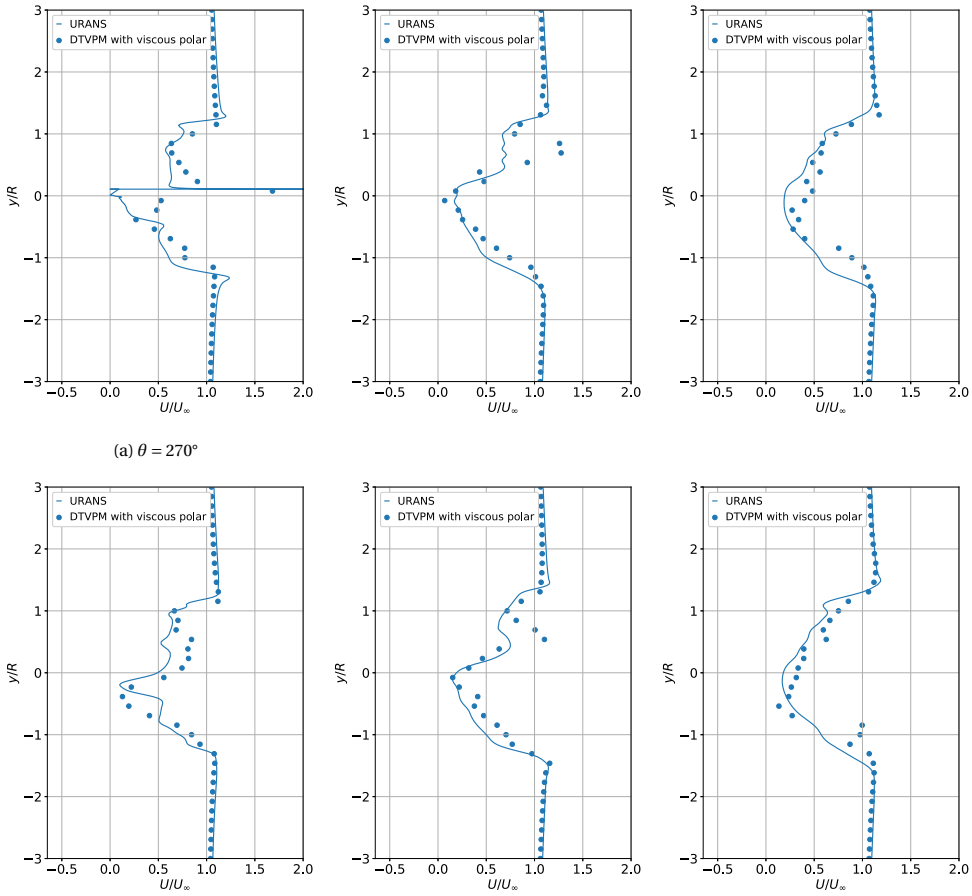

(a) $\theta = 270°$

(b) $\theta = 360°$

Figure 5.12: Downstream velocity curve of a hybrid VAWT from URANS and DTVPM, $\lambda_{hybrid} = 4.0$ (Left: $x/R = 1$, middle: $x/R = 2$, right: $x/R = 3$)

Figure 5.12 depicts the downstream velocity curves from URANS simulations and DTVPM with viscous polar at two azimuth positions $\theta = 270°$, 360° and three downstream positions $x/R = 1.0$, 2.0, 3.0. At $\theta = 270°$, the Darrieus blade is located at the sampled line $x/R = 1.0$, leading to an abrupt local velocity change at $y/R \approx 0$. For the other two downstream positions $x/R = 2.0$ and 3.0, both URANS and DTVPM can capture a similar magnitude of minimum velocity at $y/R \approx 0$. At $x/R = 2.0$, $y/R = 0.5$-1.0, the velocity curve from DTVPM slightly deviates from URANS simulation. It is attributed to the difference in vortex shedding between URANS and DTVPM. The vortices shed from the Savonius in URANS simulation behave differently from those in DTVPM simulation after one diameter downstream the turbine, which is also observed in Ref. [7]. The overall tendency downstream of the velocity curve from DTVPM agrees well with that from URANS.

POWER COEFFICIENT AT $\gamma = 0°$

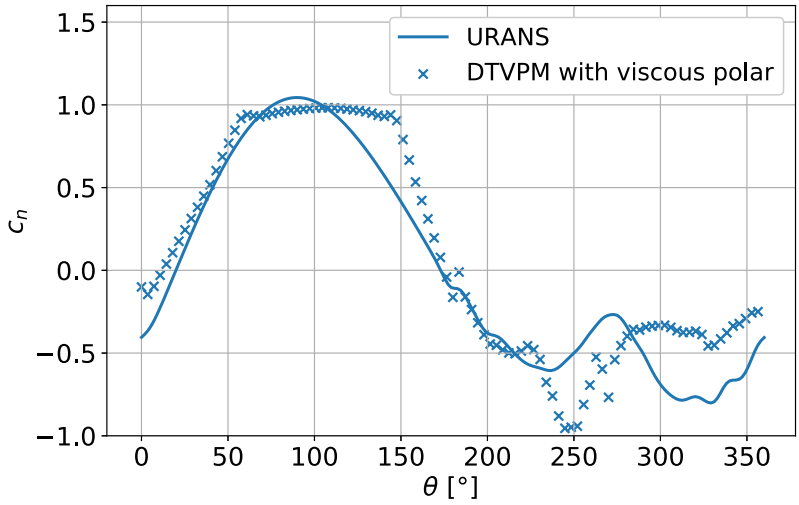

Figure 5.13: Normal force coefficient of the top blade of the hybrid VAWT

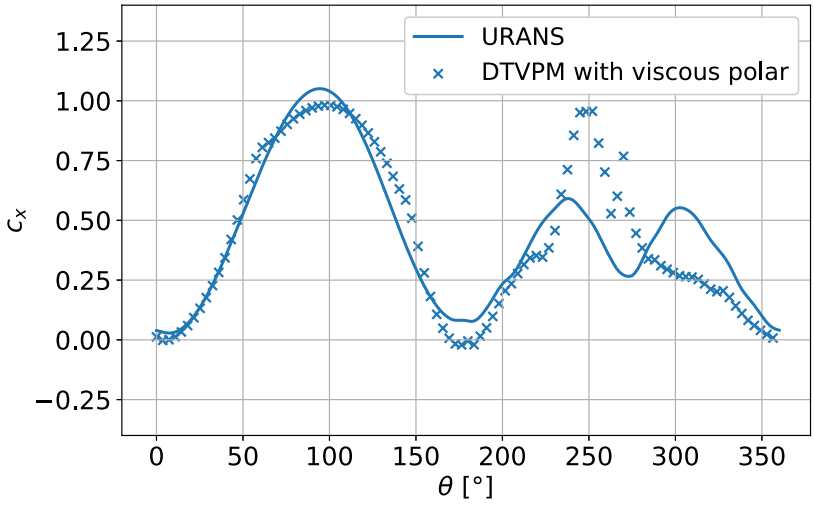

Figure 5.14: Thrust coefficient of the top blade of the hybrid VAWT

The force coefficients of the top Darrieus blade in hybrid VAWT are depicted in Figures 5.13-5.14. The normal force coefficient c_n from DTVPM with viscous correction depends on the selection of polar. The maximum c_n from DTVPM deviates around 5.84% from

the URANS simulation. The variation of c_x for the top blade from the two methods has a good agreement except for azimuth positions of $\theta = 240°$-$330°$. The instability of DTVPM comes from the strong blade-vortex interaction in these rotation phases [19].

The magnitudes and the power coefficient of a hybrid VAWT from URANS and DTVPM simulations are compared in Table 5.3 and Figure 5.15. The power coefficient from DTVPM with viscous correction is around 2.95% higher compared to the results from URANS simulation. Compared to the single Darrieus in Figure 5.6, the force fluctuations are well captured by URANS and DTVPM simulations. The torque coefficient fluctuates at $\theta = 60°$-$120°$ and $240°$-$300°$ due to the blade-vortex interaction.

Table 5.3: Comparison of power coefficients from URANS and DTVPM for a hybrid VAWT

	URANS	DTVPM with viscous polar
c_p	0.3694	0.3803

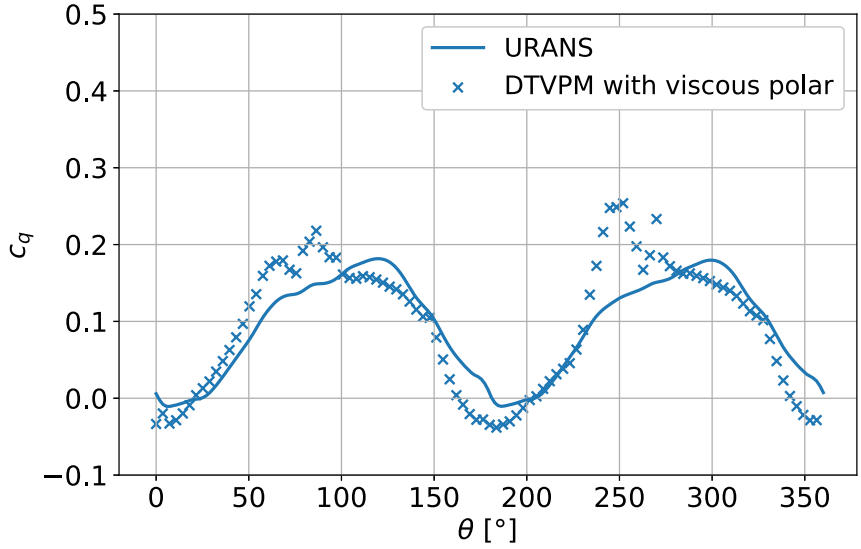

Figure 5.15: Torque coefficient of the hybrid VAWT

POWER COEFFICIENT AT VARIOUS γ

The effect of the attachment angle on the power coefficient of the hybrid VAWT from URANS and DTVPM is compared in Figure 5.16. It is observed that URANS and DTVPM with viscous correction predict $\gamma = 60°$ and $90°$ with higher power coefficient than the $\gamma = 0°$ and $30°$. It validates the effectiveness of the DTVPM with viscous correction.

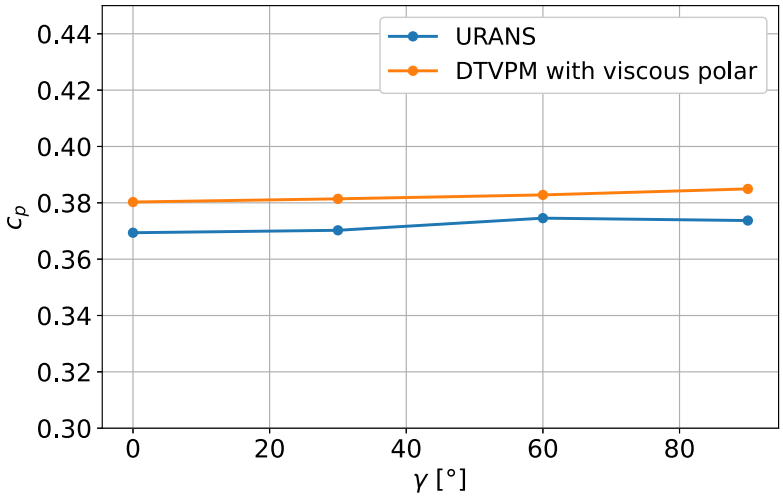

Figure 5.16: Power coefficients of a hybrid VAWT with various attachment angles

5.3.3. Comparison of hybrid VAWT and Darrieus rotor

The torque contribution of Darrieus blade to the torque generation during one revolution of hybrid VAWT and Darrieus rotor from VPM with polar correction is depicted in Table 5.4. The comparison between hybrid VAWT and Darrieus rotor is categorized in four phases: upwind windward (θ = 0°-90°), upwind leeward (θ = 90°-180°), downwind leeward (θ = 180°-270°) and downwind windward (θ = 270°-360°). It is observed that the torque contribution of the Darrieus blade in hybrid VAWT remains similar to that of the Darrieus rotor on the upwind side. On the downwind leeward side, the Darrieus blade of hybrid VAWT contributes 9.32% more to the overall torque generation compared to the single Darrieus rotor. This is also observed in Ref. [19], where the Darrieus blade interacts with the shed vortex from the advanced Savonius blade. On the downwind windward side, the Darrieus blade's torque contribution in hybrid VAWT is around 9.21% lower than that in the Darrieus rotor.

Table 5.4: Torque contribution of Darrieus blade to the torque generation during one revolution of hybrid VAWT and Darrieus rotor from VPM with polar correction

Torque contribution [%]	Upwind windward	Upwind leeward	Downwind leeward	Downwind windward
Hybrid VAWT	23.027	49.724	22.223	5.026
Darrieus rotor	21.333	51.571	12.797	14.299

5.3.4. COMPUTATIONAL EFFICIENCY

The computational efficiency of DTVPM is illustrated in the simulation of hybrid VAWT with twenty revolutions. Table 5.5 shows that a serial simulation of DTVPM is around 20 times faster than a parallel simulation of URANS with reasonable accuracy in terms of ten revolutions. The computational speed of URANS and DTVPM for twenty revolutions is compared in Figure 5.17. It is observed that the computational speed of URANS remains stable and much slower than DTVPM during the twenty revolutions. The computational speed of DTVPM increases with the increasing number of revolutions, which means the increasing number of vortex particles in the flow field. This section suggests that the discretization of time in DTVPM needs to be considered as a factor of simulation in terms of computational efficiency.

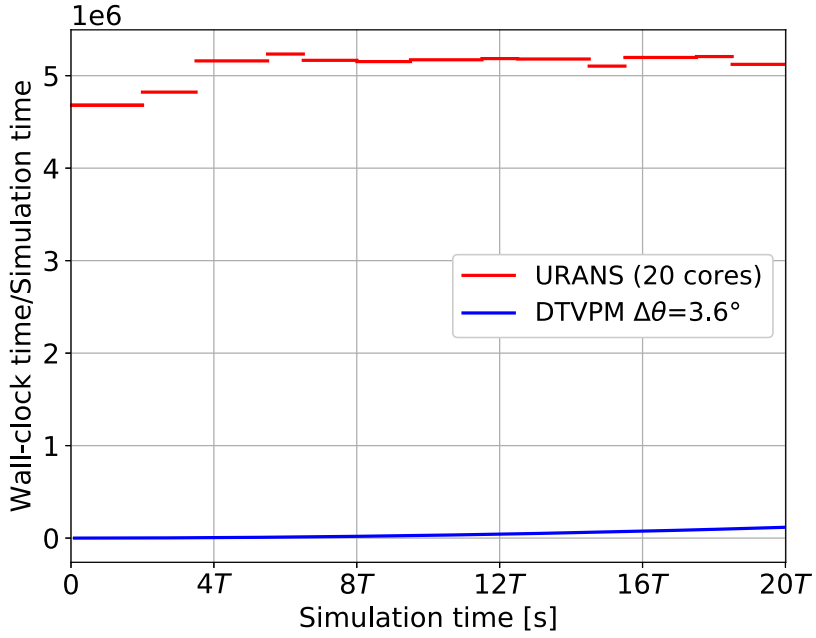

Figure 5.17: Comparison of computational speed for URANS and DTVPM simulations

Table 5.5: Computational efficiency of a hybrid VAWT for ten revolutions

Simulation	URANS	DTVPM with viscous polar
Computational element	1.68e5 cells	1e3 vortex particles
Number of cores	20	1
Wall-clock hours	182.5	8.2

5.4. CONCLUSIONS

Vortex particle methods for unsteady airfoils have been studied on the Savonius rotor in the previous research [7]. This work extended the implementation of the vortex particle methods to the hybrid VAWT and proposed a viscous correction to enhance the simulation accuracy. The vortex method with viscous correction (VPM for Darrieus, DTVPM for hybrid VAWT) used the same principle as the traditional vortex particle method, where the fluid viscosity is neglected (leading to overestimation of blade forces). By imposing the polar calculation, it is effective to predict the comparable force variations with high-fidelity simulation (URANS). Meanwhile, the computational efficiency is compared between URANS and DTVPM for the hybrid VAWT. Results show that a serial simulation of DTVPM is around 20 times faster than a parallel simulation of URANS with reasonable accuracy in terms of ten revolutions.

With the use of viscous correction, the proposed numerical method, DTVPM, can be applied to a wide range of geometries: Savonius, Darrieus and hybrid VAWT with different attachment angles. By comparing with high-fidelity simulation, the proposed DTVPM is proven to be an inexpensive and reasonably accurate method. The results of blade forces and vortex structures obtained from DTVPM agree reasonably well with those from URANS simulations. Discrepancies between DTVPM and URANS could be attributed to the blade-vortex interaction in the hybrid VAWT, which needs model improvements in the future. Despite this limitation, the DTVPM can predict the flow field of complex rotor configurations. This research validates the effectiveness of DTVPM in solving unsteady flow and provides knowledge for the future design of the hybrid VAWT.

The modeling of VAWTs has been investigated using the Eulerian method and Lagrangian method in Parts II and III. The computational cost of the Lagrangian method is lower than that of the Eulerian method, while the Eulerian method has a high resolution in the near-wake region. It would be beneficial to combine the advantages of each method. Part IV will present a brief introduction to the Eulerian-Lagrangian method with a case of hybrid VAWT.

REFERENCES

[1] E. Martinez-Ojeda, F. J. Solorio Ordaz, and M. Sen. Vertical-axis wind-turbine computations using a 2D hybrid wake actuator-cylinder model. *Wind Energy Science* 6.4 (Aug. 2021), pp. 1061–1077.

[2] A. Barnes, D. Marshall-Cross, and B. R. Hughes. Towards a standard approach for future Vertical Axis Wind Turbine aerodynamics research and development. *Renewable and Sustainable Energy Reviews* 148 (Sept. 2021), p. 111221.

[3] C. Mimeau and I. Mortazavi. A Review of Vortex Methods and Their Applications: From Creation to Recent Advances. *Fluids* 6.2 (2021), p. 68.

[4] T. R. Quackenbush, C.-M. G. Lam, and D. B. Bliss. Vortex Methods for the Computational Analysis of Rotor/Body Interaction. *Journal of the American Helicopter Society* 39.4 (Oct. 1994), pp. 14–24.

[5] L. A. Barba. "Vortex Method for computing high-Reynolds number flows:Increased accuracy with a fully mesh-less formulation". PhD thesis. California Institute of Technology, 2004.

[6] G. Morgenthal and J. Walther. An immersed interface method for the Vortex-In-Cell algorithm. *Computers and Structures* 85 (2007), pp. 712–726.

[7] J. Pan, C. Ferreira, and A. vanZuijlen. Estimation of power performances and flow characteristics for a Savonius rotor by vortex particle method. *Wind Energy* 26.1 (Jan. 2023), pp. 76–97.

[8] Q. Zhang. "Modeling, Analysis, and Control of Close Formation Flight". PhD thesis. University of Toronto, 2019.

[9] J. Katz and A. Plotkin. *Low-Speed Aerodynamics*. 2nd ed. Cambridge Aerospace Series. Cambridge University Press, 2001.

[10] C. Bil. "Development and applicationof a computer-based systemforconceptual aircraft design". PhD thesis. Technische Universiteit Delft, 1988.

[11] M. R. Mendenhall and S. C. Perkins. *Prediction of Vortex SheddingFrom Circular and NoncircularBodies in Supersonic Flow*. Tech. rep. NASA Contractor Report 3754, 1984.

[12] P. Kundu and I. Cohen. Fluid Dynamics. In: *Fluid Mechanics*. Elsevier, 2002, pp. 474–546.

[13] S. Venkateshan and P. Swaminathan. Laplace and Poisson Equations. In: *Computational Methods in Engineering*. Elsevier, 2014, pp. 529–573.

[14] L. Clancy. *Aerodynamics*. London, 1975.

[15] A. Kuethe and J. Schetzer. In: *Foundations of Aerodynamics*. New York: John Wiley and Sons, 1959.

[16] OpenFOAM. *OpenFOAM User Guide*. 2017.

[17] D. D. Chandar and H. Gopalan. "Comparative Analysis of the Arbitrary Mesh Interface(AMI) and Overset Methods for Dynamic Body Motions in OpenFOAM". In: *46th AIAA Fluid Dynamics Conference*. American Institute of Aeronautics and Astronautics, June 2016.

[18] B. LeBlanc. Dynamics of the Pitch-able VAWT: A Study of the Dynamics of the Vertical Axis Wind Turbine with Individual Pitch Control (2024).

[19] J. Pan, C. Ferreira, and A. van Zuijlen. A numerical study on the blade–vortex interaction of a two-dimensional Darrieus–Savonius combined vertical axis wind turbine. *Physics of Fluids* 35.12 (2023).

IV

EULERIAN-LAGRANGIAN METHOD

6

SIMULATION OF A HYBRID VAWT IN HYBRID EULERIAN-LAGRANGIAN MODEL

The hybrid model used in this chapter has been applied to a rotating cylinder, which has been published in Computers and Fluids*.

In Parts II and III, the Eulerian (U)RANS simulation and Lagrangian vortex particle method have been studied in different VAWT configurations. Eulerian URANS simulation can accurately resolve the flow near VAWTs, but it's computationally expensive. The Lagrangian vortex particle method can efficiently capture the main flow structure, but there are some discrepancies in the force calculation. To avoid computational deficiencies of these individual methods, this chapter simulates a hybrid VAWT using an Eulerian-Lagrangian method implemented in an in-house pHyFlow code. A preliminary study of the hybrid model is conducted in this work, where the hybrid VAWT is simplified as a hybrid force field. Results are compared to the Eulerian method in Chapter 2 and Lagrangian method.

*Rention Pasolari, Jingna Pan, Carlos Ferreira, Alexander van Zuijlen, Flow over traveling and rotating cylinders using a hybrid Eulerian-Lagrangian solver, Computers & Fluids 279, 106327 (2024) [1].

6.1. INTRODUCTION

Previous chapters resolve the flow around the hybrid VAWT using the Eulerian method and the Lagrangian method. In the case of resolving flow physics close to the solid surface, the Eulerian simulation performs better than the Lagrangian simulation in resolution, but it is computationally expensive.

The flow around the hybrid VAWT is quite complex as reviewed in Chapter 1, and scholars around the world have conducted extensive research [2, 3, 4, 5]. Among these studies, it is obvious that a suitable simulation method is vital in the accurate and efficient prediction of the flow field. Researchers have explored different models that can estimate the power output and vortex dynamics effectively. To analyze the complex and unsteady aerodynamic flow associated with wind turbine functioning, computational fluid dynamics (CFD) is an attractive and powerful method [6, 7]. However, the high computational cost of CFD simulation limits studies on the aerodynamic performance of wind turbines. Therefore, alternative computational methods can be applied to save computation time and resources. The vortex method [8] is a mesh-free method in which the vorticity is carried by vortex particles.

Since the Eulerian and Lagrangian solvers are complementary to the simulation techniques, an alternative approach is to divide the computation domain into two regions and apply these two solvers according to the flow characteristics present in each region. By employing the hybrid solver, it is possible to accurately and effectively resolve the flow in the near-wake region and capture the wake flow [9, 10, 11, 12, 13, 14]. Following this idea, this chapter simulated the hybrid VAWT case of Chapter 2 using the hybrid model and compared results with individual Eulerian and Lagrangian methods.

Pasolari et al. [15] developed an in-house pHyFlow code by coupling a vortex particle method with a finite volume solver and using the domain decomposition technique. Results showed a good agreement with the full Eulerian simulations. This chapter extends the work of this hybrid solver presented in [15] by simulating the hybrid VAWT as force fields for the sake of simplification.

6.2. METHODOLOGY

pHyFlow is an in-house code that uses an Eulerian-Lagrangian model (hybrid model) to simulate the VAWT aerodynamics. A brief introduction to the hybrid model is written in this section. More information can be found in Pasolari et al [15].

In this work, the test case is chosen as the simulation of an idealized hybrid VAWT ($c_{T_{AD}} = 0.1$, $c_{T_{AC}} = 0.7$) using Eulerian RANS, Lagrangian vortex particle model (VPM) and hybrid models. The Savonius and Darrieus parts of the hybrid VAWT are represented by uniform force fields as described in Chapter 2. In the Eulerian RANS model, the schematic of the hybrid VAWT is shown in Figure 6.1a, where the force fields of hybrid VAWT (AD+AC) are modeled in the Eulerian domain Ω_E. In the hybrid model, the computational domain is decomposed as the Lagrangian subdomain Ω_L and Eulerian subdomain Ω_E. Two cases are conducted using the hybrid model: In Figure 6.1b, force fields of hybrid VAWT (AD+AC) are modeled in the Eulerian domain Ω_E, and the flow around the hybrid VAWT is resolved in the Lagrangian subdomain; In Figure 6.1c, force fields of Darrieus (AC) and Savonius (AD) part in hybrid VAWT are modeled in the La-

grangian domain Ω_L and Eulerian domain Ω_E, respectively. The Lagrangian VPM is also conducted to resolve the hybrid VAWT problem in the Lagrangian domain Ω_L in Figure 6.1d. The results of the Lagrangian VPM and hybrid models are compared to the Eulerian RANS model.

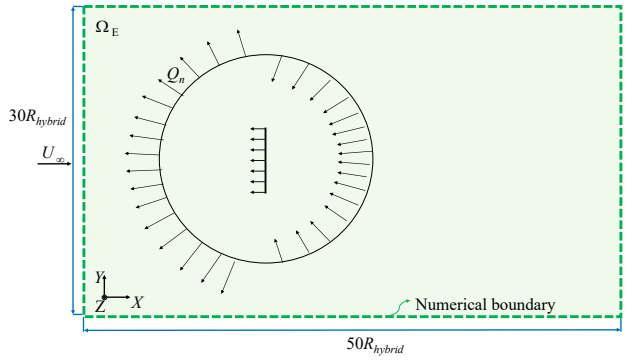

(a) Eulerian RANS (Not true to scale)

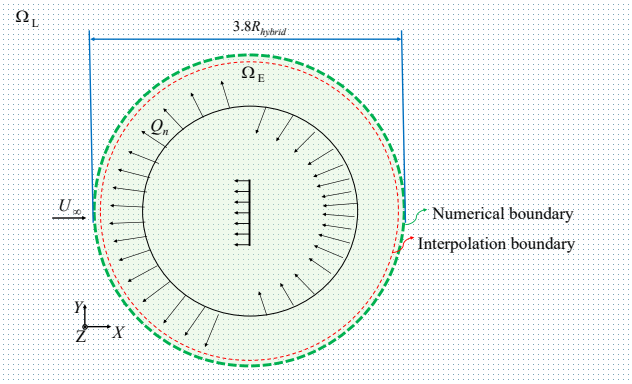

(b) Hybrid model (AD+AC in Ω_E)

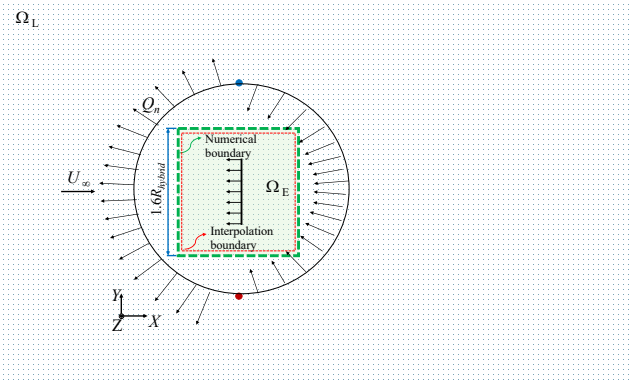

(c) Hybrid model (AD in Ω_E, AC in Ω_L)

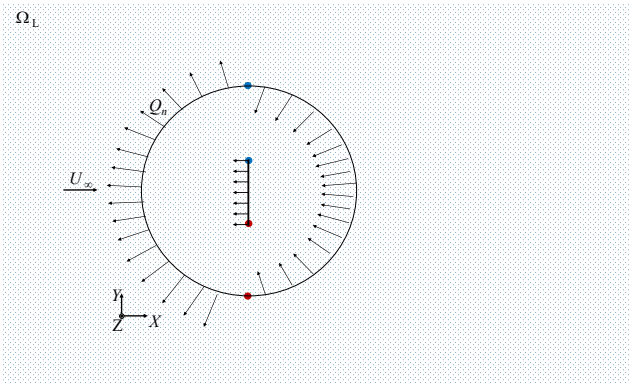

(d) Lagrangian VPM

Figure 6.1: Schematic of computation domain for a hybrid VAWT represented by force fields in (a) Eulerian RANS model (b)(c) hybrid model and (d) Lagrangian VPM (Numerical boundary: green dashed line; Interpolation boundary: red dashed line; The distance between numerical boundary and interpolation boundary is 0.05m; Blue and red dots: location of non-zero $\nabla \times \vec{f}$ where vorticity is created)

Table 6.1: Numerical parameters of Eulerian, Lagrangian and coupled Eulerian-Lagrangian simulations

Parameters \ Reference frame	Eulerian	Lagrangian	Eulerian-Lagrangian
Flow model	Steady, inviscid	Unsteady, inviscid	Unsteady, inviscid
Discretization method	Finite volume	particles	Finite volume + particles
Computational element	8.9e4 cells	2.62e5 particles	4.68e4 cells + 5.62e5 particles in Figure 6.1b, 1e4 cells + 5.62e5 particles in Figure 6.3c
Size of Eulerian domain	$30R_{hybrid} \times 50R_{hybrid}$	-	$3.8R_{hybrid}$ in Figure 6.1b, $1.6R_{hybrid} \times 1.6R_{hybrid}$ in Figure 6.3c
Size of Lagrangian domain	-	Whole domain	Whole domain

The numerical parameters of these simulations are shown in Table 6.1. In the cases with force fields modeled in the Lagrangian domain, the circulation of vortex particles is calculated by the corresponding thrust coefficient c_T, time Δt and inflow velocity U_∞, see Equation $\Gamma = c_T \cdot 0.5 U_\infty^2 \Delta t$. The circulation is added to locations where $\nabla \times \vec{f}$ is nonzero according to Equation 2.1. These locations are marked in Figure 6.1.

In the hybrid solver, the Eulerian subdomain is inside the numerical boundary, where the Finite Volume Method (FVM) is implemented to primarily resolve the near-wake region. The Eulerian solver is implemented in OpenFOAM v9 [16]. Specifically, the solver in this context is pimpleFOAM, an incompressible, transient solver capable of accommodating dynamic mesh simulations. PIMPLE algorithm is used in pimpleFOAM for correcting the velocity and pressure fields to enforce the continuity equation. The Lagrangian subdomain is the entire computational domain, where VPM is implemented to primarily resolve the wake evolution. It is worth noting that an interpolation boundary is applied to the hybrid solver to correct the Lagrangian solution using the Eulerian solution. The Lagrangian and Eulerian solvers are coupled through a two-way communication in the interpolation region. Firstly, the evaluation of the boundary conditions for the Eulerian solver at the numerical boundary. Secondly, the correction of the Lagrangian solution inside the interpolation region, using the more accurate Eulerian solution.

6.3. RESULTS AND DISCUSSIONS

The hybrid model is applied to a hybrid VAWT represented by force fields. The velocity and vorticity fields of four tested scenarios are shown in Figures 6.2 and 6.3. The flow patterns from the hybrid model agree well with those from the Eulerian RANS simulation. The shed vorticity originates from the top and bottom of rotors where the gradients of force distributions are nonzero values [17]. The streamwise velocity at $y = 0$ from the hybrid model is compared with that from the Eulerian RANS simulation to validate the quantitative results of the hybrid model, see Figure 6.4. A good agreement has been observed in this numerical work. The four scenarios have a similar amount of streamwise velocity deficit (around $0.552U_\infty$). The axial induction factor of the wind turbine a is calculated as $a = 0.5 - 0.5\sqrt{1 - c_T}$. The theoretical velocity at the rotor center and theoretical wake velocity are expressed as $U_R = U_\infty(1-a)$ and $U_e = U_\infty(1-2a)$, respectively. The velocity at the far-wake region U_e is comparable with the theoretical value $0.448U_\infty$ under thrust coefficient $c_T = 0.8$. Besides, the numerical velocity at the rotor center agrees well with the theoretical value $0.724U_\infty$. This convergence in results highlights the efficacy of the hybrid model in capturing the flow dynamics of the idealized hybrid VAWT.

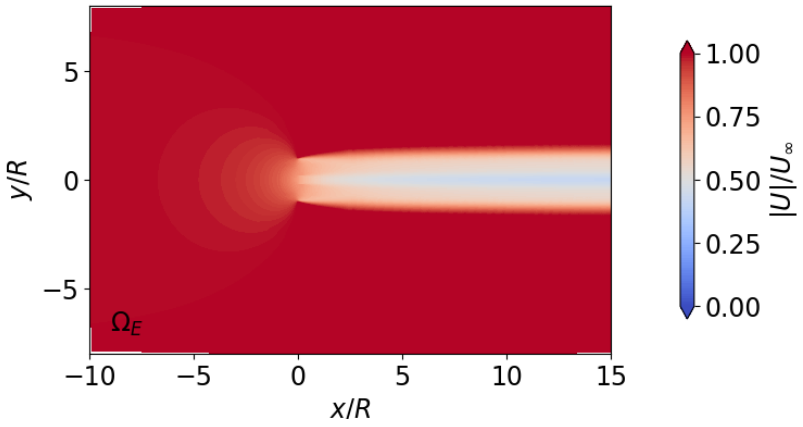

(a) Eulerian RANS

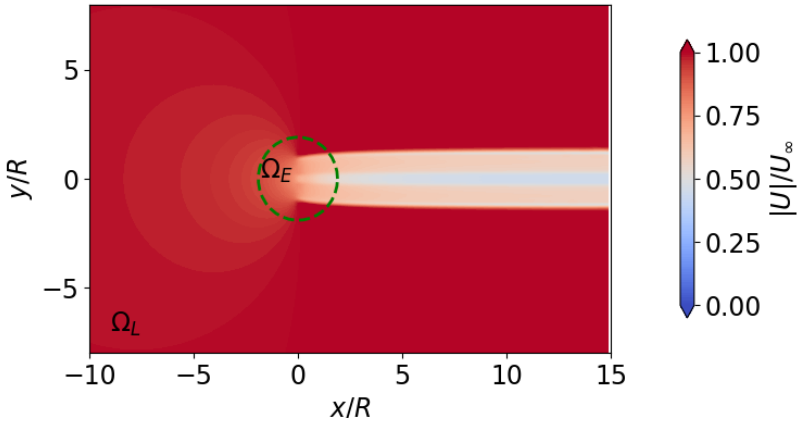

(b) Hybrid model (AD+AC in Ω_E)

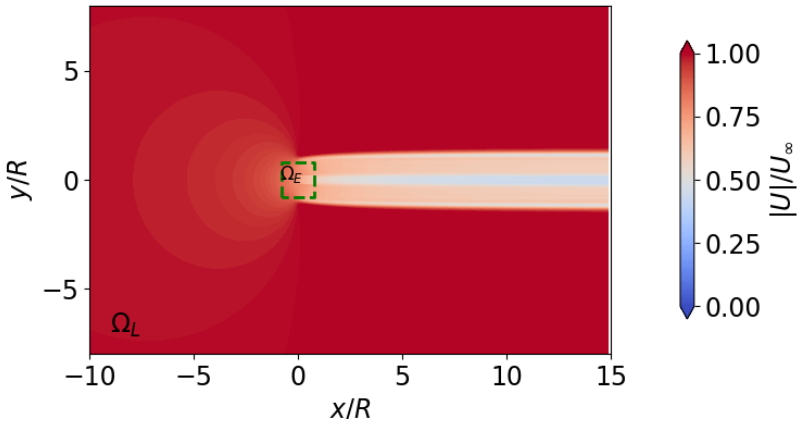

(c) Hybrid model (AD in Ω_E, AC in Ω_L)

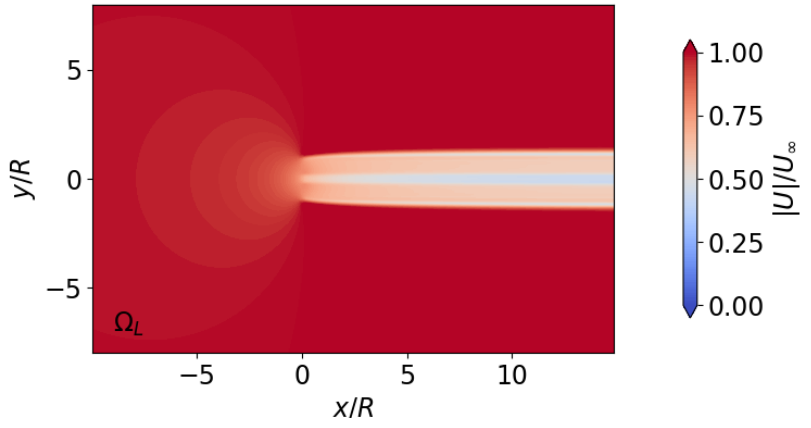

(d) Lagrangian VPM

Figure 6.2: Velocity fields of hybrid VAWTs

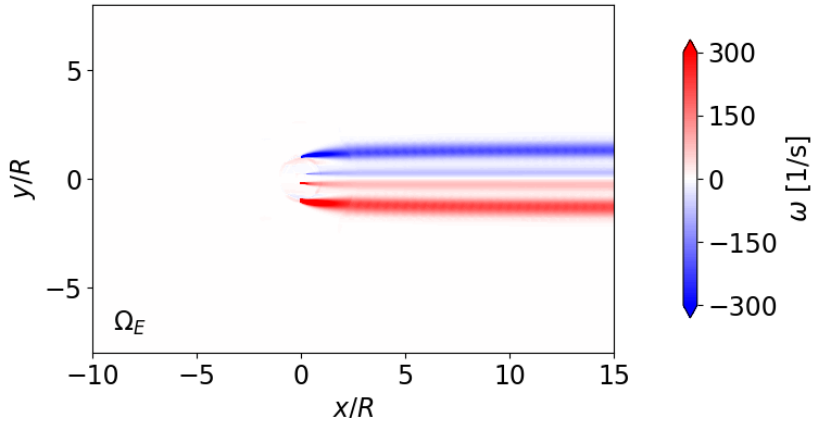

(a) Eulerian RANS

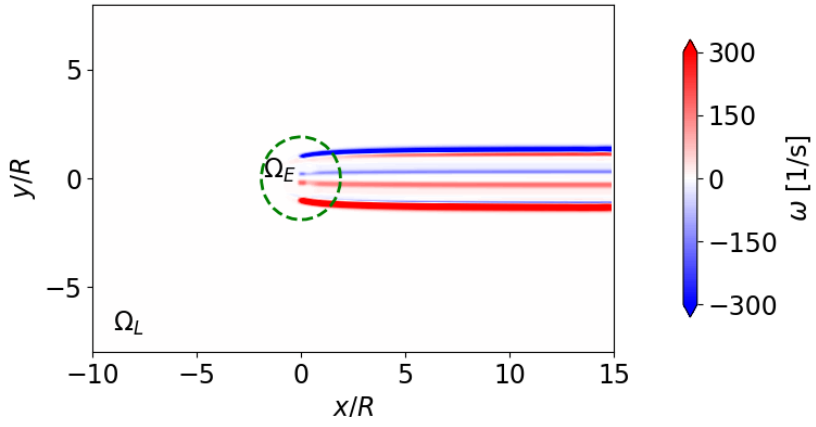

(b) Hybrid model (AD+AC in Ω_E)

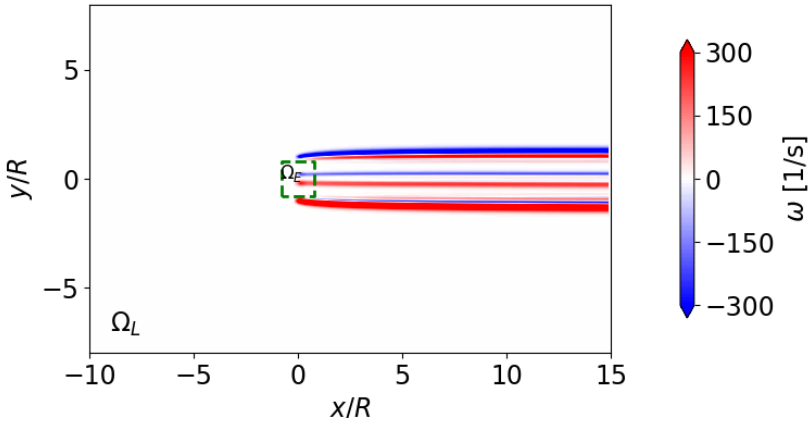

(c) Hybrid model (AD in Ω_E, AC in Ω_L)

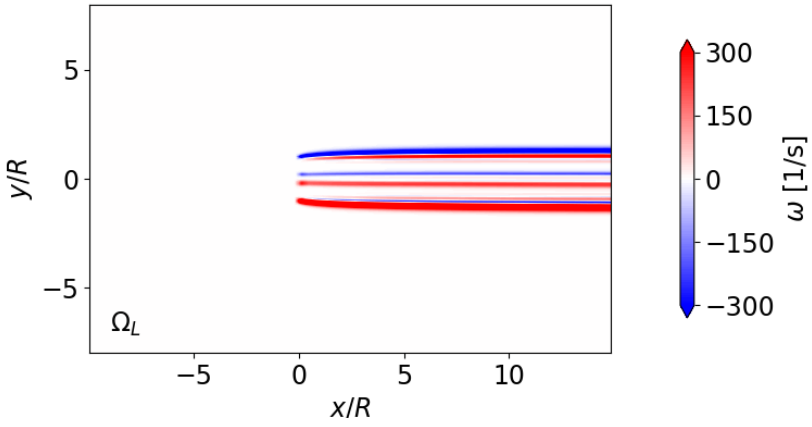

(d) Lagrangian VPM

Figure 6.3: Vorticity fields of hybrid VAWTs

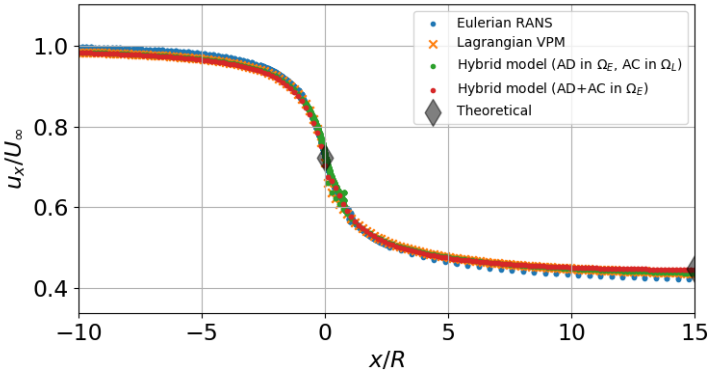

Figure 6.4: Comparison of streamwise velocity at $y = 0$ from Eulerian RANS, Hybrid model (AD+AC in Ω_E), Hybrid model (AD in Ω_E, AC in Ω_L), Lagrangian VPM, and theoretical model

6.4. CONCLUSIONS

The exploration of computational methods for analyzing the intricate flow dynamics around hybrid VAWTs is crucial for improving their aerodynamic performance. While traditional approaches like computational fluid dynamics (CFD) offer accuracy, their high computational cost limits their practicality. The development of alternative methods such as the vortex method and hybrid solvers combining Eulerian and Lagrangian techniques presents promising avenues for overcoming these limitations.

This work has highlighted the evolution of hybrid solvers, emphasizing their ability to efficiently resolve complex flow phenomena of a hybrid VAWT. Further research and experimentation with the proposed hybrid solver across a range of scenarios will be instrumental in fully realizing its potential for optimizing hybrid VAWT design and performance. As the solid boundaries are not included in this work, continued efforts to simulate a hybrid VAWT with real blades will enhance the accuracy and reliability of hybrid solver simulations in capturing flow dynamics near solid boundaries.

Overall, the advancements in computational methods showcased in this study underscore the importance of innovation in addressing the challenges associated with predicting and optimizing the flow around hybrid VAWTs.

REFERENCES

[1] R. Pasolari, J. Pan, C. Ferreira, and A. van Zuijlen. Flow over traveling and rotating cylinders using a hybrid Eulerian–Lagrangian solver. *Computers & Fluids* 279 (2024), p. 106327.

[2] P. Bhadra, S. Alam, B. Debnath, D. Sarkar, and A. Sengupta. Review of Experimental and Computational Analysis of Coaxial H-Savonius Vertical Axis Wind Rotor. *SSRN Electronic Journal* (2019).

[3] D. Sarkar, A. R. Sengupta, P. Bhadra, S. Alam, and B. Debnath. Review of the Hybrid H-Savonius Rotor's Design and Performance. In: *Recent Advances in Mechanical Engineering*. Springer Singapore, 2021, pp. 33–40.

[4] J. Sarma, S. Jain, P. Mukherjee, and U. K. Saha. Hybrid/Combined Darrieus–Savonius Wind Turbines: Erstwhile Development and Future Prognosis. *Journal of Solar Energy Engineering* 143.5 (2021), p. 050801.

[5] A. M. Abdelsalam, M. Kotb, K. Yousef, and I. Sakr. Performance study on a modified hybrid wind turbine with twisted Savonius blades. *Energy Conversion and Management* 241 (Aug. 2021), p. 114317.

[6] A. Alaimo, A. Esposito, A. Messineo, C. Orlando, and D. Tumino. 3D CFD analysis of a vertical axis wind turbine. *Energies* 8.4 (2015), pp. 3013–3033.

[7] K. M. Almohammadi, D. B. Ingham, L. Ma, and M. Pourkashanian. 2-D-CFD Analysis of the Effect of Trailing Edge Shape on the Performance of a Straight-Blade Vertical Axis Wind Turbine. *IEEE Transactions on Sustainable Energy* 6.1 (2015), pp. 228–235.

[8] G.-H. Cottet and P. D. Koumoutsakos. *Vortex Methods: Theory and Practice*. Cambridge University Press, 2000.

[9] G. Papadakis, V. A. Riziotis, and S. G. Voutsinas. A hybrid Lagrangian–Eulerian flow solver applied to elastically mounted cylinders in tandem arrangement. *Journal of Fluids and Structures* 113 (Aug. 2022), p. 103686.

[10] Y. Shi, G. Xu, and P. Wei. Rotor wake and flow analysis using a coupled Eulerian–Lagrangian method. *Engineering Applications of Computational Fluid Mechanics* 10.1 (Jan. 2016), pp. 384–402.

[11] G. H. Cottet. "Particle-grid domain decomposition methods for the Navier-Stokes equations in exterior domains". In: *Vortex Dynamics and Vortex Methods, American Mathematical Society*. 1991, pp. 103–117.

[12] J.-L. Guermond, S. Huberson, and W.-Z. Shen. Simulation of 2D External Viscous Flows by Means of a Domain Decomposition Method. *Journal of Computational Physics* 108.2 (1993), pp. 343–352.

[13] M. L. Ould-Salihi, G. H. Cottet, and M. El Hamraoui. Blending Finite-Difference and Vortex Methods for Incompressible Flow Computations. *SIAM Journal on Scientific Computing* 22.5 (2001), pp. 1655–1674.

[14] G. Daeninck. "Developments in hybrid approaches : Vortex method with known separation location". PhD thesis. Université catholique de Louvain, 2006.

[15] R. Pasolari, C. Ferreira, and A. van Zuijlen. Coupling of OpenFOAM with a Lagrangian vortex particle method for external aerodynamic simulations. *Physics of Fluids* 35.10 (2023).

[16] OpenFOAM9. "https://openfoam.org/version/9/".

[17] J. Pan, C. Ferreira, and A. van Zuijlen. Performance analysis of an idealized Darrieus–Savonius combined vertical axis wind turbine. *Wind Energy* n/a.n/a ().

V

Conclusion

7
CONCLUSION

The current study aims to reveal the flow physics of hybrid VAWT and analyze VAWT performance in various modeling techniques. This dissertation has studied Savonius, Darrieus, and hybrid VAWT using the high-fidelity simulation, vortex particle method, and coupled Eulerian-Lagrangian method. This chapter reflects on the proposed research questions in Chapter 1 and future work that can be implemented on hybrid VAWT.

7.1. MAIN FINDINGS

HOW TO SIMPLIFY THE HYBRID VAWT INTO ITS FUNDAMENTAL FORMULATION AS A HYBRID FORCE FIELD?

We have studied the hybrid VAWT represented by two actuators with uniform force distributions to investigate the effect of the force fields of each turbine component on the performance of the hybrid VAWT. The hybrid force field effectively represents the performance of hybrid VAWT without the influence of blade geometrical and rotor operational parameters. The presence of a Savonius rotor inside a Darrieus rotor leads to a non-ideal force field and hence a lower power output in any circumstance. The hybrid configuration is primarily advantageous for the start-up performance of the combined rotor, which is not explored in this thesis. Given one of the thrust coefficients of the two actuators, the optimal condition for the idealized hybrid VAWT is determined. Given a low $c_{T_{AC}} \leq 0.76$ for the idealized hybrid VAWT, we should increase the thrust coefficient of the inner AD to get the maximum power. While given a series of $c_{T_{AD}}$ for the idealized hybrid VAWT, it requires a higher $c_{T_{AC}}$ for low $c_{T_{AD}}$ case to gain the same amount of power as the high $c_{T_{AD}}$ case. The force fields of the idealized hybrid VAWT also affect the dowstream wake. In the case of an idealized hybrid VAWT with a turbine-mode AD, the high energy extraction on the upwind side of the rotor leads to a deficit in kinetic energy, reducing the energy extraction on the downwind side. However, when the AD operates in a propeller mode, it helps to mitigate the rotor blockage caused by this kinetic energy deficit and to generate a slighter wake expansion downstream. **(Chapter 2)**

HOW WELL CAN AN EULERIAN URANS MODEL PREDICT THE PERFORMANCE AND FLOW DYNAMICS OF A HYBRID VAWT?

We have studied the flow features and performance of the hybrid VAWT using URANS simulations and validated against published results, taking the solid boundaries and blade geometry into account. The URANS simulation illustrates that the power coefficient of hybrid VAWT cannot be as high as that of the single Darrieus. The URANS model well captures the blade-vortex interactions and blade force variations. We investigated the effects of attachment angle and Savonius' tip speed ratio on the hybrid VAWT performance. The power coefficient of the hybrid VAWT with an attachment angle of 60 ° and 90 ° is larger compared to that with 0° and 30°. In the downwind part of hybrid VAWT, the torque variation is dependent on the blade-vortex interaction. The torque coefficient of the Darrieus blade in hybrid VAWT is higher than that in the single Darrieus while the blade interacts with the shed vortex from the advanced Savonius blade. This dependency is observed in varied attachment angles and varied tip speed ratio cases. The Savonius' rotation also affects the performance of the hybrid VAWT. The results indicate that slowing down the Savonius in hybrid VAWT leads to less induction to the flow field and more available energy downstream. Lower λ_S is beneficial to the power performance of the Darrieus part in the hybrid VAWT regardless of the complex mechanics of the rotation axis. **(Chapter 3)**

HOW WELL CAN A LAGRANGIAN VORTEX MODEL PREDICT THE KEY PERFORMANCE PARAMETERS OF VAWTS?

A cost-effective vortex method, DTVPM, is capable of addressing the issue with the absence of flow viscosity and enhancing the computational efficiency. The viscous correction for tip vortices improves the prediction accuracy. The difference of power coefficient Δc_p is improved from -0.10 to 0.01 and from -0.27 to 0.01 at λ = 1.0, 1.2 after viscous correction, respectively. At λ = 0.8, DTVPM is able to capture flow structures at $0 \leq x/R \leq 2$ but predicts a larger deflection of vortex position in y direction at $x/R \geq 2$. Considering the computational efficiency, the serial DTVPM simulation is about 20 to 10^4 times faster than the parallel URANS simulation in 5 revolutions. **(Chapter 4)**

HOW WELL CAN A LAGRANGIAN VORTEX MODEL BE APPLIED TO THE HYBRID VAWT?

By coupling vortex methods to a simple blade model (polar model), it is effective in predicting comparable force variations with Eulerian URANS simulations. Meanwhile, the computational efficiency is compared between URANS and DTVPM for the hybrid VAWT. Results show that a serial simulation of DTVPM is around 20 times faster than a parallel simulation of URANS with reasonable accuracy in terms of ten revolutions. The power coefficient from DTVPM with viscous correction is around 2.95% higher compared to the results from URANS simulation. The maximum normal force coefficient of Darrieus blade in hybrid VAWT from DTVPM deviates around 5.84% from the URANS simulation. By comparing with the Eulerian URANS simulation, the proposed DTVPM is proven to be an inexpensive and reasonably accurate method. The results of blade forces and vortex structures obtained from DTVPM agree reasonably well with those from URANS simulations. **(Chapter 5)**

WHAT IS THE MOST SIMPLE AND EFFICIENT WAY TO MODEL THE HYBRID VAWT IN TERMS OF ITS PERFORMANCE, LOADS, AND VORTICAL STRUCTURES?

The hybrid solver combining Eulerian and Lagrangian techniques presents promising features in accurately and efficiently simulating a hybrid VAWT, represented by a hybrid force field (actuator disk and cylinder). Qualitatively, the flow patterns from the hybrid solver agree well with those from the Eulerian and Lagrangian simulations. The shed vorticity originates from the top and bottom of rotors where the gradients of force distributions are nonzero values. Quantitatively, the streamwise velocity at $y = 0$ from the hybrid solver is compared with that from the Eulerian and Lagrangian simulations to validate the results of the hybrid solver. The velocities at the far-wake region and rotor center are comparable with the theoretical value $0.448U_\infty$ and $0.724U_\infty$, respectively. A good agreement has been observed between the hybrid solver and Eulerian, Lagrangian simulations. The conducted scenarios predict a similar amount of streamwise velocity deficit (around $0.552U_\infty$). This convergence in results highlights the robustness and efficacy of the hybrid solver in capturing the flow dynamics of the hybrid VAWT. **(Chapter 6)**

7.2. CONTRIBUTION TO THE STATE-OF-THE-ART

The thesis makes significant contributions to the state-of-the-art in the field of hybrid VAWTs by addressing key questions regarding power performance, flow features, and numerical modeling techniques for hybrid VAWT systems.

Firstly, the thesis extends the knowledge of wind energy extraction in a hybrid VAWT flow model. Our understanding of power extraction is further improved by the research on the idealized turbine, which excludes geometrical and operational effects. The maximum power output of the idealized hybrid VAWT with a given $c_{T_{AD}}$ is lower than that of a single actuator. This indicates an idealized hybrid VAWT cannot show a significant power increase compared to the optimal single Darrieus rotor. The hybrid configuration is primarily advantageous for the start-up performances of the combined rotor instead of the power performances. **(Chapter 2)**

Secondly, the thesis numerically investigates the differences in flow fields between the single Darrieus rotor and its counterpart in a hybrid VAWT using an Eulerian URANS model. It explores the mutual influence between the wakes of Savonius and Darrieus rotors in a hybrid configuration, elucidating how this influence manifests in terms of flow dynamics and turbine performance. The effects of attachment angle and Savonius' rotation speed on the hybrid VAWT flow physics are further studied by a detailed blade-vortex interaction analysis. By characterizing flow patterns and correlating them with changes in blade torque, we acquire valuable insights that are utilized to enhance the efficiency of the hybrid VAWT. The torque increase of the Darrieus blade in hybrid VAWT (compared to a single Darrieus rotor) is due to the appearance of the vortex shedding from the advanced Savonius blade. The correlation between blade torque variations and vortex dynamics is independent of the attachment angle and tip speed ratio. **(Chapter 3)**

Lastly, the thesis focuses on implementing efficient models tailored to different types of VAWTs. It discusses how existing models are adapted and applied to simulate both single- and multi-rotor systems, optimizing computational efficiency and accuracy. Through rigorous evaluation, the thesis assesses the computational efficiency and accuracy of the Lagrangian VPM and the Eulerian-Lagrangian hybrid model, providing insights into their strengths and limitations. The Lagrangian VPM can efficiently predict the wake dynamics and torque coefficient of various types of VAWTs. Compared to the Lagrangian VPM, the hybrid model is capable of representing hybrid VAWT in the Eulerian reference frame and modeling its wake dynamics in the Lagrangian reference frame. The hybrid model provides preliminary knowledge and techniques to an efficient model in the case of hybrid VAWT. These contribute to advance the design, optimization, and analysis of hybrid VAWT systems, ultimately enhancing their performance and cost-effectiveness in renewable energy generation. **(Chapter 4 & Chapter 5 & Chapter 6)**

7.3. FUTURE RESEARCH

The future research of hybrid VAWTs is promising with continued advancements in modeling techniques and integration of novel technologies expected to drive further performance improvements. There are still unresolved research questions regarding the advancement of hybrid modeling for hybrid VAWT.

1. **Where should the hybrid VAWT development move towards?**
   It is important to acknowledge that the hybrid VAWT is unlikely to surpass the power output of a single Darrieus rotor by changing operational and geometrical conditions. Instead of striving for maximum power generation in this context, our attention should pivot towards more pragmatic approaches: enhancing the start-up performance of the hybrid VAWT while mitigating power losses, and tuning the wind condition around the turbine (e.g., using wind deflectors). Redirecting our focus towards optimizing these attributes significantly enhances the practicality of hybrid VAWTs in the renewable energy landscape.

2. **How can the current study of hybrid VAWT be extended to incorporate urban applications?**
   This study used the 2D simulation for the hybrid VAWT. To extend the comprehensive study of vortex dynamics in hybrid VAWT and incorporate it with urban applications, 3D effects should be taken into account in future work. It allows us to study the effect of tip vortices on turbine performance. Besides, research on wake development in the vicinity of the Savonius and Darrieus blades within hybrid VAWTs will continue to advance. This involves further understanding the impact of blade vortex interaction on the vorticity system and how vortex shedding influences startup and power performance in the axial direction. It is also suggested to explore innovative approaches to mitigate power losses of hybrid VAWTs based on insights gained from 3D wake dynamics, such as optimizing wake management strategies and enhancing turbine design.

3. **How can we accurately and efficiently simulate the flow fields in the far-wake region of VAWTs?**
   In the vortex particle method, the mesh-free modeling and unconfined numerical boundary benefit the efficient simulation of far-wake flow. This method requires a viscous correction due to the potential flow assumption. We considered the viscous effects near the Savonius and Darrieus blades by relocating the latest few shed vortices from the Savonius blade tips and including the viscous polar of the Darrieus blades, respectively. Future research should focus on considering viscous effects at further downstream of VAWTs. This will enable a thorough investigation of the wind farm layout design and blade/rotor-wake interaction.

4. **How can we improve the hybrid method for hybrid VAWT simulations?**
   The hybrid method plays an important role in the efficient prediction of hybrid VAWTs. We have observed the potential of the hybrid method from the simulation of a hybrid VAWT represented by force fields. The blade-resolved simulation for the hybrid VAWT will be presented in the future. This requires a thorough consideration of various simulation parameters, such as the size of the Eulerian domain, vortex core radius and growth factor, time step size, etc. It will allow an accurate simulation of boundary layer flow in the hybrid VAWT and follow-up research on the complex multi-rotor system.

VI

Appendix

A

Mesh independence study of Savonius using Eulerian URANS

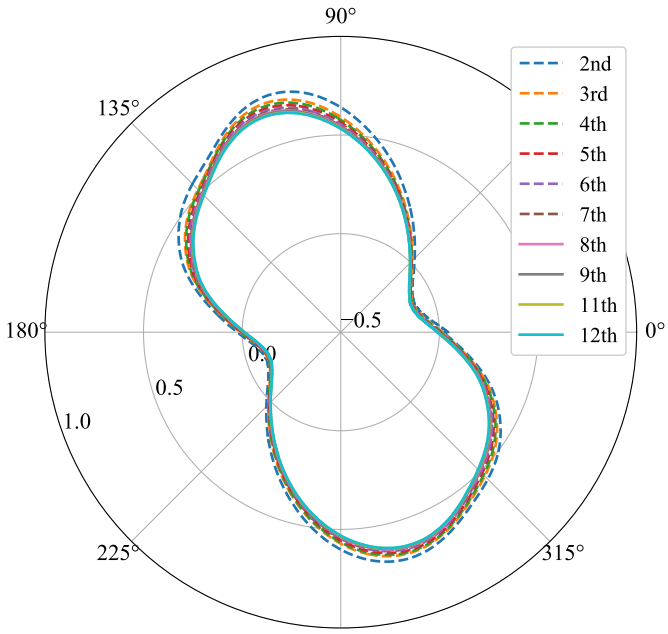

Figure A.01: Convergence of power coefficient for Savonius rotor at 0.24°/step, $\lambda_S = 0.8$, $U_\infty = 7$m/s, medium mesh configuration

The mesh independence study is conducted to determine the appropriate mesh size for URANS simulations of VAWT. A single-stage two-bladed semicircular Savonius rotor without gap width [1] is arranged in a computational domain of $30R_S \times 50R_S$. The distance between the inlet and Savonius rotation axis is $15R_S$. The inflow wind speed is 7m/s with a corresponding rotation speed of 11.2rad/s. Three sets of meshing with varying mesh resolutions were generated with the first row's cell height of 0.046mm, 0.051mm and 0.056mm and the growth factor of 1.2. In this study, the first row's cell height was calculated with the premise of the dimensionless wall distance $y^+ = \frac{\rho u_\tau \cdot \Delta y_1}{\mu}$ [2] lower than one. The three sets of mesh are named coarse mesh, medium mesh and fine mesh, with the total numbers of mesh being around 1.77e5, 1.83e5, 1.90e5 and blade discretization of 296, 312, 332, respectively. Pave meshing scheme is applied for all surfaces. The discretization of the inlet and outlet boundaries uses double-sided successive ratio of 0.95 to refine the wake region. The maximum values of calculated y^+ occur at the convex side of blades with an average value below one. This indicates an effective meshing strategy [3]. The power coefficients from the three mesh configurations are shown in TABLE A.01. The values of the maximum skewness for the three mesh configurations are 0.72, 0.73, 0.66, respectively. The medium and coarse mesh configurations differ by 0.15% and 0.57% from the fine mesh, which indicates the medium mesh yields reasonably accurate results. In order to properly control convergence, the simulation residual was set as 1e-5. Among all the simulations in this work, the interpolation scheme has

a second order of accuracy. The azimuthal increment of 0.24°/step was chosen according to the published time step independence study for a Savonius rotor with similar tip speed ratio, wind speed, and diameter [4, 5]. The simulation time is over twelve revolutions. The power coefficients of Savonius from different revolutions are shown in FIG. A.01. It demonstrates that there is little change in the power coefficient between the sixth and seventh revolutions. So, the simulation results are considered as converged from the sixth revolution.

Table A.01: Power coefficient of Savonius rotor from different mesh configurations, $\lambda_S = 0.8$, $U_\infty = 7$m/s

Mesh	Fine	Medium	Coarse
Number of cells	1.90e5	1.83e5	1.77e5
Blade discretization	332	312	296
First row's cell height [mm]	0.056	0.051	0.046
Number of layers	26	28	30
Power coefficient c_p	0.2614	0.2618 (+0.15%)	0.2629 (+0.57%)

Table A.02: Power coefficient of Darrieus rotor from different mesh configurations, $\lambda_D = 4.0$, $U_\infty = 4.01$m/s

Mesh	Fine	Medium	Coarse
Number of cells	2.02e5	1.58e5	1.38e5
Blade discretization	92	70	62
First row's cell height [mm]	0.018	0.022	0.018
Number of layers	28	28	30
Power coefficient c_p	0.4343	0.4220 (-2.83%)	0.3604 (-17.0%)

A

REFERENCES

[1] J. Pan, C. Ferreira, and A. vanZuijlen. Estimation of power performances and flow characteristics for a Savonius rotor by vortex particle method. *Wind Energy* 26.1 (Jan. 2023), pp. 76–97.

[2] H. Versteeg and W. Malalasekera. *An Introduction to Computational Fluid Dynamics: The Finite Volume Method*. Pearson Education Limited, 2007.

[3] E. Fatahian and H. e. a. Lohrasbi Nichkoohi A.and Salarian. Comparative study of flow separation control using suction and blowing over an airfoil with/without flap. *Sādhanā* 44.220 (2019).

[4] P. Jaohindy, S. McTavish, F. Garde, and A. Bastide. An analysis of the transient forces acting on Savonius rotors with different aspect ratios. *Renewable Energy* 55 (2013), pp. 286–295.

[5] S. McTavish, D. Feszty, and T. Sankar. Steady and rotating computational fluid dynamics simulations of a novel vertical axis wind turbine for small-scale power generation. *Renewable energy* 41 (2012), pp. 171–179.

B

Mesh independence study of Darrieus using Eulerian URANS

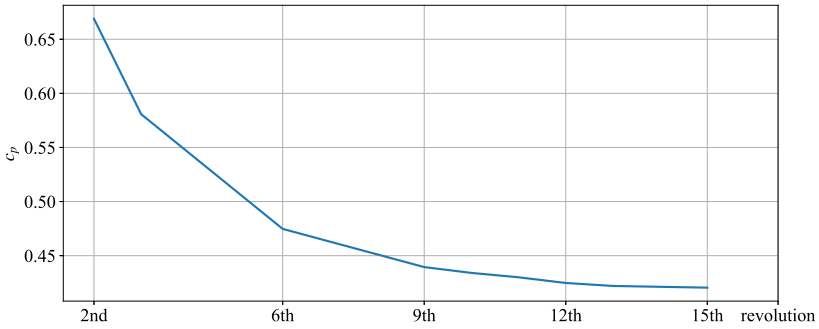

Figure B.01: Convergence of power coefficient for Darrieus rotor at 0.24°/step, $\lambda_D = 4.0$, $U_\infty = 4.01$m/s, medium mesh configuration

A mesh independence study of a two-bladed Darrieus rotor with the same geometrical parameter as the Darrieus part in the hybrid VAWT and the same meshing strategy as the Savonius rotor is conducted. The rotation axis of the Darrieus rotor is $10R_D$ from the inlet and $24R_D$ from the outlet. To optimize the limits of cell size, three mesh configurations (coarse, medium, fine) are simulated with cell numbers of 1.38e5, 1.58e5 and 2.02e5, respectively. The values of the maximum skewness for the three mesh configurations are 0.71, 0.69, 0.51, respectively. The simulation residual is set as 1e-5. An azimuthal increment of 0.24°/step is seen as sufficient according to the convergence studies of Rezaeiha et al. [1] and Edwards et al. [2]. The average $y+$ over the blade surface is below one with the maximum value at the leading edge [3]. The power coefficient from different mesh configurations and mesh details are shown in TABLE A.02. The convergence of power coefficient from different revolutions is depicted in FIG. B.01. The results show that the medium mesh configuration yields reasonably accurate results with a -2.83% difference from the fine mesh configuration. The power coefficient of the Darrieus rotor is seen as converged from the twelfth revolution.

REFERENCES

[1] A. Rezaeiha, I. Kalkman, and B. Blocken. Effect of pitch angle on power performance and aerodynamics of a vertical axis wind turbine. *Applied energy* 197 (2017), pp. 132–150.

[2] J. M. Edwards, L. A. Danao, and R. J. Howell. PIV measurements and CFD simulation of the performance and flow physics and of a small-scale vertical axis wind turbine. *Wind Energy* 18.2 (2015), pp. 201–217.

[3] E. Fatahian and H. e. a. Lohrasbi Nichkoohi A.and Salarian. Comparative study of flow separation control using suction and blowing over an airfoil with/without flap. *Sādhanā* 44.220 (2019).

C

SENSITIVITY ANALYSIS OF DARRIEUS USING LAGRANGIAN VPM

The two-bladed Darrieus rotor is simulated using VPM and OpenFOAM. The simulation and geometrical parameters are the same as the Darrieus part of hybrid VAWT. To check the convergence of VPM simulation, the sensitivity analysis of VPM application in terms of time step discretization and number of revolutions is summarized in this section.

Results of downstream velocity from VPM are compared with URANS results. The downstream velocity curve from URANS is an average of 12th to 15th revolutions. One diameter downstream velocity curve from various revolutions at $\lambda_D = 4.0$ is depicted in Figure C.01. The 14th revolution is seen to converge. In terms of computational sensitivity, the downstream velocity curve from different angle intervals is shown in Figure C.02. The comparison indicates that VPM with $\Delta\theta = 3.60°$ predicts similar velocity profiles with finer cases. Additionally, this will consume less computational time. So, $\Delta\theta = 3.60°$ is applied to different turbine cases in this work.

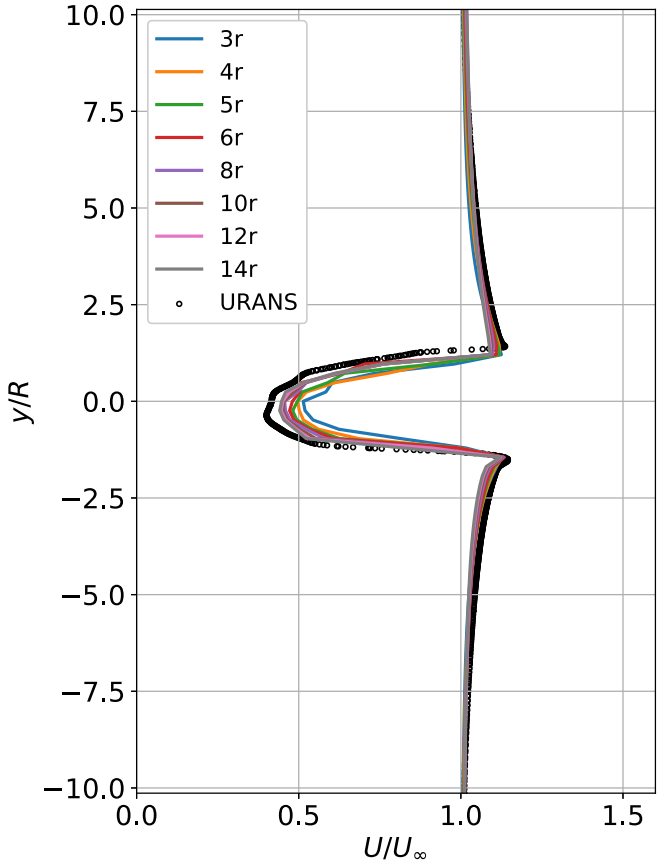

Figure C.01: Downstream velocity curve from various revolutions of Darrieus rotor, $\lambda_D = 4.0$, $x/R = 2$, $\theta = 360°$

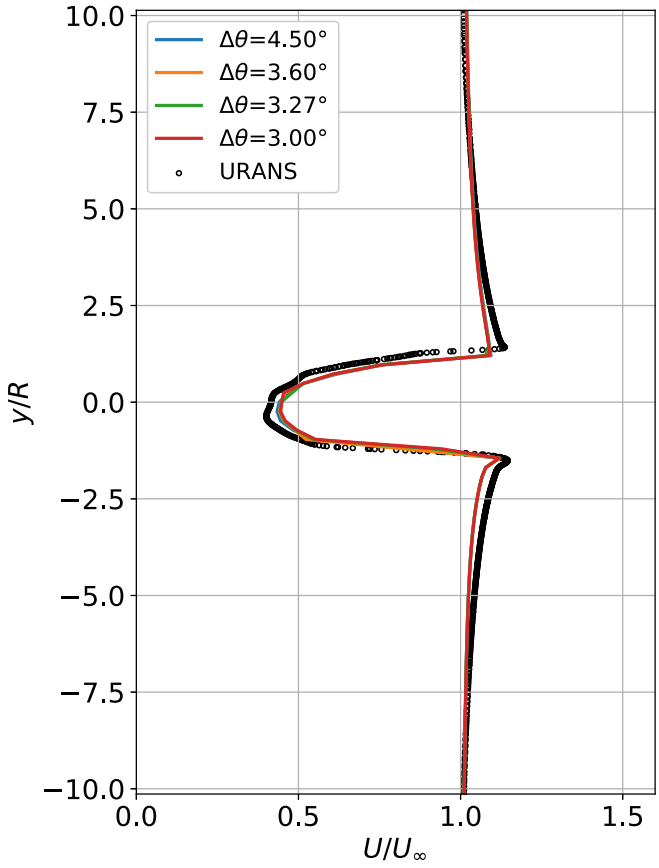

Figure C.02: Downstream velocity curve from different angle intervals, $\lambda_D = 4.0$, $x/R = 2$, $\theta = 360°$, VPM results are taken from the 14th revolution

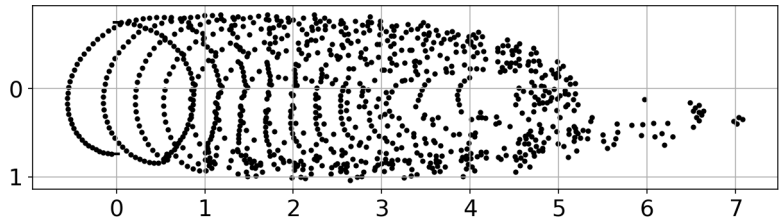

(a) $\Delta\theta = 4.5°$

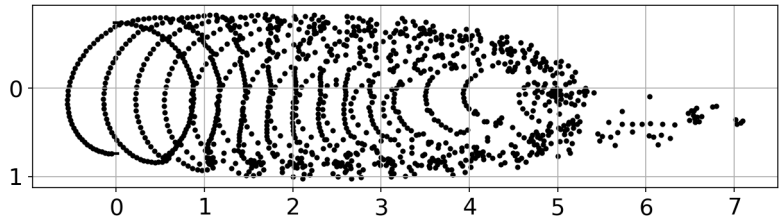

(b) $\Delta\theta = 3.6°$

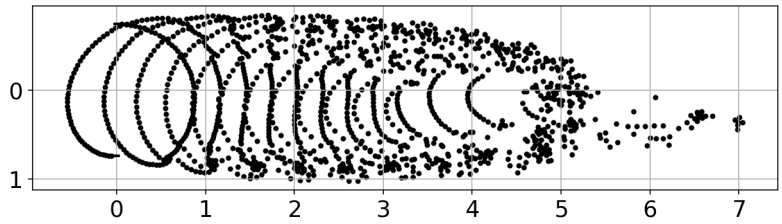

(c) $\Delta\theta = 3.27°$

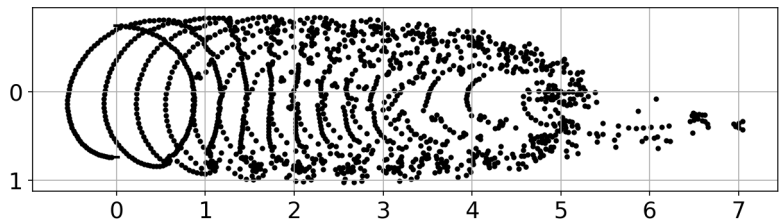

(d) $\Delta\theta = 3.00°$

Figure C.03: Particle map of Darrieus rotor from different angle intervals using VPM, $\lambda_D = 4.0$

D

SENSITIVITY ANALYSIS OF HYBRID VAWT USING LAGRANGIAN DTVPM

The downstream velocity of the hybrid VAWT is sampled at $x/R = 2$, $\theta = 360°$ from different revolutions in Figure D.01. It is observed that velocity from the 14th revolution agrees better with URANS simulation compared to the 6th revolution. In this work, results from the 14th revolution are discussed based on the hybrid VAWT case.

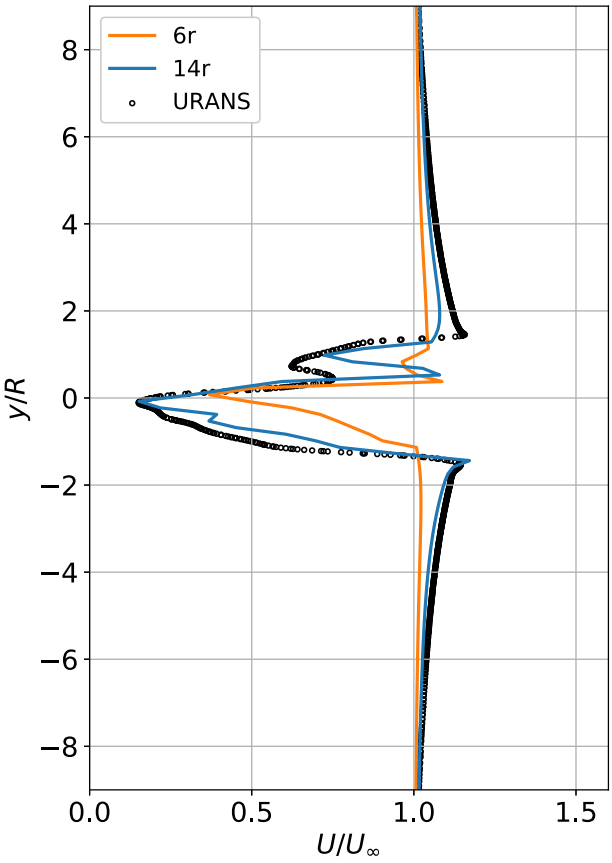

Figure D.01: Downstream velocity curve from different revolutions of hybrid VAWT, $\lambda_{\text{hybrid}} = 4.0$, $x/R = 2$, $\theta = 360°$

ACKNOWLEDGEMENTS

I am immensely grateful to all those who have contributed to the completion of this dissertation. My doctoral journey has been a challenging yet rewarding experience, and I could not have achieved this milestone without the support, guidance, and encouragement of numerous individuals and institutions.

First and foremost, I would like to express my gratitude to my promotor Prof. Dr. Ir. Carlos Ferreira, for your unwavering support, insightful guidance, and invaluable mentorship throughout this research. Your expertise has been instrumental in shaping the direction of my work and enhancing its quality. Your diverse perspectives have helped me approach my research questions from multiple angles and develop a comprehensive understanding of my field. I wish to formally convey my profound gratitude to Dr. Alexander van Zuijlen, my esteemed co-promotor. Your consistent assistance and invaluable guidance have greatly contributed to my work. I extend my appreciation for your attentive ear and enduring patience. Our meetings have been a source of genuine pleasure and enlightenment. I want to thank our secretary, Sylvia, for her hard work and dedication. Her efficiency and professionalism are greatly appreciated. I also want to acknowledge the committee members. Thank you for your time and efforts.

I would like to thank my colleagues and fellow researchers for their camaraderie, inspiring discussions, and mutual support. The exchange of ideas and experiences within this vibrant community has been an essential aspect of my academic journey.

In my first year, I received lots of warm tips from senior PhDs. Carlos, you helped me start my journey with the Linux system and gave me a brief introduction to the vortex particle method. Delphine, you kindly shared your animation of the turbine's loading and useful website for PhD. Your random acts of kindness inspired me to be a senior like you. Mikko, you are my enlightenment teacher of OpenFOAM. I admire your professional skills. We had many coffee breaks and afternoon walks together before the pandemic. The conversations brought light to me when facing an unknown future and unfamiliar environments. Thanks for being so nice to me. Ming, Kaisheng, Weibo, I would like to thank you for inviting me to your cycling group during Covid time. Those trips were a lot of fun.

Guanqun, we shared lots of memories while traveling and exploring Europe. You are always thoughtful and kind, gentle and powerful. You have a clear future goal that I really admire. I hope you can achieve it in the future. Deepali, we had a good time during bouldering. That was my first time trying it and there will be many times in the future. Adhyanth, I would like to express my gratitude for your efforts in creating and sharing stickers within the group chat. Your contributions have added an element of fun and have helped create lasting memories. Your enthusiasm in promoting "One Piece" has not gone unnoticed, and you have truly been an integral part of my PhD journey. Rention, during our discussions on your hybrid solver, your impressive software development skills were evident. Wishing you great success with your book. Kiran, the gossip

we had distracted me and released much of my stress. Thanks for the tips on tennis and badminton. I hope we can still play badminton, ping-pong, and tennis in the future. Mehtab, Jiaxin, Likhitha, Ricardo, Flavio, Ali and Marie, we shared lots of memories on many dinner and movie nights. I enjoyed them a lot (including so many horror movies). I hope we can still have dinner together in the future. Mihir, you are the first influencer with 200k+ subscribers among all my friends. Keep going! One day in the future, can you please ask Hrithik to sign me a poster? Anand, it was an amazing trip to come across you and your dad in Rome. I will never forget the yoga class on the hill of TU Delft Library. David, I admire your 'Work hard, play harder' vibe. Your leaping thinking is a talent that I wish I had. Best wishes for your future career. Simone, I hope your magazine will be the top of the top in the future. Matteo, the best officemate forever! Thank you for offering me tasty wedding chocolates. Yanan and Jiashang, the dumplings we made together were pieces of art. You have added a lot of color to my life. Wencan, Yifu, and Xiang, you are all incredible Mafia players. Our trips are unforgettable because of your enthusiastic involvement. Erik, Seba, Shyam, André, Rishi, Oriol, Abhyuday, Anwesha, Nils, Livia, Yan, Jatinder, Abhratej, Edo, and Hafiz, thank you for many chitchat during lunch, coffee breaks, or drinks. Your words have added a spark to my life. Special thanks to my Spanish friends, Mon, Uma, Sandra, Iris, Manu, Júlia, Lucía, Javi, Marta, and Macia, I am lucky to have met you all. Our trip to Estartit beach will always be unforgettable.

My gratitude extends to my friends and family for their unwavering encouragement, patience, and belief in my abilities. Baba and Mama, your emotional support provided the foundation upon which I could face the challenges of this endeavor. Thank you for your unwavering support. Knowing that you will always be by my side empowers me to pursue my dreams confidently. Special thanks to Jianwen, we shared lots of tears and laughter. You are the most important part of my life in the Netherlands. Thanks for your company. Dong, thank you for cheering me up while I felt depressed. Your company makes me feel peace of mind. Love ya!

In conclusion, the completion of this dissertation marks the culmination of years of hard work and collaboration. I am truly grateful to everyone who played a role, no matter how small, in helping me realize this achievement. This dissertation stands as a testament to the power of collective effort and the significance of meaningful relationships in the pursuit of knowledge.

Thank you all!

August 2024

CURRICULUM VITÆ

Jingna PAN 潘静娜

16-04-1994 Born in Yantai, China.

EDUCATION

2012–2016 Bachelor in Environmental Protection Equipment Engineering

China University of Petroleum (East China)

2016–2019 Master in Power Engineering

China University of Petroleum (East China)

Excellent Graduate and Excellent Master Thesis Award 2019

2019–2023 PhD in Wind Energy

Delft University of Technology, Netherlands

LIST OF PUBLICATIONS

JOURNAL PAPER

5. **Jingna Pan**, Carlos Ferreira, Alexander van Zuijlen, *A viscous vortex particle method for a Darrieus-Savonius combined vertical axis wind turbine*, under review.

4. Rention Pasolari, **Jingna Pan**, Carlos Ferreira, Alexander van Zuijlen, *Flow over traveling and rotating cylinders using a hybrid Eulerian-Lagrangian solver*, Computers & Fluids **279**, 106327 (2024).

3. **Jingna Pan**, Carlos Ferreira, Alexander van Zuijlen, *Performance analysis of an idealized Darrieus-Savonius combined wind turbine*, Wind Energy, 1-16 (2024).

2. **Jingna Pan**, Carlos Ferreira, Alexander van Zuijlen, *A numerical study on the blade–vortex interaction of a two-dimensional Darrieus–Savonius combined vertical axis wind turbine*, Physics of Fluids **35**, 125152 (2023).

1. **Jingna Pan**, Carlos Ferreira, Alexander van Zuijlen, *Estimation of power performances and flow characteristics for a Savonius rotor by vortex particle method*, Wind Energy **26** (1), 76-97 (2023).

CONFERENCE

1. **Jingna Pan**, Carlos Ferreira, Alexander van Zuijlen, *Numerical analysis of a 2D lift-drag combined vertical axis wind turbine*, Wind Energy Science Conference, Glasgow, 2023.